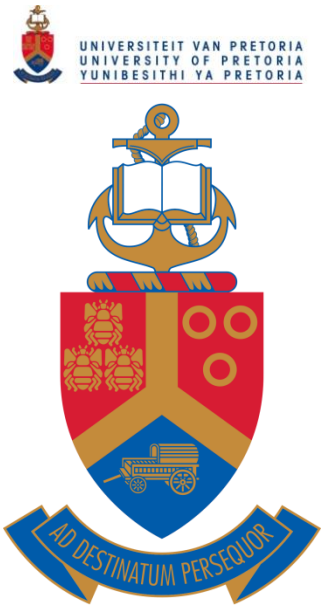

Microstructure and properties of laser beam and gas tungsten arc welded zirconium-2.5niobium

By

Sibusiso S. Mahlalela

Submitted in partial fulfillment of the requirement for the degree

MSc: Applied Science (Metallurgy)

In the Faculty of Engineering, the Built Environment and Information Technology
Department of Material Science and Metallurgical Engineering.
University of Pretoria

May 2018

Supervisor: Prof. P.G.H. Pistorius

ACKNOWLEDGEMENTS

Firstly I would like to sincerely thank God the Father and my savor Jesus Christ for the wisdom, inspiration, and strength that saw me through to completion of this research project.

For the LORD gives wisdom; from His mouth come knowledge and understanding.

Proverb 2:6

To my wife, Malebo, thank you for your support, encouragement and for taking care of our two daughters as I have been focused on my research. I dedicate this research project to my two daughters, Uthando and Lethubuhle Mahlalela, I hope this inspires you to grow up to be the best you can be.

I would like to extend my gratitude to my supervisor, Prof. Pieter Pistorius for the unwavering support and guidance throughout. Your invaluable expertise and counsel has made it possible for me to complete this work.

Thank you to the Advanced Metals Initiative (AMI) and SAIW Centre for Welding Engineering at the Department of Material Science and Metallurgical Engineering, for the financial support. I would also like to extend my gratitude to IMMRI, Laboratory for Microscopy and Microanalysis at University of Pretoria, and CSIR National Laser Center for assistance with the experimental work.

ABSTRACT

The service performance of zirconium-2.5niobium components is largely dependent on the microstructure and mechanical properties achieved through a specific thermo-mechanical process applied during manufacturing. Welding causes microstructural changes which can result in unfavorable changes of properties. The aim of the current study is to understand the transformation behavior of zirconium-2.5niobium during welding, the resulting microstructure and the effect on mechanical properties.

Autogenous bead on plate welding using varying parameters was conducted on Zr705 (zirconium-2.5niobium) alloy sheet of 1.5 mm thickness. The two most common fusion welding processes in reactor core fabrication, namely laser beam welding (LBW) and gas tungsten arc welding (GTAW), were applied. Dilatometry was performed on cooling from 1050°C at varying cooling rates ranging between 0.5-600°C/s. In addition, tensile and micro-Vickers hardness tests were done to characterize the mechanical properties.

Microstructural examination of the dilatometry samples cooled between the ranges of 0.5-50°C/s showed a Widmanstätten structure. At 0.5-10°C/s cooling rate the structure exhibited coarse hcp alpha phase structure with a large volume fraction manifesting as basket weave. Parallel plate structure and grain boundary allotriomorphs (GBA) were also observed. At intermediate cooling rates (10-50°C/s), basket-weave morphology was dominant and composed of finer intragranular alpha plates that randomly precipitated on a number of planes within the same parent β grain. At cooling rates of 150°C/s and higher, the dominant transformation product was martensite. The morphology exhibited acicular (α′) martensite plates. The martensite structure was finer at higher cooling rates.

The GTAW and LBW morphology were very similar. The heat affected zone (HAZ) and weld metal of both processes were characterized by an equiaxed grain morphology at low heat input. Increased heat input resulted in the equiaxed to columnar grain morphology transition at the weld metal. The microstructures of GTAW exhibited a basket weave structure in both HAZ and weld metal, with retained beta phase observed in HAZ of some welds. The LBW microstructures consisted of a mixture of martensite, retained beta and Widmanstätten structure in the HAZ, with a fully martensitic weld metal.

Based on the dilatometry and weld results, hardness and cooling rate have a positive linear relationship up to about 150°C/s, when the martensitic reaction occurs and the hardness plateaus. Laser beam welds had a higher tensile strength than the gas tungsten arc welds, this was due to the higher cooling rate and a much finer martensitic structure.

Table of Contents

List of Figures

List of Tables

List of Acronyms and Abbreviations

ASME	American Society of Mechanical Engineers
ASTM	American Society for Testing and Materials
AWS	American Welding Society
BCC	Body Centred Cubic
CANDU	Canada Deuterium Uranium (Canadian nuclear reactor)
CCT	Continuous cooling transformation
DCEN	Direct current electrode negative
DCEP	Direct current electrode positive
EBW	Electron beam welding
EWTh	Thoriated tungsten electrode
FEG SEM	Field emission gun scanning electron microscope
GBA	Grain boundary allotriomorphs
GTAW	Gas tungsten arc welding
HAZ	Heat affected zone
HCP	Hexagonal Close Packed Crystal Structure
HI	Heat Input
ISO	International Organization for Standardization
LBW	Laser beam welding
LWR	Light-water reactor
M_f	Martensite finish
M_s	Martensite start
PHWR	Pressurized heavy water reactor
PWHT	Post weld heat treatment
RBMK	Reaktor Bolshoy Moshchnosty Kanalny (Russian nuclear reactor)
TEM	Transmission electron microscope
UTS	Ultimate tensile strength
YS	Yield strength

CHAPTER 1

General Background and Overview

1.1 Introduction

Zirconium is mainly used to manufacture nuclear plant components. The metal and its alloys have limited application in the chemical industry. Zirconium alloys are preferred for nuclear applications because of low neutron absorption cross-section, good resistance to corrosion, and good creep resistance (Douglass, 1971). Over the years, extensive research has been done in the development of zirconium-tin alloys (the so-called Zircaloy alloys). The two widely used zirconium-tin alloys are Zircaloy-2 and Zircaloy-4. Though Zircaloy-2 was first chosen as the pressure tube material because of the confidence gained on this material in the reactor environment, zirconium-2.5niobium soon replaced it because of superior properties, (Robertson, 1979):

- Zirconium-niobium tubes possess higher strength than Zircaloy. The higher strength of the heat-treated zirconium-2.5niobium offers a reduction in the pressure tube wall thickness of nearly 40 percent.
- Zirconium-niobium alloys have improved corrosion resistance when appropriate thermo-mechanical processing is applied.
- Zircaloy-2 is inferior to either cold-worked or heat-treated zirconium-2.5niobium when considering creep performance.

The welding of zirconium alloy components is one of the most critical manufacturing processes of nuclear reactor fuel assembly components (Rudling, 2007). Zirconium and its alloys have good weldability. It is, unfortunately, a reactive metal and therefore susceptible to contamination by elements like hydrogen, nitrogen, oxygen, and carbon at temperatures above 370°C during the welding operation (Krueger, 2015). Small amounts of both nitrogen and oxygen contamination increases the hardness and tensile strength, and lowers the ductility of zirconium (Lustman, 1955). The most serious problems associated with welding zirconium-niobium alloys are delayed hydrogen cracking and embrittlement due to contamination. Thorough cleaning of work-piece and good shielding from atmospheric gases is thus essential. Welding also introduces residual stresses and changes to the crystallographic texture of the material (Coleman, 1994). Besides contamination, an important factor to consider during welding is the heat input, because heat input influences the cooling rate which in turn affects the resulting metallurgical structure of the weld and heat affected zone (HAZ).

Gas tungsten arc welding (GTAW) is the most common process used for welding zirconium alloys. GTAW produces acceptable quality but with wider welds due to an inherently higher heat input, when compared to welds produced using laser

beam welding (LBW). The advancement in laser beam welding technology and the advantages it offers has resulted in preferences shifting to the latter. Laser beam welding allows precision, high-quality weld joints to be produced with a low heat input. The low heat input results in a small heat-affected zone, fast cooling rate with very little distortion, and a high depth-to-width ratio. The challenge with LBW is the initial high set-up costs.

1.2 Rationale for the study

A lot of research has been done in understanding the mechanical and metallurgical behavior of zirconium-2.5niobium. The transformation kinetics under equilibrium and the non-equilibrium condition have also been extensively studied. The current research is focused on the application of this knowledge to understanding the transformation behavior during welding of zirconium-2.5niobium and the influence of welding process parameters on the microstructure of weld metal, heat affected zone (HAZ), and the room temperature mechanical properties.

1.3 Research objectives

The objectives of this research are as follows:

- Microstructure characterization of welded zirconium-2.5niobium.
- Determine and compare the fundamental difference in the resulting microstructure between the autogenous laser beam and gas tungsten arc welding.
- Investigate the influence of welding parameters on zirconium-2.5niobium properties.
- Establish the relationship between welding heat input and weld metal cross-sectional area of investigated material
- Establish the relationship between the microstructure morphology and mechanical properties.
- To determine the phase transformation temperatures during cooling (including the monotectoid and martensite start temperature) through dilatometry.

CHAPTER 2

Literature Review

2.1 Historical development of zirconium alloys

Klaproth in 1789 discovered the element zirconium but did not isolate the element into a metallic state. In 1824 Berzelius made some progress but it was not until 100 years later, in 1925, that the production of high purity "crystal bar" zirconium was achieved by Van Arkel and De Boer through the iodide refining process. This method was superseded in 1945 by the much cheaper Kroll process (Northwood, 1985).

The use of zirconium and its alloys in the nuclear industry is credited to Admiral Rickover of the US Navy. He oversaw the development of the Shipping-port Atomic Power Station (Krishnan, 1980). This was the world's first pressurized water reactor (PWR) used for generating electricity. A PWR required a metal which could withstand the harsh environment of high radiation at high temperatures for prolonged periods of time whilst maintaining its integrity, and have a low neutron-capture cross-section.

Zirconium is naturally associated with hafnium which has a high neutron capture cross-section. Kaufman and Pomerance successfully separated hafnium from zirconium and demonstrated that zirconium in its pure form absorbed only a few neutrons. The focus of zirconium development then turned to improving the corrosion resistance properties. As a consequence, the first stage in the development of zirconium was to identify those elements which improved the corrosion behavior. Preliminary research showed that the presence of impurities like nitrogen, carbon, and aluminum in zirconium even in low quantities led to significant degradation of corrosion resistance (Nikulina, 2010). The addition of tin was found to be most effective in counteracting the detrimental effects of impurities on corrosion resistance without seriously affecting the neutron economy. Thus Zircaloy-1 was developed which contained 2.5 weight percent tin (Moorthy, 1969). This alloy was subjected to long-term testing and results showed that the corrosion rate remained essentially high instead of the expected decrease in rate with time (Krishnan, 1980).

Iron and chromium in zirconium were un-intentionally added after a Zircaloy-1 ingot was melted in a furnace which was contaminated with stainless steel. The resultant material proved to have outstanding corrosion resistance. Nickel was also added because of the beneficial effects on high-temperature corrosion resistance. The new alloy was named Zircaloy-2. This alloy performed satisfactorily but there were fears of the detrimental effect of high tin content during service. Therefore it was decided to limit the tin content to the amount just necessary to counteract the nitrogen and other impurities deleterious to corrosion resistance (Adamson, 2007).

As a consequence, an alloy with just 0.25 weight percent tin and 0.25 weight percent iron was recommended, designated as Zircaloy-3. This alloy was abandoned due to lower mechanical properties when compared to Zircolay-2.

Hydrogen absorption during operation from the metal/water reaction was a major problem on Zircaloy-2 because it resulted in low impact values due to the presence of zirconium hydride platelets. Nickel was discovered to increase hydrogen absorption considerably. A decision to remove the 0.05 weight percent nickel addition in Zircaloy-2 was taken. The resultant alloy (that did not contain any nickel) was found to have inadequate corrosion resistance. The iron content was increased, thus a new composition was arrived at with 0.18 to 0.24 weight percent iron, 0.10 weight percent chromium, and 1.5 weight percent tin, designated Zircaloy-4. It was found to perform as well as Zircaloy-2 on steam corrosion resistance while exhibiting half the hydrogen absorption.

The development of the Zircaloy grades (that were exclusively based on the zirconium-tin system) mainly occurred in the United States of America. The Russian work reported at the United Nations conference on the 'Peaceful Uses of Atomic Energy' in 1955 strongly suggested that a zirconium alloy containing 1 to 5 weight percent niobium would have superior mechanical strength and adequate corrosion resistance (Moorthy, 1969). The Russian revelations sparked an interest in corrosion studies of zirconium-niobium alloys in Canada, United Kingdom, Germany, and Scandinavia. Only later did it become evident that only the zirconium-1niobium and the zirconium-2.5niobium alloys were being used commercially in Russian reactors. The zirconium-2.5niobium is commonly known as E125 or UNS Zr60705. Currently, the Canadian CANDU pressurized heavy water (PHWR) and Russian RBMK power reactors use the zirconium-2.5niobium alloy to manufacture pressure tubes.

2.2 The application of zirconium-2.5niobium alloy in CANDU pressure tubes

The pressure tube CANDU reactor design was adopted in 1957 in preference to the pressure vessel design (Langford, 1978). The zirconium-2.5niobium pressure tubes are used to contain the fuel rods and primary coolant. They are approximately 6.3 m in length, have an internal diameter of 104 mm and wall thickness of 4.2 mm. Twelve fuel bundles are placed in each pressurised fuel tube of the reactor. The pressure tubes pass through a Calandria tube containing carbon dioxide and heavy water (that acts as a coolant and a moderator). The coolant is also utilized to remove the heat from the fuel bundles to the steam generators (Cheadle, 1975). Figure 1 shows a typical arrangement of the fuel cell in the core of a reactor (Robertson, 1979).

The pressure tubes in CANDU reactors experience coolant pressures in the range of 10-11 MPa and temperatures between 250 to 310°C. The pressure tube wall, therefore forms the primary pressure boundary in the core reactor (Elliot, 2005).

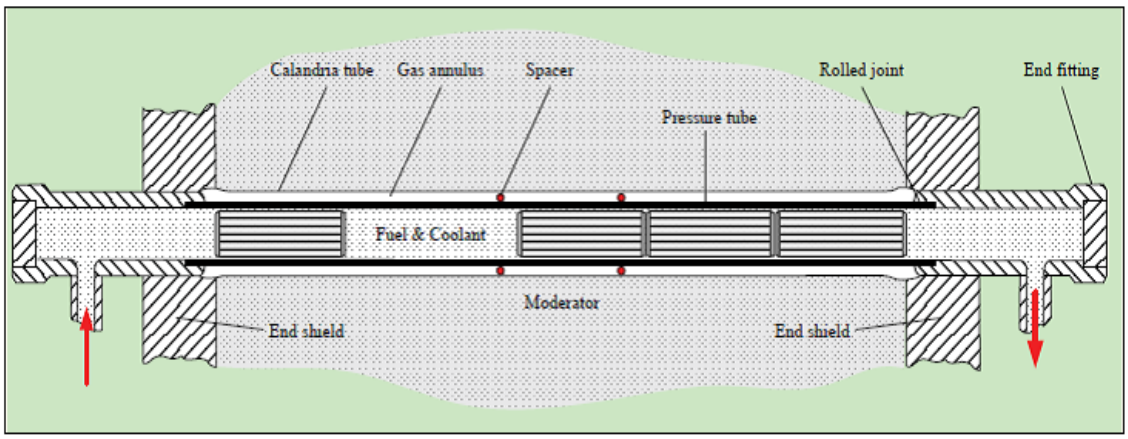

Figure 1: Schematic layout of pressure tube in a CANDU reactor (Robertson, 1979)

During the manufacturing of pressure tubes, they are extruded at around 820 to 850°C, cold worked 20 to 30 percent and stress relieved (autoclaved) in steam at 400°C. At the extrusion temperature, the tube microstructure consists of about 80 percent beta zirconium (β_{Zr}) and 20 percent alpha zirconium (α_{Zr}). During air cooling after the extrusion, the β_{Zr} transforms to α_{Zr} by growing on the existing elongated α-grains produced during the extrusion, while the β_{Zr} becomes progressively enriched in niobium. These α-grains are surrounded by a grain boundary network of metastable β_{Zr}, with a bcc structure, that contains about 18 to 20 weight percent niobium. Cold drawing causes additional elongation of the α-grains and introduces a high density of dislocations. The autoclaving treatment at 400°C in addition to the in-service reactor temperatures around 300°C will transform the β_{Zr} phase to the equilibrium hcp structure phase β_{Nb} (Bordoni, 2005).

2.3 Metallurgy of zirconium-2.5niobium alloy

The generally accepted zirconium-niobium phase diagram is as given in Figure 2 (Massalski, 1992). Zirconium-2.5niobium alloy exhibits two equilibrium phases at room temperature namely alpha (α_{Zr}) phase with the hexagonal close-packed crystal structure (hcp) and niobium-rich body-centered cubic (bcc) beta phase (β_{Nb}). At temperatures above about 860°C, a beta ($\beta_{Zr,Nb}$) phase with bcc structure exists (Banerjee, 2010). The single phase α and single phase β regions are separated by a two-phase region of (α_{Zr}+β_{Zr}) between 620-860°C. A monotectoid reaction occurs at a 18.5 atomic percent niobium composition and 620°C temperature. In the zirconium-2.5niobium alloy, a single β phase present at temperatures above ~860°C progressively transforms to α phase with a decrease in temperature. The maximum solubility of niobium in α phase is 0.6 atomic percent; therefore the β phase becomes increasingly enriched with niobium as the volume fraction of α phase grows until the monotectoid composition of 18.5 atomic percent niobium is reached.

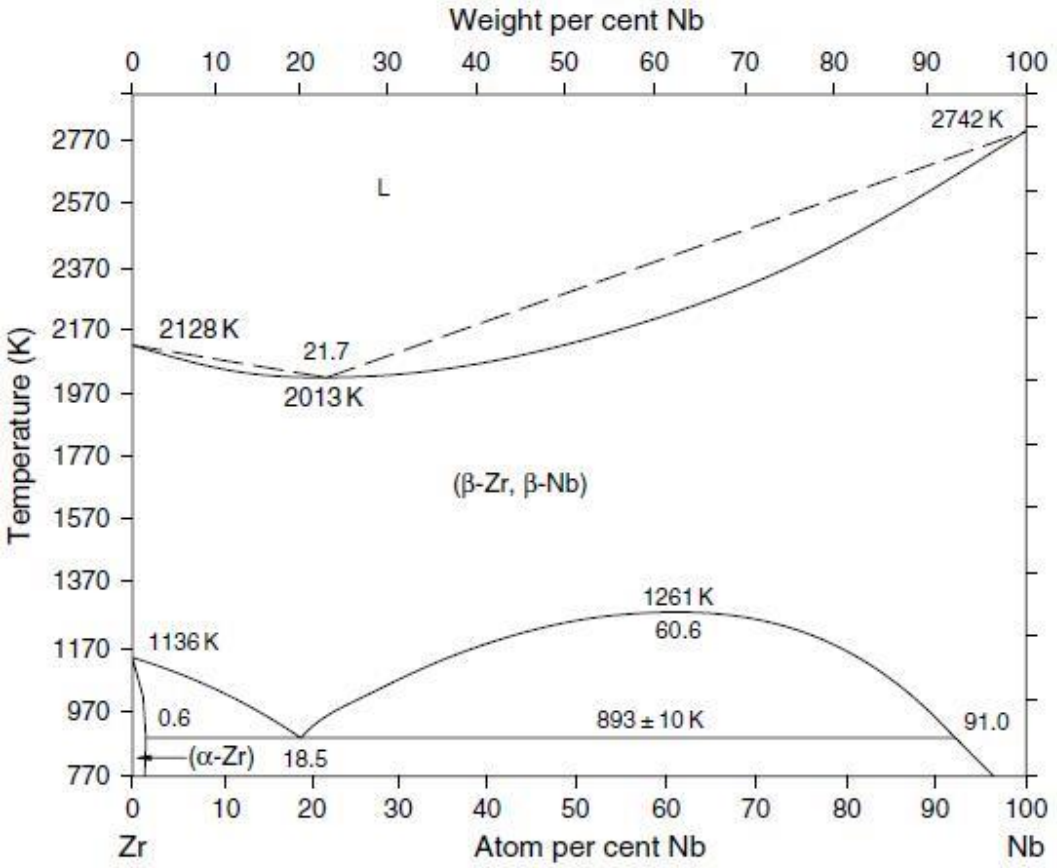

Figure 2: Zirconium-Niobium Binary Phase Diagram (Massalski, 1992).

Below is a list of possible solid phase transformations in zirconium-2.5niobium Alloy (Yuan, 2015)

- $\beta_{Zr, Nb} \rightarrow \alpha'$ occurs during quenching (fast cooling).
- $\beta_{Zr, Nb} \rightarrow \omega$ occurs during quenching or aging at low temperature.
- $\beta_{Zr, Nb} \rightarrow (\alpha + \beta_{Zr})$ normal transformation during slow cooling.
- $\beta_{Zr, Nb} \rightarrow (\alpha + \beta_{Nb})$ this reaction is associated with very sluggish decomposition kinetics which is why retained β_{Zr} is normally observed.
- $\alpha' \rightarrow \alpha + (\beta_{Zr}$ or $\beta_{Nb})$ during tempering or aging.

where:

$\beta_{Zr,Nb}$: body-centered cubic (bcc) structure stable in a single phase region at a temperature between 860-1840°C.

β_{Zr}: bcc crystal structure stable in the $(\alpha+\beta_{Zr})$ two-phase region between 620-860°C with the maximum composition of 18.5 atomic percent niobium.

α: hexagonal close-packed (hcp) crystal structure equilibrium phase with maximum solubility of 0.6 atomic percent niobium at room temperature.

β_{Nb}: niobium-rich bcc crystal structure equilibrium beta phase, stable below the monotectoid temperature (620°C) with the maximum composition of 91 atomic percent niobium.

α': hcp non-equilibrium martensite phase.

ω: hcp metastable omega phase which transforms from aging retained beta ($\beta_{Zr,Nb}$) at low temperatures.

Non-equilibrium phases such as the martensite phase can manifest as either hcp (α') and orthorhombic (α'') crystal structure. The ω-omega phase and a large number of metastable intermetallic phases also occur in binary zirconium-niobium base alloys. The metastable ω-omega phase has an hcp crystal structure and transforms from the decomposition of retained beta ($\beta_{Zr,Nb}$). The beta to omega ($\beta_{Zr,Nb} \rightarrow \omega$) thermally activated transformation occurs after prolonged ageing at low temperatures (below 500°C, depending on the alloy composition). The orthorhombic martensitic α'' phase, which forms in alloys containing large concentrations of β-stabilizing elements, can be considered as a distorted hexagonal phase (Banerjee, 2010).

As is seen from the phase diagram and the transformation list above, the zirconium-niobium system is a heat-treatable alloy with complex transformation products. When an alloy containing 2.5 weight percent niobium is rapidly quenched from beta phase, a martensitic type of transformation occurs to alpha zirconium containing niobium in a supersaturated solution. It has been observed experimentally that good properties are shown by the material which has been quenched from the alpha plus beta phase, cold-worked and aged in the high alpha region (500-600°C). Increasing the niobium content increases both the as-quenched hardness and the aging response. On the other hand, increasing the two constituents decreases the ductility. Worst properties are shown by materials slow-cooled through the alpha plus beta region.

Retention of the β-phase during quenching has been found to be feasible in the binary zirconium-niobium systems. Retained large volume fractions of a metastable, β_{Zr} phase have been observed in relatively solute-lean alloys (Zr-2.5Nb and Zr-5Ta) (Banerjee, 1976).

As with the cooling rate, the heating rate has a notable influence on the transformation dynamics. The α-β phase transformation temperature range is shifted to higher values with an increase in heating rate. This is shown in Figure 3, which are dilatometric results of work done by Forgeron (2000) on a zirconium-1niobium alloy. From the work by Forgeron, it seems the phase volume fraction and the effect of heating rate on transformation temperatures can be determined from dilatometry experiments (Forgeron, 2000).

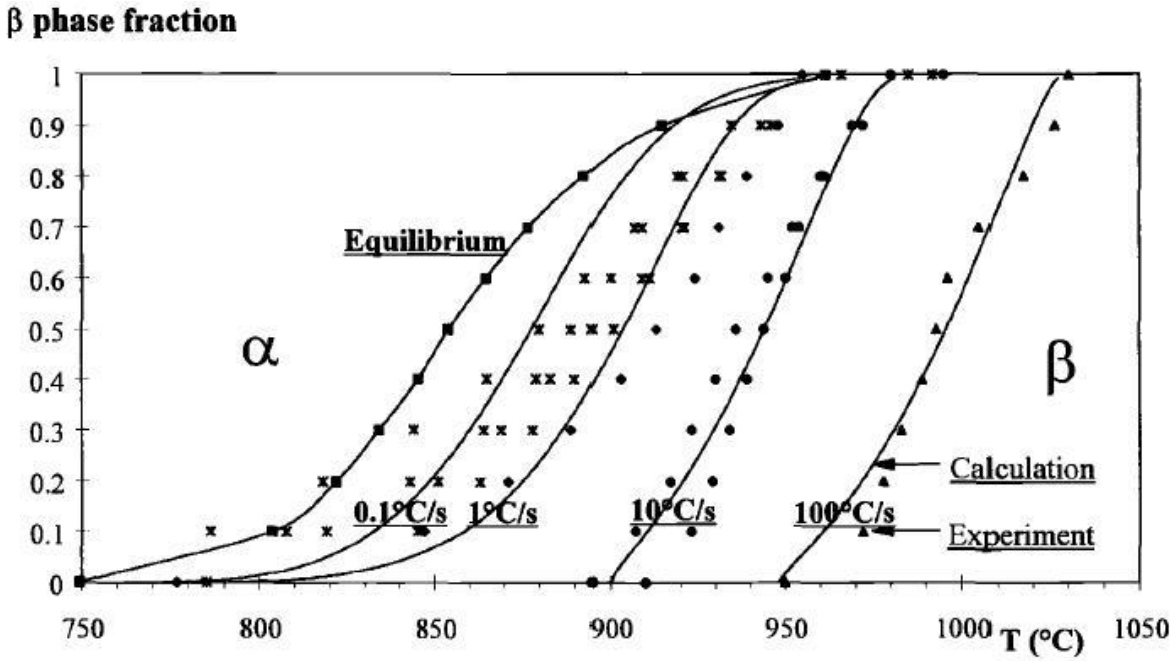

Figure 3: Experimental and calculated a-β phase transformation for several heating rates (Zr-1Nb Alloy) (Forgeron, 2000)

2.3.1 Alloying elements in zirconium, other than niobium

Alloying elements have an important effect on the α to β phase transformation temperature. Some elements stabilize the α-phase by raising the transformation temperature while some others lower it, thereby stabilizing the β-phase. Elements which cause the transformation temperature to increase are known as α stabilizers. These elements are generally non-transition metals and interstitial elements like aluminium, tin, carbon, nitrogen and oxygen. Elements which decrease the transformation temperature are termed β stabilizers and these elements include niobium, iron, chromium, nickel, and molybdenum.

Most of the elements have a very limited solubility in α_{Zr}, with a few exceptions such as titanium, hafnium, nitrogen and oxygen mainly due to the relatively large size of the zirconium atom. On the contrary, β_{Zr} is a much better solvent, but it is generally quite difficult to retain the β-phase at room temperature in a metastable state by quenching (Froes, 1996).

Alloying elements added to zirconium above the solubility limit may form chemical compounds and second-phase particles. These compounds and particles tend to lower the ductility of zirconium alloys and have been found to influence the final microstructure, by acting as nucleation sites for the alpha plates (Krueger, 2015).

Oxygen was initially considered an undesirable impurity but that changed after its strengthening effect on zirconium was realized. All conventional zirconium-niobium alloys contain dissolved oxygen and there are two main reasons why it should be given special consideration. Firstly, oxygen is an α_{Zr} phase stabilizer and thus increases the β/α+β phase transformation temperature. Experimental work has

shown that the effect of oxygen on the transformation temperature is given empirically by equation 1 (Moorthy, 1969) below.

$$T=871+0.8(A-1000)\ ^{\circ}C \qquad [1]$$

where (A) is the dissolved oxygen content in ppm. This empirical equation was based on measurements of zirconium2.5niobium β/(α+β) trunsus temperatures with oxygen contents ranging from 400 to 1800 ppm. Figure 4 below shows the influence of oxygen on the equilibrium β/α+β transformation temperature in different zirconium-niobium alloys. The effect of increasing oxygen content from 1420 to 5350 ppm in zirconium 2.5 weight percent niobium resulted in a ~220°C rise of the β/α+β transformation temperature. Secondly, oxygen is known to have a significant influence on the solubility of niobium in α_{Zr} and, therefore, a change in oxygen content will change the super-saturation of niobium and the precipitation kinetics.

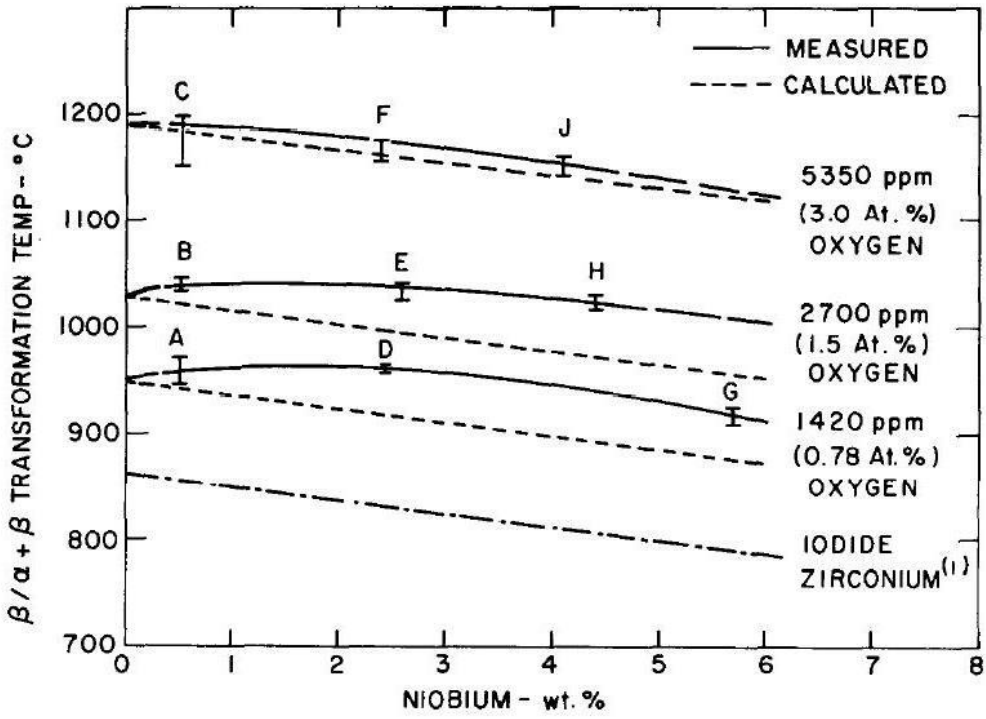

Figure 4: Oxygen concentration influence on the β/a+β transformation temperature (Hunt, 1970).

2.3.2 Phases present in the zirconium-2.5niobium alloy

2.3.2.1 Alpha phase (a_{Zr})

Figure 5 shows a typical microstructure of zirconium-2.5niobium α phase which had been furnace cooled after solution treatment at 950°C (β phase region). The microstructure at a lower magnification consists of irregular α plates whose orientation and arrangement in the prior β grains reflect the number of crystallographic variants of the β→α transformation, and the darker phase is retained beta (Perovic, 1989). At higher magnification (image B), the α/β interface

consists of arrays of dislocations whose density changes in a systematic way as the local orientation of the interface plane changes.

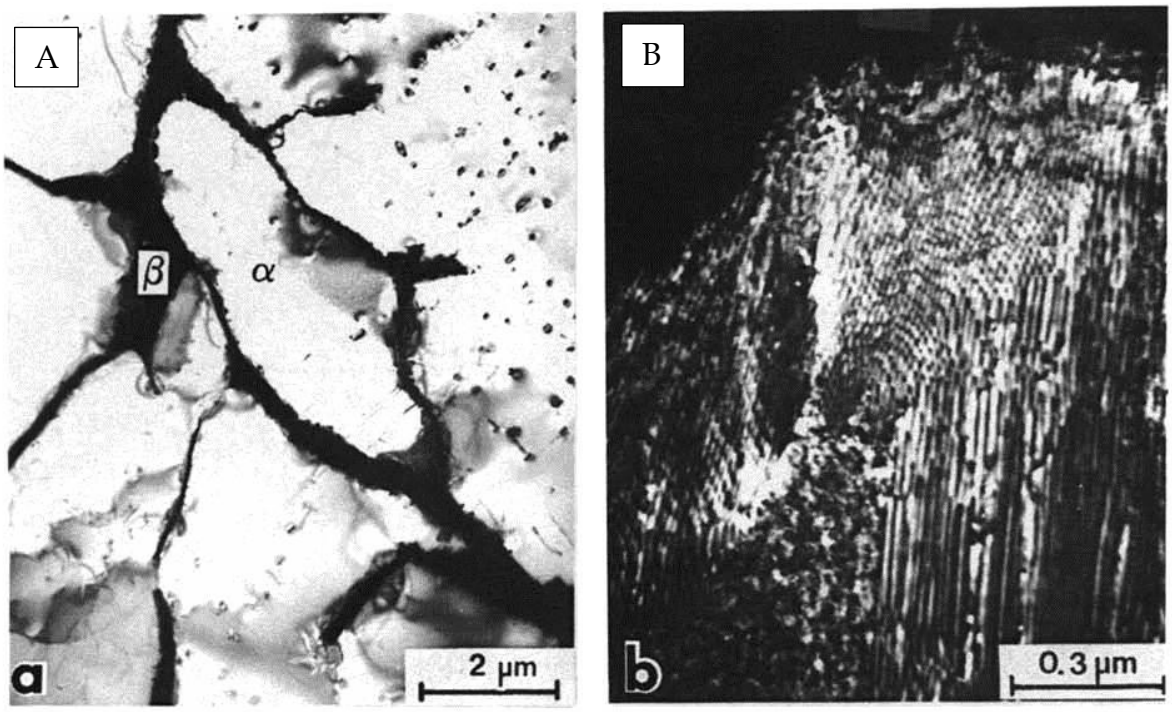

Figure 5: Zr-2.5Nb furnace cooled alpha phase after solution treatment at 950°C (Perovic, 1989).

Many theoretical models have been developed in an attempt to understand the morphological development and possible interfacial structures that form during the diffusion controlled transformation of bcc beta to hcp alpha. One of the models by Dahmen showed that the product phase in many transformations grows as a lath or needle parallel to an invariant line of the phase transformation, with the orientation relationship being determined by the restrictions imposed by the invariant line criterion (Perovic, 1989). This same principle has been found to control the growth direction of α plates in β_{Nb}.

For an intermediate cooling rate, the first plates to appear during α precipitation are grain boundary allotriomorphs (GBA) which form along the high angle grain boundaries of the parent β-phase, Figure 6. The alpha plate establishes a Burger orientation relationship with one of the two adjacent beta grains to ensure a low interfacial energy and favorable nucleation kinetics (Banerjee, 2010).

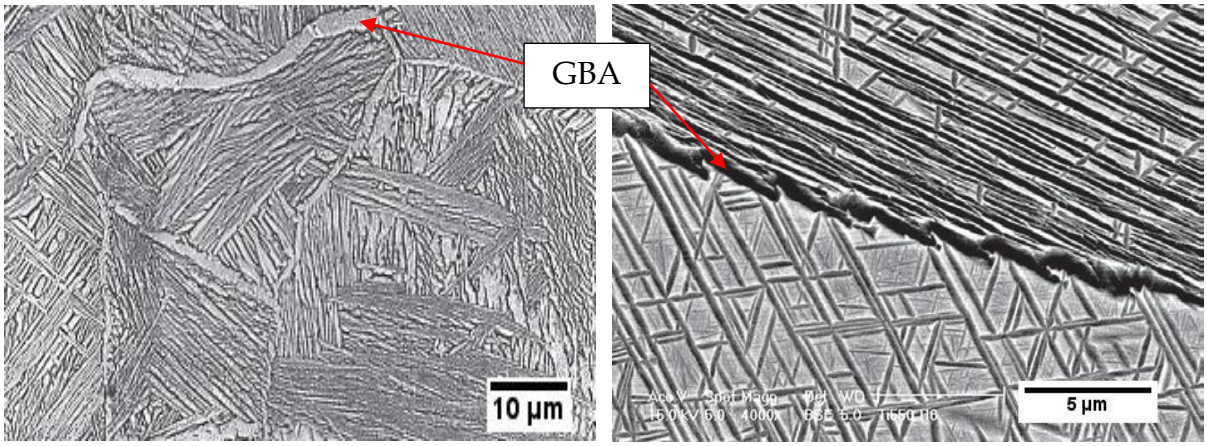

Figure 6: Intermediate cooled alpha phase at different magnification.

GBA nucleating along the prior β grain boundary and secondary alpha plate nucleating from GBA at higher magnification on the right (Banerjee, 2010).

Alpha phase may exhibit a Widmanstätten structure which manifests itself into two morphologies called parallel plates and basket-weave (Holt, 1969). The parallel plate structure consists of a number of long α_{Zr} plates that precipitate and grow on the same habit plane from the grain boundary or by branching from the GBAs. Another parallel morphology is the intragranular alpha plate which nucleates within the beta grain. These plates can form in isolation or in a colony and still obey a strict orientation relationship as seen in Figure 7. The plates continuously partition the prior beta grain into smaller and smaller volumes with new generations of plates appearing.

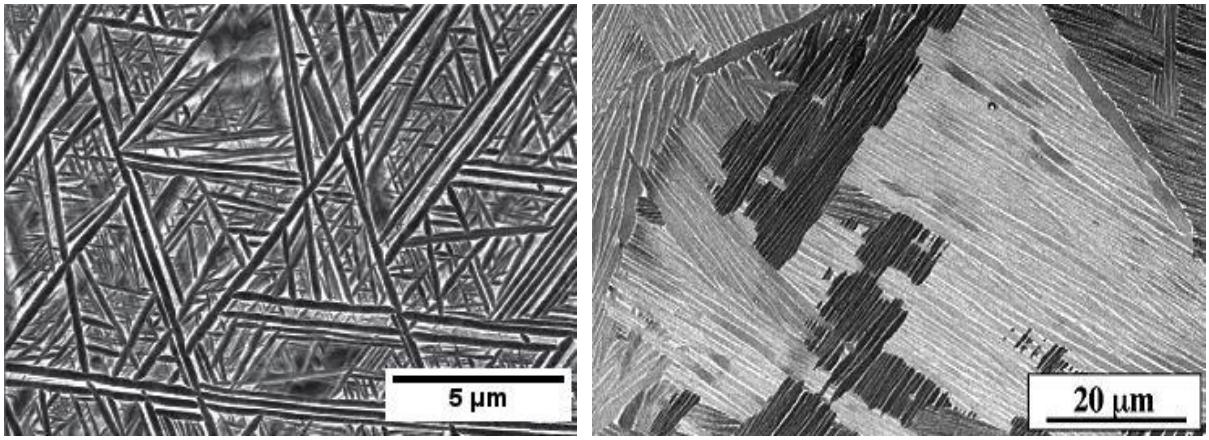

Figure 7: Basketweave and parallel Widmanstätten structure of the alpha phase (Banerjee, 2010).

Basket-weave morphology, in contrast, is composed of the nucleation and growth of parallel intragranular plates that randomly precipitate on a number of planes within the same parent β grain. A basket-weave structure is promoted by an increase in cooling rate and the presence of randomly dispersed second phase particles in the parent β phase.

2.3.2.2 Martensite (α')

Zirconium-niobium alloy can experience a martensitic transformation to form hcp α´ martensite from the supersaturated bcc beta during an increased cooling rate. Generally, zirconium martensite exhibits two types of morphologies, referred to as lath (massive) martensite and plate (acicular) martensite. Pure zirconium with a total niobium content less than 0.8 atomic percent shows massive twin-free martensite laths whereas acicular twinned plates are dominant at higher niobium contents. The transition from lath to plate morphology is not sudden and the two may co-exist over a range of compositions. The substructure within a given martensite plate on the zirconium-niobium alloy is generally a mixture of dislocations and a twinned structure. Some observations have been made based on the M_s temperature which is a composition attribute. Acicular twinned plate morphology is seen in alloys with M_s temperatures below 650 to 700°C, while a massive slipped lath morphology is present in alloys with a higher M_s ranging between 650 to 900°C (Banerjee, 1997). A further consequence of increasing niobium content on the morphology of martensite is the increase in the volume fraction of the total number of plates that are twinned while the plate size decreases (Banerjee, 1971). It has also been shown that increasing the quenching rate results in an increase in the volume fraction of the internally twinned primary martensite plates (Srivastava, 2000).

A further description of the different martensite morphologies is explained below with an accompanying microstructure of zirconium-2.5niobium alloy shown in Figure 8.

1. Martensite can have a morphology of alternate laths belonging to the two twin-related variants. Lath units are grouped together in parallel arrays within a packet and several such packets make up the volume of the parent β grain.
2. Internally twinned martensite plates with thick twins are often present in zirconium-2.5niobium. This morphology is observed in primary plates which partition the parent β grain. Secondary plates form within the untransformed β phase and the process continues until the transformation is complete
3. An indentation-like morphology which generally forms in the last stage when the untransformed phase undergoes an instantaneous transformation. In appearance, this morphology shows a group of three martensite plates which are mutually twin related on $\{10\bar{1}1\}_\alpha$ planes (Banerjee, 1997).

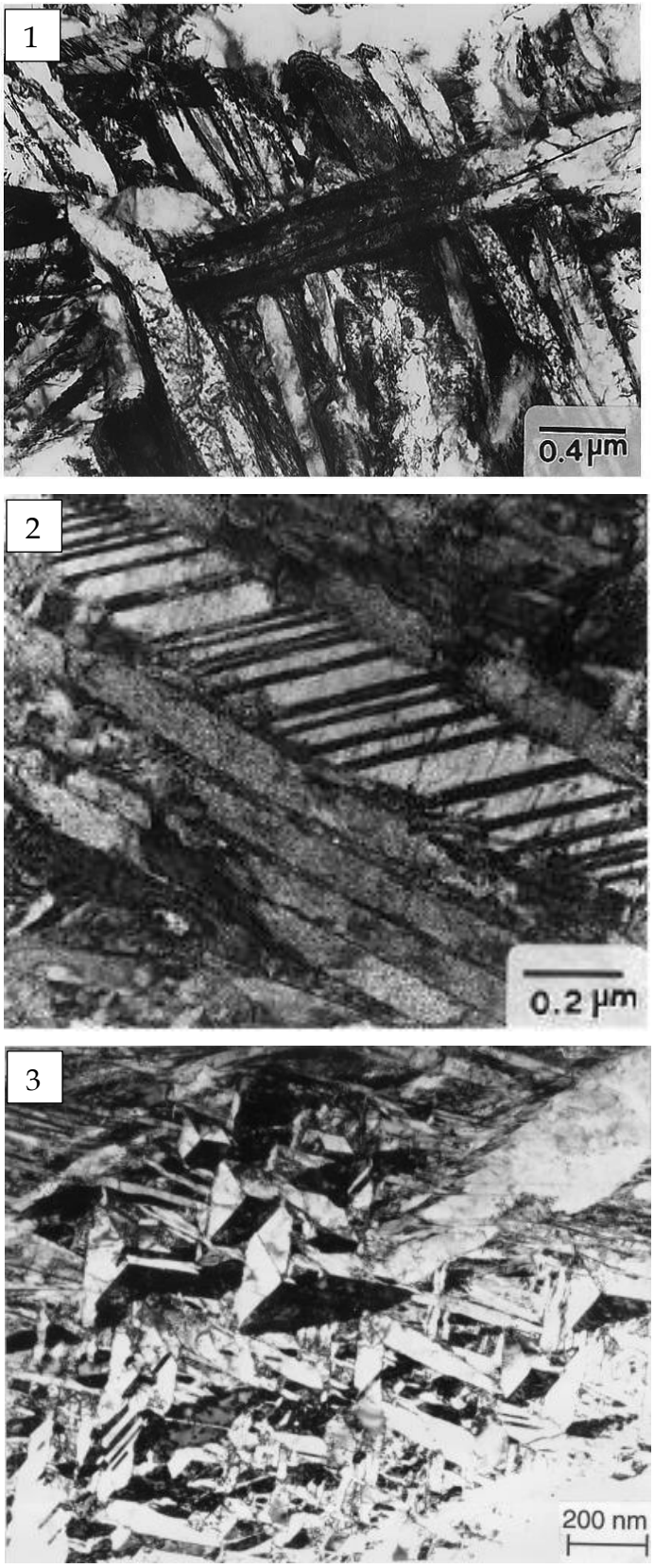

Figure 8: The different martensite morphologies of the Zr-2.5Nb alloy (Srivastava, 2000).
1. Alternate laths belonging to two twin-related variants, 2. Internally twinned martensite plates, 3 indentation-like morphology

The zirconium alloys martensite transformation start (M_s) temperature has been shown to be approximately 50°C below the T_o temperature (Kaufman, 1959). T_o is the temperature where the free energies of the parent beta phase and martensite are equal. This temperature is relatively low and implies that only a small amount of undercooling is needed to initiate the martensite transformation ($\beta \rightarrow \alpha'$). The small undercooling is sufficient because the necessary lattice strains approximately satisfy the invariant plane strain condition for the $\beta_{Nb} \rightarrow \alpha'$ martensitic transformation. The surface energy associated with the creation of the new β/α' interface and the strain energy from martensite formation is small, therefore the magnitude of driving force required for the transformation is also small (Kaufman, 1959).

The martensite start (M_s) temperature is independent of cooling rate, oxygen content, and β phase solution treatment temperature and time but decreases as the niobium content increases. Figure 9 shows the zirconium-2.5niobium M_s temperatures as reported by three authors namely McMullen, Higgins and Hunt of between 670-690°C (Abriata, 1982). The dotted line shows M_s temperatures as reported by Cometto much earlier in 1959.

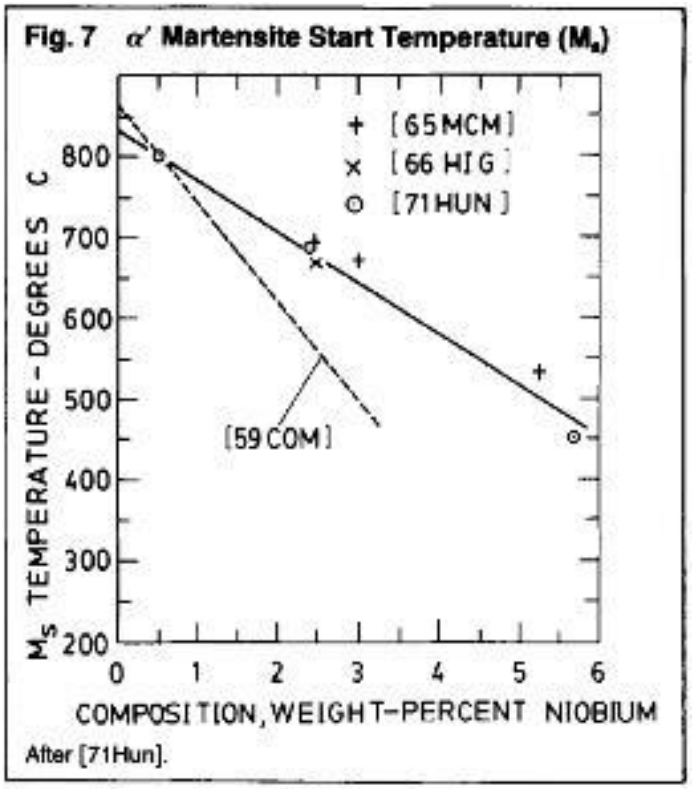

Figure 9: Martensite start temperature of Zr-Nb (Abriata, 1982).

Three authors reported M_s temperatures in good agreement of 670°C ±10 for Zr-2.5Nb alloy with an oxygen content of 400-700 ppm.

2.3.2.3 Beta (β_{Nb})

Beta niobium is an equilibrium phase found at room temperature in the zirconium-niobium system. The composition has been found to contain 91 atomic percent niobium at room temperature (Yuan, 2015). There are two mechanisms by which β_{Nb} can form during heat treatment under nonequilibrium conditions: nucleation and growth of new β_{Nb} particles and in-situ transformation. These two mechanisms can occur simultaneously. (Robson, 2008)

- *Nucleation and growth mechanism*: This mechanism will occur when the beta phase ($\beta_{Zr,Nb}$) is quenched to form a supersaturated α' martensite. Due to the absence of any retained β_{Zr} phase after quenching, direct nucleation and growth of the β_{Nb} phase are observed during aging heat treatments.
- *In-situ transformation*: slow cooling from the beta phase ($\beta_{Zr,Nb}$) will result in an alpha zirconium (α_{Zr}) matrix with retained beta-zirconium (β_{Zr}) along the grain boundaries. The retained β_{Zr} phase is metastable and will transform to α_{Zr} and β_{Nb} when tempered. The transformation of retained β_{Zr} to β_{Nb}, when aged below 530°C, involves an intermediate step in which a metastable hcp omega (ω) phase is observed. The metastable omega phase will, with time at elevated temperature, transform to α_{Zr} and β_{Nb}. At temperatures above 530°C, the transformation $\beta_{Zr} \rightarrow \alpha_{Zr} + \beta_{Nb}$ will occur without the formation of the metastable omega phase. In some instances, the retained β_{Zr} is found within the supersaturated α_{Zr} matrix. Under these circumstances, the niobium in the supersaturated α_{Zr} phase will diffuse to the retained β_{Zr} which will drive its transformation to β_{Nb}.

2.3.3 Plastic Deformation of zirconium-2.5niobium

The hcp crystal structure of the zirconium alpha phase has a smaller than ideal c/a lattice dimension ratio of 1.593, therefore it tends to slip prismatically instead of the basal plane out of reach, but reverses back to basal slip under irradiation in a LWR environment. Figure 10 shows the important planes in the hcp structure. The predominant slip system is $\{10\bar{1}0\} <\bar{1}012>$. At higher plastic strains and at elevated temperatures slip on pyramidal planes such as $\{11\bar{2}1\}$ and $\{10\bar{1}1\}$ become operative which accounts for the high ductility of the alpha-zirconium phase (Song, 1995).

Twinning also plays an important role in plastic deformation of zirconium with a number of twinning systems available depending on the temperature, strain rate and type of loading. Twinning results in the reorientation of the crystal axes within a region of a crystallite (Cochrane, 2013). The overall magnitude of deformation due to twinning is generally small relative to that caused by slip; however, the orientation change in the lattice may be large, thereby restabilizing orientations that are favorable for slip (Tenckhoff, 2005). Under tensile stresses along the c-axis at ambient temperatures, $\{10\bar{1}2\} <\bar{1}011>$ and $\{11\bar{2}1\} <\bar{1}\bar{1}26>$ twin systems are activated, with the latter twin operating less frequently (Yoo, 2002).

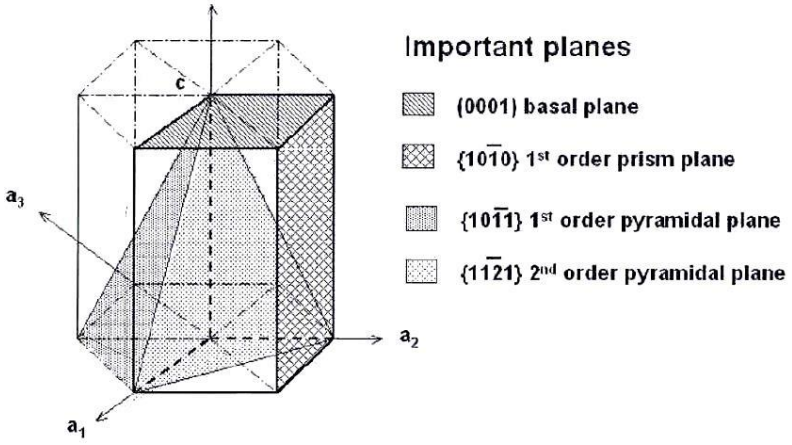

Figure 10: Schematic HCP crystal structure showing the important planes (Tenckhoff, 2005)

Which deformation mode is activated first between the twin and slip is often dependent on the crystallographic orientation even though the critical resolved shear stress (τ_{RSS}) is higher for {10$\bar{1}$2}<$\bar{1}$011> twinning than for prismatic slip at ambient temperatures (Song, 1995). A material will initiate deformation if τ_{RSS} is greater than a critical activation stress associated with that particular system, and this difference can be used to predict which mode occurs first.

2.3.4 Mechanical Properties of zirconium-2.5niobium

2.3.4.1 Tensile strength

Because of the role of the pressure tube as a secondary containment for hot, pressurized coolant, its integrity and reliability are essential to the safe operation of a nuclear reactor of this design. The minimum tensile property requirements for R60705 (zirconium-2.5niobium) sheet in the recrystallized annealed condition as stipulated in ASTM B551, are presented in Table 1. The typical tensile results for zirconium-2.5niobium were reported by Banerjee (2001). Included are Zircaloy-2 properties for comparison purposes.

Table 1: Properties of zirconium-2.5niobium and Zircaloy-2 alloy in recrystallized annealed condition(Banerjee, 2001) against the ASTM B551, 2009 standard

Alloy	UTS (MPa)	0.2% YS (MPa)	Elongation (%)
Zr-2.5Nb (ASTM B551)	550 (min)	380 (min)	16 (min)
Zr-2.5Nb	650	600	12
Zircaloy-2	580	420	18

2.3.4.2 Hardness

Three zirconium-2.5niobium alloys were hardness tested by Sabol (1970) and below in Table 2, are the results. These zirconium-2.5niobium alloys were quenched from 985°C after soaking for 15 minutes. The microstructure was internally twinned α' acicular martensite plates.

Table 2: Hardness results using Vickers hardness testing with a 200g load (Sabol, 1970)

Alloy	O (ppm)	Fe (ppm)	N (ppm)	Hardness ($HV_{0.2}$)
High Purity Zr-2.4Nb	161	70	91	178
High Purity Zr-2.46Nb-Cu	90	< 50	-	202
Commercial Zr-2.6Nb	800	1000	100	254

Hardness results of zirconium-2.5niobium that had been surface treated with a pulsed laser where cooling rates exceeded 6000°C/s, almost doubled to above 400 $HV_{0.1}$ from a base metal hardness of 220 $HV_{0.1}$. Zirconium-2.5niobium therefore, has the capability to harden significantly under certain conditions and this is attributed to several factors:

1. The martensitic transformation which produces very fine twinned α´ plates separated by high angle boundaries in comparison to the prior large α grains in the thermo-mechanically treated base metal. The martensitic transformation results in grain-refinement hardening due to the Hall-Petch effect.
2. It has been confirmed that twin boundaries can be a more effective barrier to the dislocation slip than a grain boundary.
3. Solid solution hardening due to super-saturation of niobium on the α´ plates. With complete transformation to a martensitic structure where no residual beta phase exists, the alpha phase is saturated with the alloying elements (Chai, 2015).

A combination of these factors can lead to significant hardening of the zirconium-2.5niobium (Chai, 2015).

2.4 Welding of zirconium

Welding of zirconium components is one of the most critical manufacturing processes in a nuclear reactor. Zirconium alloys have shown good weldability using welding techniques such as gas tungsten arc welding (GTAW) and laser beam welding. Zirconium is a reactive metal and therefore susceptible to contaminants like hydrogen, nitrogen, oxygen, and carbon at temperatures above 370°C (Krueger, 2015). Zirconium can also dissolve up to 50 atomic percent oxygen and 25 atomic percent nitrogen as a solid solution in the alpha phase (Lustman, 1955). The

susceptible to contaminants is the reason why pure argon and helium (or a mixture) are the only shielding gases recommended. Thorough cleaning of the work-piece before welding is essential. Contamination causes embrittlement which results in an increase in hardness but the loss of ductility. Adequately shielded welds should show bright silver weld beads. When contaminated, as seen in Figure 11, zirconium welds show a range of discoloration from dark straw to blue for light contamination to dark blue or grey for severe contamination (Krueger, 2015).

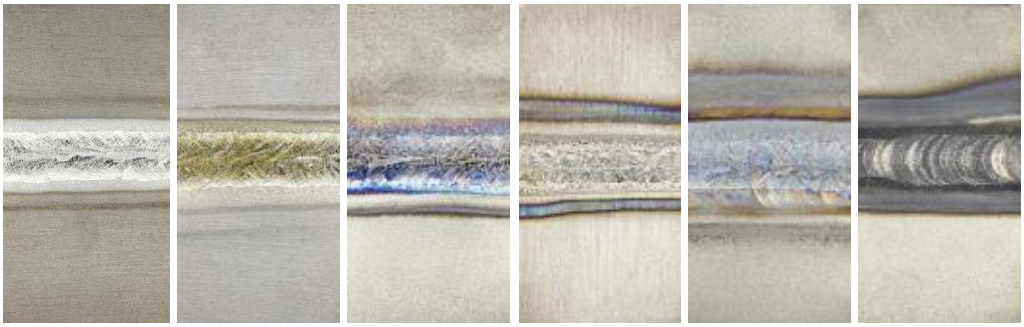

Figure 11: Weld Bead coloration and discoloration in zirconium (Krueger, 2015).

The weld puddle, solidified weld, and heat affected zone must, therefore, be protected until the temperature has cooled below 427°C (800°F) as recommended by AWS G2.5/G2.5M;2012 (American Welding Society, 2012).

The common zirconium weld discontinuities are lack of fusion, incomplete penetration, under-fill, and porosity. Majority of these discontinuities are caused by incorrect welding parameters, inadequate shielding, and poor cleanliness. Zirconium-niobium is also susceptible to delayed hydrogen cracking.

To minimize the hydride platelets causing cracking, post weld heat treatment (PWHT) is a mandatory requirement within 14 days of welding (AWS, 2012). The parameters for PWHT are 540-595°C for a minimum of 1 hour for thicknesses up to 25mm (1 inch), plus 0.5 hours for each additional inch of thickness (ASME, 2010). The PWHT will relieve the residual stresses and allow diffusion of hydrogen out of the welded component.

During welding, microstructural changes occur resulting in unfavorable changes in mechanical properties. The performance of zirconium alloys is very sensitive to its microstructure which is a result of chemical composition and thermal treatment. The weld fusion and the heat affected zone represent a large range of heat treatments. The fusion zone has reached the highest temperature, while the area in the HAZ furthest away from the fusion zone had the lowest peak temperature. This heat treatment range means that a weld (fusion and HAZ) will show a large variety of microstructures, some of which may have very poor properties.

CHAPTER 3

Welding Processes and Characterisation

3.1 Welding Process

Fusion welding is a process that involves a very intense, moving heat source applied to the workpiece that leads to melting. There are mainly three classifications of fusion welds; autogenous, homogenous, and heterogeneous. The latter two utilize a filler metal during welding and will not be applied in this research. Autogenous welds are those where no filler metal is added and the fusion zone is formed by the melting and re-solidification of the base metal. In homogeneous welds, the filler metal composition closely matches that of the base metal, whereas in heterogeneous welds the filler metal is different from the base metal composition (Lippold, 2014). Autogenous welding was applied during the current study because the base metal sheets used have a 1.5 mm thickness and the desired full penetration will be achieved without difficulty on all welds. The risk of altering the weld composition and contamination is also limited. Autogenous welds are commonly used in situations where section thicknesses are minimal and penetration can easily be achieved by the process selected. The fusion zone has essentially the same composition as the base metal, except for possible losses due to evaporation or pickup of gases from the shielding atmosphere.

The thermal cycle or temperature distribution in the welded component is a function of heat input. Experimentally, it is difficult to make measurements of the thermal cycle within the weld pool and the workpiece as a whole. Thus theoretical analysis has been attempted to predict the thermal cycles even though a few assumptions are required. Satisfactory agreement has been obtained between measured and theoretical temperature profiles in the heat-affected zone, especially using the heat-flow equations of a moving point heat-source given by Rosenthal in 1935 (Easterling, 2013)

This study is concerned with mainly two fusion welding processes namely the laser beam and gas tungsten arc welding.

3.1.1 Laser Beam Welding (LBW)

In this process, moving high density coherent optical energy is focused on a small spot on the material to be welded. The laser beam has the ability to generate a power density of greater than 10^6 W/cm^2 and the absorption of such energy by the material leads to melting and evaporation. There are two applicable modes of welding namely the conductive and deep penetration mode. The deep penetration mode, commonly known as the key-hole mode, is when vaporization of the material occurs to create a hole as shown in Figure 12. The hole assists in the absorption of the laser

beam energy into the material. The keyhole is prevented from closing by the vapor pressure, the hydrostatic stability of the molten material, and surface tension forces (Weman, 2011). As the laser beam moves together with the cavity, the molten material must move continuously from the front of the cavity to the cooler trailing region behind (Mazumder, 1993). The laser beam is reflected multiple times on the walls of the keyhole and the molten material of the keyhole walls absorb the power of the beam. With a high welding speed, the process gives a parallel sided fusion zone, narrow weld, and high welding efficiency. The weld depth may be ten or more times greater than the weld width. The high accuracy and reduced distortion of keyhole welding have made this process common in many applications requiring deeper welds.

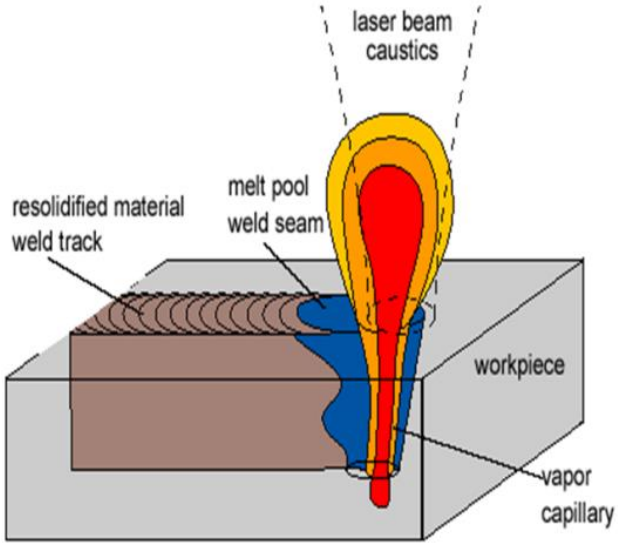

Figure 12: A schematic example of a key-hole mode in laser welding

Process parameters as stipulated in ISO 15609-4 (2009)

1. Beam parameters :
    a. Laser beam power
    b. Laser beam orientation
2. Mechanical parameters
    a. Travel speed
    b. Wire/filler feed rate, direction, if any
3. Shielding and backing gas parameters
    a. Gas flow rate
    b. Gas purity
    c. Purge procedure
4. Working distance
5. Shape and dimensions of the beam on the workpiece

ASME IX (2010 ASME Boiler and Pressure Vessel Code) specifies the variables listed in Table 3 for qualification of the laser beam welding procedure specification. Only the relevant ASME parameters (variables) were included.

Table 3: LBW welding variables procedure specifications as per ASME IX (2010).

ASME IX Paragraph		Process variable
QW-402 Joints	.1	Groove design
QW-403 Base metals	.3	Penetration
QW-408 gas	.2	Single, mixture, or %
	.12	Flow rate
QW-409 Electrical characteristics	.20	Mode, energy
	.21	Power, speed
QW-410 Technique	.17	Type/model of equipment
	.37	Single to multiple pass
	.77	Wavelength
	.80	Spot size

The effect of the important laser beam welding process variables are discussed below (Mazumder, 1993).

1. Welding speed: the penetration depth reduces as the welding speed is increased.
2. Incident laser beam power: for a given beam diameter, penetration increases linearly with incident laser power. This is because the power density is a function of both the incident beam power and beam diameter.
3. Beam diameter: the beam diameter determines the power density.
4. Absorptivity: this is the efficiency at which light energy is absorbed by the workpiece from the incident laser beam power. Absorptivity is a function of the electrical resistivity of the workpiece. The efficiency can be improved by adding reactive gases to the shielding gas and by using the key-hole mode.

Laser energy transfer efficiency (η_w) is the proportion of the energy that is absorbed by the workpiece over the incident laser energy. (Sokolov, 2014)

$$\eta_w = \frac{E}{P \times t} \qquad [2]$$

where: E: total energy absorbed by workpiece (Joules)
P: laser output power (W or Joules/s)
t: laser time (s)

There are two mechanisms that describe the energy absorption through the keyhole. The first mechanism refers to the beam absorption at the solid/liquid surface of the material on the keyhole wall and the second one takes place in the partially ionized

plume of vapor in the keyhole. The absorption levels can be influenced by surface roughness, wavelength and process parameters.

The LBW provides increased processing speed, less post-processing, reduced consumption of materials and the possibility of automation, leading to increased productivity. The disadvantages of this welding technique are high costs of laser apparatus, difficulty in melting highly reflective or highly thermal-conductive metals and a low tolerance for variation in the root opening.

3.1.2 Gas Tungsten Arc Welding (GTAW)

The GTAW process involves initiating an arc between the non-consumable tungsten electrode and the workpiece to form a weld pool. The arc can be initiated by either using a high-frequency generator which produces a spark necessary for the initial conducting path or through the 'lift-arc' method where the electrode is lowered to touch the workpiece and on lifting, the arc strikes (Weman, 2003). With the latter process, a special power source controls the current to correct levels.

The electrode is not consumed during welding and therefore requires special properties like low electrical resistance, high melting point, good emission of electrons and high thermal conductivity. The best material for these required properties is tungsten. The tungsten electrode is usually alloyed with thorium oxide to improve arc stability and ease of striking (Weman, 2003). An inert gas (usually pure argon, helium or a mixture) coming through the cup on the welding gun, shields both the weld pool and the electrode. This welding process can be operated in different modes namely direct current electrode positive or negative (DCEN or DCEP) and alternating current (AC). During DCEN, electrons are discharged from the tungsten electrode and accelerated through the arc to the workpiece at a very high speed. These electrons collide with the workpiece to generate heat which causes melting. This mode results in a high heat input, deep penetration, and narrow welds. The opposite occurs when operating with DCEP where the electrons accelerate toward the tungsten electrode. Less heat input on the workpiece results with shallow welds. The AC mode results in mixed characteristics of both DC modes during the corresponding half cycles (Messler, 1999).

Process parameters for GTAW (ISO 4063:2010)

1. Welding current
2. Polarity
3. Gas type and purity
4. Gas volume
5. The distance between electrode and workpiece (arc length)
6. Welding speed
7. Torch position
8. Diameter of electrode
9. Tip angle of electrode

10. Welding Position.

For qualification of the GTAW welding procedure specification, ASME IX (2010 ASME Boiler and Pressure Vessel Code) specifies the variables listed in Table 4.

Table 4: GTAW welding variable's procedure specifications as per ASME IX.

ASME IX Paragraph		**Process variable**
QW-402 Joints	.1	Groove design
	.11	Retainers
QW-403 Base metals	.8	Base metal thickness
QW-405 positions	.2	Position
QW-408 gas	.1	Trailing gas
	.2	Single, mixture, or %
	.3	Flow rate
	.9	Backing gas
	.10	Shielding gas
QW-409 Electrical characteristics	.1	Heat input
	.4	Polarity
	.8	Current and voltage
	.12	Tungsten electrode
QW-410 Technique	.9	Multi to single pass/side
	.25	Manual or automatic

In GTAW the arc efficiency decreases with increasing welding current, increasing welding electrode distance and increasing the positive polarity of the electrode. On the other hand, an increase in the arc efficiency can be achieved by increasing the gas flow or changing the gas mixture by adding more helium to the argon shielding gas.

3.1.3 Heat Input

The heat input is the measure of energy transferred per unit length of a weld from either an electrode or beam to the base metal during welding. Heat input is important mainly because of its influence on the heating and cooling rate of the weld. Consequently, this thermal cycle affects the weld size, influences the final metallurgical structure and mechanical behavior. Heat input is calculated as a ratio of power to the welding speed using equation 3 (Weman, 2003).

$$Q = \frac{V \times I}{\nu} \times \eta \qquad [3]$$

where Q is the linear heat input (J/m), V is the voltage (V), I is the current (A), ν is the welding speed (m/s) and η is the arc efficiency or laser energy transfer efficiency (Funderburk, 1999). The weld size (cross-sectional area) is proportional to the heat

input. The effect of heat input on the cooling rate is influenced by other factors such as material thickness, specific heat, density and thermal conductivity.

Arc efficiency is the proportion of the arc input energy that is transferred to the workpiece. The arc energy generated is a product of the current and voltage of the arc. Arc efficiency (η) can be expressed in an equation as

$$\eta = \frac{q_w}{q_{arc}} \qquad [4]$$

where, q_w: energy input transferred into the workpiece,

q_{arc}: energy input to the arc or laser beam

The energy not transferred to the workpiece is lost into the atmosphere through electrode heating, radiation, convection and heat conduction in the torch (Stenbacka, 2012). The energy distribution from the arc is demonstrated schematically in Figure 13.

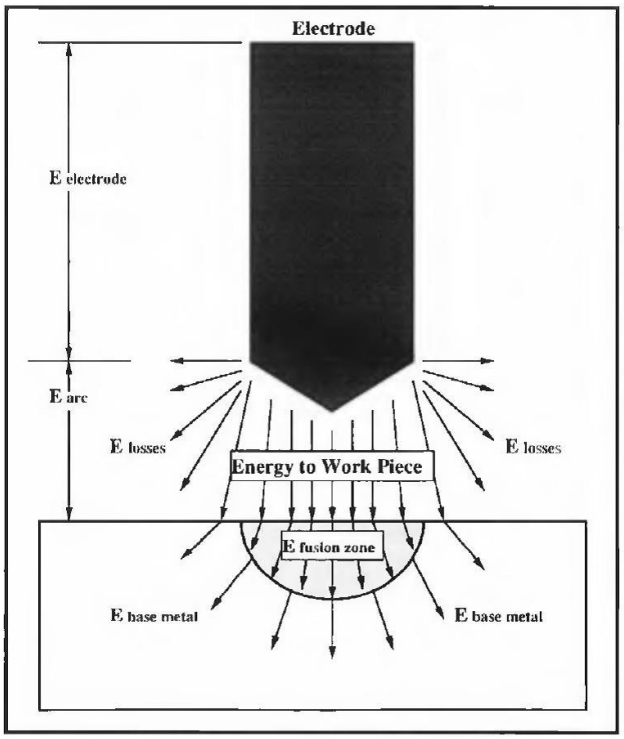

Figure 13: Schematic diagram showing energy distribution in arc welding (DuPont, 1995)

The arc efficiency can be influenced by welding parameters such as current, welding speed, electrode, and shielding gas.

3.2 The Rosenthal equation

Varying welding processes, parameters, and material, changes the heat input and consequently the weld thermal cycles. To be able to quantify the influence of heat input on the weld thermal cycle, the Rosenthal heat flow equation of a moving point heat source can be used.

In solving this heat flow equation, Rosenthal made a number of assumptions which some are listed below:

1. The plate is semi-infinite.

2. The welding heat source was a moving point.

3. Material physical coefficients are not affected by changes in temperature or state (solid or liquid)

4. Heat losses at the plate surface to the atmosphere are negligible.

5. Latent heat changes due to phase transformations are ignored

In applying the Rosenthal equation, the influence of the welded plate thickness needs to be considered because of its influence in characterizing the heat flow as either two or three dimensional. Since the thermal cycle is a function of the plate thickness, it is necessary to determine the critical thickness (d') or the transition thickness between thick and thin plate. This critical thickness can be calculated according to

$$d' = \{\frac{q}{2\rho c v}\left(\frac{1}{773-T_0}+\frac{1}{1073-T_0}\right)\}^{1/2} \qquad [5]$$

The 1073K to 773K used in this equation is the transformation temperature range of austenite with its products for carbon steel. For the purpose of this investigation, the temperature range will be taken as 1173K to 773K (900-500°C) because this represents the two-phase region in the zirconium-2.5niobium phase diagram where the beta ($\beta_{Zr,Nb}$) phase transforms to alpha zirconium + beta (β_{Nb}) niobium.

Once the critical diameter has been determined, the correct Rosenthal equation between [6] and [7] can be applied to calculate the cooling rate or the temperature-time distribution.

Thick plate: $$T - T_0 = \frac{\frac{q}{v}}{2\pi\lambda t} e^{-\frac{r^2}{4at}} \qquad [6]$$

Thin plate: $$T - T_0 = \frac{\frac{q}{v}}{d\sqrt{4\pi\lambda\rho ct}} e^{-\frac{r^2}{4at}} \qquad [7]$$

where: T temperature at a distance r from the heat source (K)
T_0 temperature of the plate prior to welding (K)

d	plate thickness (m)
q	welding power (W)
v	welding speed (m/s)
q/v	heat input (J/m),
λ	thermal conductivity ($Wm^{-1}K^{-1}$ or $Jm^{-1}s^{-1}K^{-1}$)
a	thermal diffusivity (m^2s^{-1})
ρc	volume thermal capacity ($Jm^{-3}K^{-1}$),
t	time (s)
r	distance from the heat source (m)

Determining the peak temperature and the cooling rate in the heat affected zone will assist in understanding the weld's microstructure and relating these factors to dilatometry microstructures.

3.2.1 Relationship between the weld size and heat input

As already mentioned, the heat input is an important parameter in controlling the resulting weld pool size and its cooling rate. A low heat input will result in a smaller weld pool and higher cooling rates because less energy needs to be dissipated. This has a bearing on the weld and HAZ size and its microstructural morphology and constituents. For a welded sample, the measured weld size can, therefore, be used to estimate the heat input required to achieve it. This can be done by using the simplified Rosenthal thin plate equation [8] below and making the heat input (q/v) the subject of the formula.

$$T_p - T_0 = \sqrt{\left(\frac{2}{\pi e}\right)} \frac{q/v}{d\rho c 2r} \qquad [8]$$

where:

T_p	temperature at a distance r from the weld center (2113K)
T_0	temperature of the plate prior to welding (298K)
q/v	heat input (to be calculated)
d	plate thickness (m)
r	distance of the fusion line from the weld centre (half the weld bead width).
ρc	volume thermal capacity ($Jm^{-3}K^{-1}$)

3.2.2 Determining arc efficiency from weld widths

The heat input used in the Rosenthal equation to determine the thermal cycle is a function of the welding parameters (power) and the arc efficiency. Due to inherent variable inconsistencies in the welding process, accurate arc efficiency cannot be simply taken from the literature. Calculating the arc efficiency is therefore critical not

only for determining the thermal profile of a weld but also in characterizing the welding process.

Calculating the arc efficiency is a two-step process:

1: Determining the heat input from the welding process parameter (excluding arc efficiency from the literature)

HI (q/v) = welding power/welding speed

2: Calculating the heat input required to achieve the measured weld metal widths. The value of heat input can be achieved by using the simplified Rosenthal thin plate equation [8] as already mentioned in the sub-section 3.2.1.

The arc efficiency of both welding processes can, therefore, be determined by comparing the two weld heat inputs.

3.3 Dilatometry

Dilatometry is a technique used to study solid-solid phase transformations in materials. It allows observation of dimensional changes occurring in the sample by application of a thermal cycle (Garci, 2002). Phase transformation temperatures can thus be determined using this technique because when a material undergoes a phase change, the lattice structure changes and this is accompanied by a change in specific volume (Garci, 2002).

As the phase transformation temperatures and mechanisms of zirconium-2.5niobium were covered in chapter 2, only the dilatometry analysis will be explained in this section. Fong (2012) and his co-workers analyzed the crystallographic texture and volume fraction of α and β phases in zirconium-2.5niobium pressure tube materials during heating and cooling, and the results displaying volumetric thermal changes are presented in Figure 14.

The volumetric thermal expansion of the hcp α-phase increased linearly on heating to about 750°C as observed in Figure 14. Heating to temperatures above 750°C gave a larger linear expansion up to 900°C. This increase of linear expansion at higher temperatures can be attributed to segregation of oxygen in the primary α_{Zr} grains, occupying the interstitial sites within the hcp structure, which is known to increase the lattice parameters according to Choubey (1996). In the bcc β-phase, little change in unit cell volume with temperature is observed on heating below 620°C (monotectoid temperature). This little change is due to the transformation of the metastable β_{Zr} phase into a β_{Nb} that reduces the lattice parameter in combination with the linear thermal expansion of the lattice (Aldridge, 1972). Heating through the temperatures from about 600 to 900°C, there is a sharp increase in linear volumetric expansion of the β-phase structure. The sharp volumetric expansion can be related to

the combined changes in the niobium content in the transformed β_{Zr} phase and the dependence of the lattice parameter on temperature. On heating at temperatures above 900°C into the full β-phase region, there is a decline in the linear volumetric expansion of the β phase structure, which is simply due to the linear temperature dependence of the lattice parameter (Fong, 2012).

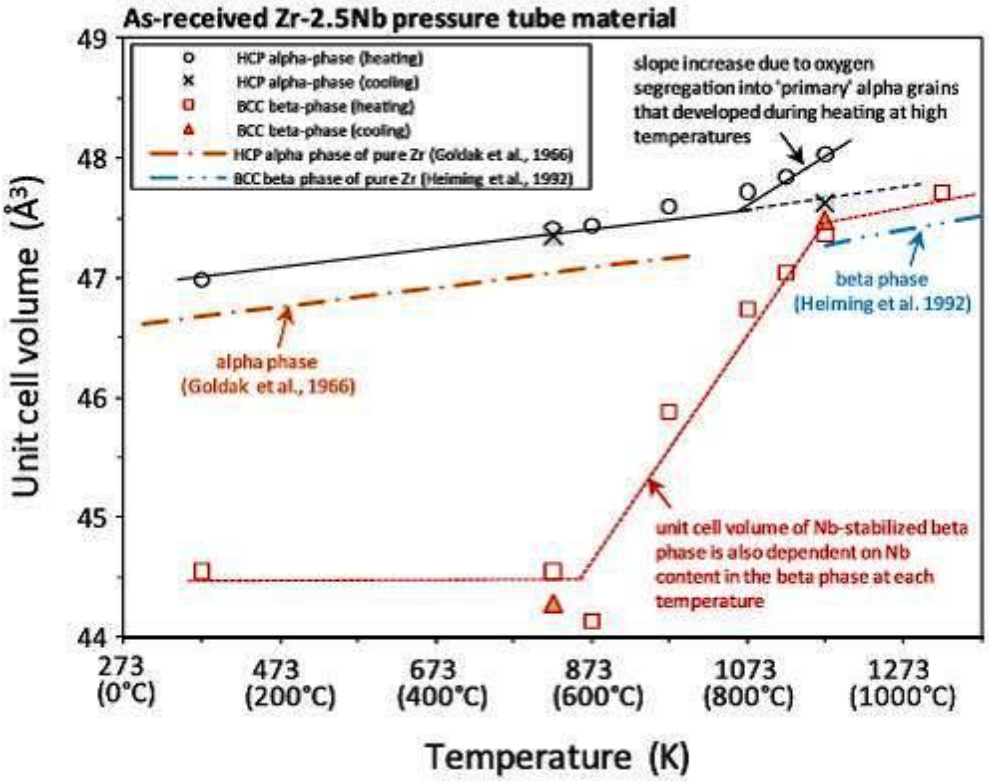

Figure 14: Volumetric thermal change of Zr-2.5Nb during heating and cooling (Fong, 2012)

The coefficient of thermal expansion in the α-phase temperature range depends strongly on the initial crystallographic texture due to the anisotropy of the hexagonal crystallographic structure in the zirconium-2.5niobium alloy. Therefore, the initial metallurgical condition has a strong influence on dilatometry results. This dependency of thermal expansion on crystallographic texture is the reason why discrepancies can be observed on results of different samples. Alloying and impurity elements present in the zirconium-2.5niobium can also contribute to discrepancies (Forgeron, 2000).

The contraction observed on heating through the transformation range just above the (620°C) transus temperature is due to a decrease in unit cell volume of bcc β as compared to the hcp α. The interatomic distance in β zirconium is about 2.6 percent smaller. When the amount of transformed β phase increases sharply above the transus temperature, the total volumetric change becomes significant.

CHAPTER 4

Experimental Procedure

This chapter describes the experimental plan followed during the course of this investigation. A 1.5 mm thick zirconium-2.5niobium metal sheet was laser beam and gas tungsten arc welded with varying parameters. All welds performed were autogenous bead-on-plate. Figure 15 are images of the welded samples. The parameter matrix was designed to ensure full penetration on all welds and overlapping heat inputs of the two welding processes. No pre-heat or post-weld heat treatment was performed during this investigation. The as-received plate and welded samples were then characterized to determine the microstructure and mechanical properties. Dilatometry was also performed to simulate the response of the material during welding and determining the resulting microstructure with varying cooling rates.

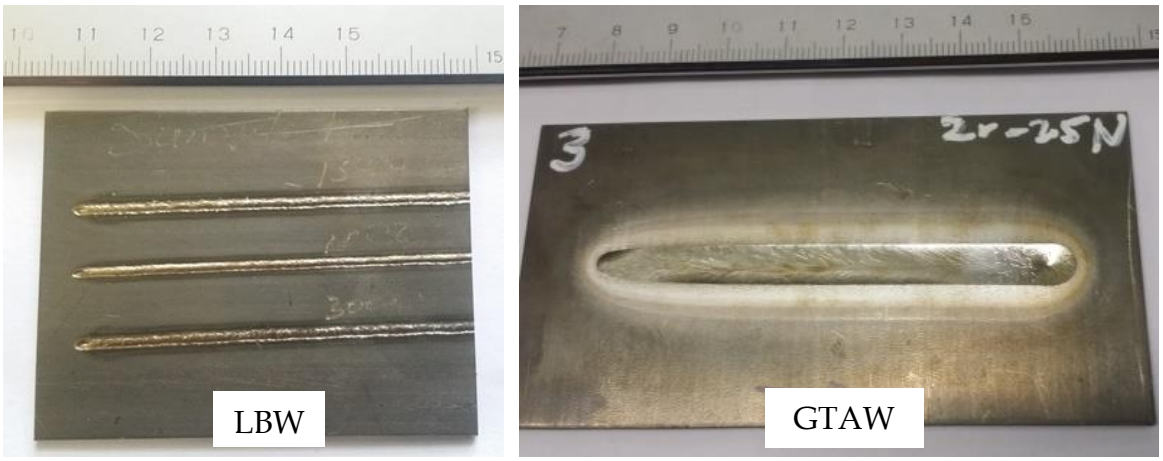

Figure 15: Typical bead on plate welds on the Zr-2.5Nb alloy samples

4.1 Analysed base material Zr705 alloy (zirconium-2.5niobium)

The material used for investigation was Zr705 alloy sheet of 1.5 mm thickness supplied by ATI Specialty Alloys & Components. The chemical composition of the alloy as provided by the supplier is shown in Table 5 and conforms to the ASTM B352 standard. The material was supplied in the cold worked and annealed condition. The sheet was sectioned into 100 x 50 mm rectangular samples using a foot operated guillotine. Prior to welding, all the sectioned samples were cleaned with ethanol to limit contaminants.

Table 5: Chemical composition of Zr-2.5Nb alloy base metal (wt% unless noted otherwise)

Elements	ASTM B352 Standard (max)	Base metal (Zr705)
Zirconium + hafnium (min)	95.5	97.1
Niobium	2-3	2.58
Hafnium	4.5	0.027
Iron+ Chromium	0.2	0.11
Oxygen	0.18	0.136
Nitrogen	0.025	0.0066
Hydrogen	0.005	0.0013
Carbon	0.05	0.0113

4.2 Welding

4.2.1 Laser Beam Welding (LBW)

LBW was performed in the key-hole (deep penetration) mode using an IPG YLR 3000 - ST fiber laser which has a maximum power output of 3 kW. The welding head was mounted on an articulated arm robot. The samples were assembled on a welding table with a root purge incorporated as seen in Figure 16. Helium was used for root purging and shielding whilst a trailing weld shoe using argon was utilized for the top side of the weld bead. Table 6 shows all the essential welding variables used during the LBW process as stipulated in ASME IX.

A total of 9 laser welds (labelled L1-L9) were performed. The welding parameters are presented in Table 7 showing the different combinations of welding speed and laser power used. The heat input was calculated using the Rosenthal equation for thin plate from the weld's cross-sectional area. Visually most welds were free of discoloration which suggests adequate shielding except for two high heat input welds (L6 and L9) which contained the dark straw to light blue colours. These colors indicate surface oxidation which can be removed using a wire brush as per the AWS G2.5/G2.5M zirconium welding standard.

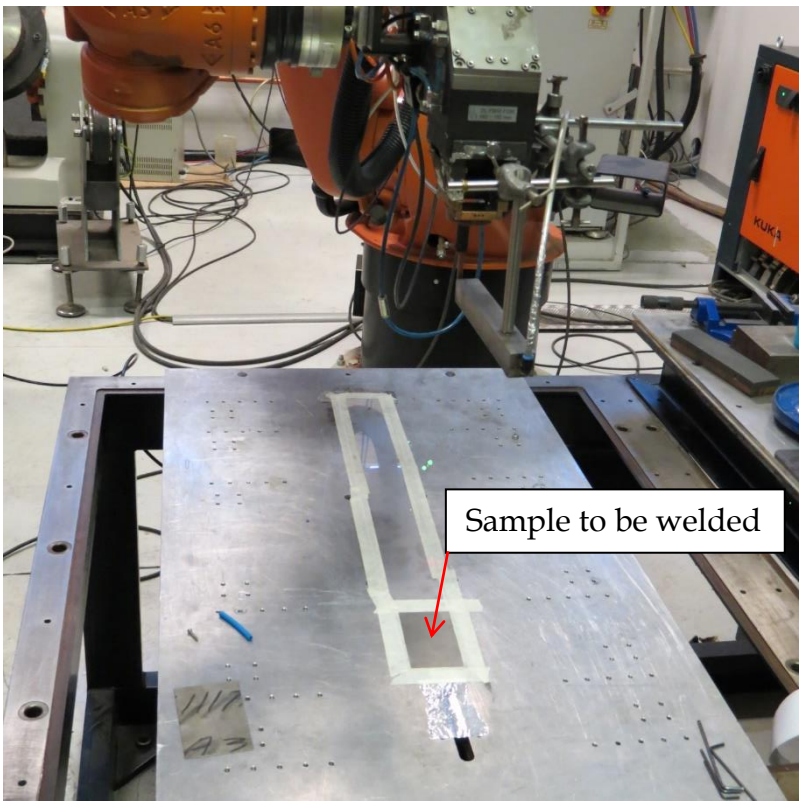

Figure 16: LBW set-up during welding. IPG YLR 3000 - ST fiber laser which has a maximum power output of 3 kW

Table 6: Essential welding variables used to produce all the laser welds

ASME IX Paragraph		Process variable	Parameters
QW-402 Joints	.1	Groove design	Bead on plate
QW-403 Base metals	.3	Penetration	Full weld penetration
QW-408 gas	.2	Single, mixture, or %	Helium and argon
	.12	Flow rate	17 lpm
QW-409 Electrical characteristics	.20	Mode, energy	Continuous mode
	.21	Power, speed	Max 3kW, 1-4m/min (see Table 7)
QW-410 Technique	.17	Type/model of equipment	IPG YLR 3000 - ST fibre laser
	.37	Single to multiple pass	Single-pass
	.77	Wavelength	1.07 µm
	.80	Spot size	250 µm

(lpm: liters per minute)

The heat inputs in Table 7 (LBW) and Table 9 (GTAW) were calculated using the weld's cross-sectional areas as stipulated in Section 3.2.1 in the previous chapter.

Table 7: Laser beam welding parameters (spot size: 250µm)

Sample Label	Power (W)	Welding Speed (m/s) x10^{-3}	Heat Input (J/mm)
L1	1000	66.7	8.30
L2	1500		14.5
L3	3000		13.4
L4	1000	33.3	18.6
L5	1500		22.7
L6	3000		21.7
L7	600	16.7	17.6
L8	800		26.3
L9	1000		28.9
Range			8.30 to 28.9

4.2.2 Gas Tungsten Arc Welding (GTAW)

The GTAW process was used to weld a total of eight samples. The direct current electrode negative (DCEN) polarity was used with an EWTh 2.4 mm diameter electrode on the semi-automated GTAW machine. Technical-grade argon was used for purging and shielding through the backing plate, torch nozzle and trailing weld shoe, see Figure 17 for welding apparatus set-up. Table 8 contains the welding process variable used. The welding arc was initiated through the 'lift-arc' method where the workpiece is lifted to touch the electrode and on lowering, the arc strikes. The 'lift-arc' method is not commonly used when welding zirconium alloys due to the difficulty of lifting complex and heavy products. The welding set-up which afforded good shielding, made it possible to apply this method.

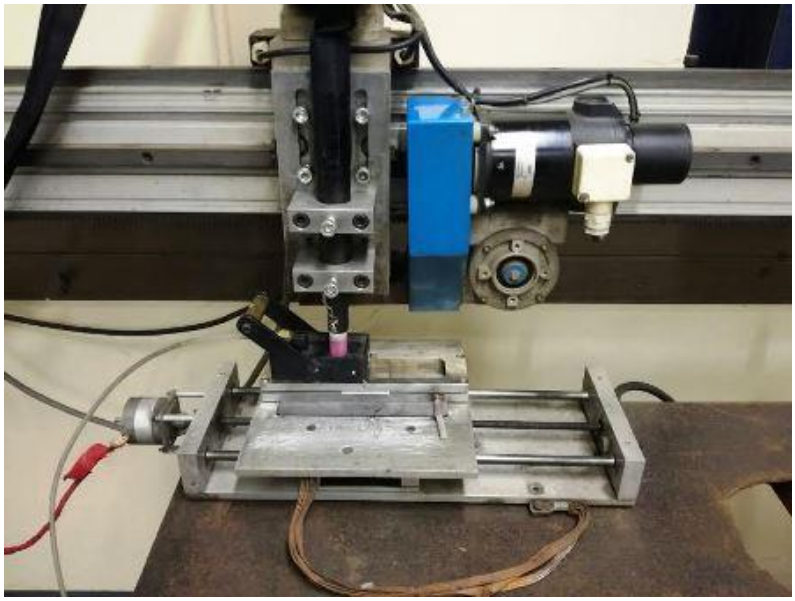

Figure 17: Semi-automated GTAW set-up.
Argon gas was supplied through the black trailing shoe on top and the backing plate.

Table 8: Essential welding variables used to produce all the GTAW welds

ASME IX Paragraph		Process variable	Parameters
QW-402 Joints	.1	Groove design	Bead on plate
	.11	Retainers	Backing gas housing
QW-403 Base metals	.8	Base metal thickness	1.5 mm
QW-405 positions	.2	Position	Flat
QW-408 gas	.1	Trailing gas	Argon
	.2	Single, mixture, or %	Single
	.3	Flow rate	15 lpm
	.9	Backing gas	Argon
	.10	Shielding gas	Argon
QW-409 Electrical characteristics	.1	Heat input	As seen in Table 9
	.4	Polarity	DCEN
	.8	Current and voltage	As seen in Table 9
	.12	Tungsten electrode	EWTh 2.4 mm diameter
QW-410 Technique	.9	Multi to single pass/side	Single
	.25	Manual or automatic	Semi-automated

Different combinations of welding speed and current were applied resulting in a heat input range of 21.7 to 74.3 J/mm between the eight welds. Table 9 shows the actual welding parameters. The welding current and voltage presented in Table 9 are calculated averages from data recorded during welding. No discoloration was observed visually on the welds which suggested adequate shielding.

Table 9: Gas tungsten arc welding parameters

Sample	Welding Current (A)	Welding Voltage (I)	welding speed (m/s) $x10^{-3}$	Heat input (J/mm)
T1	54.7	9.42	3.43	43.4
T2	69.7	10.43		50.6
T3	79.6	11.0		64.0
T4	70.0	10.5	5.02	21.7
T5	90.0	11.1		45.4
T6	104.6	11.45		74.3
T7	99.7	11.1	7.54	33.0
T8	119.6	12.5		54.7
Range				21.7 to 74.3

4.3 Dilatometry

Dilatometry was performed during this investigation to achieve the following objectives

- To examine the resulting microstructure with varying cooling rates applied.
- To determine the phase transformation temperatures during cooling including the monotectoid and martensite start temperatures.
- To determine the hardness values of the different microstructures.

Due to the inherent nature of fusion welding, the workpiece has to form a molten metal. The limitation of the dilatometric technique is that one cannot start with a molten metal, especially in studying the phase transformations of materials which have phases forming at temperatures very close to the melting point. This limitation is however not a problem in zirconium-niobium alloys because of the large single beta ($\beta_{Zr,Nb}$) solid solution region after solidification. During welding, every point in the heat affected zone experiences a different thermal cycle depending on its distance from the arc. This means a weld will have different microstructures and mechanical properties from one point to the other. Therefore studying the continuous cooling transformation behavior of the zirconium-2.5niobium alloy using varying thermal cycles in the dilatometer, is crucial in understanding its response to welding.

Initially, dilatometry was done on folded 1.5 mm thick samples to improve the buckling strength. On performing the test at elevated temperatures when the structure has transformed to the single beta phase region (above 870°C), the thermal curve showed a significant contraction of the sample even though the temperature was rising. This is demonstrated in Figure 18 where the folded sample's thermal curve showed an increasing negative change in length, indicating contraction.

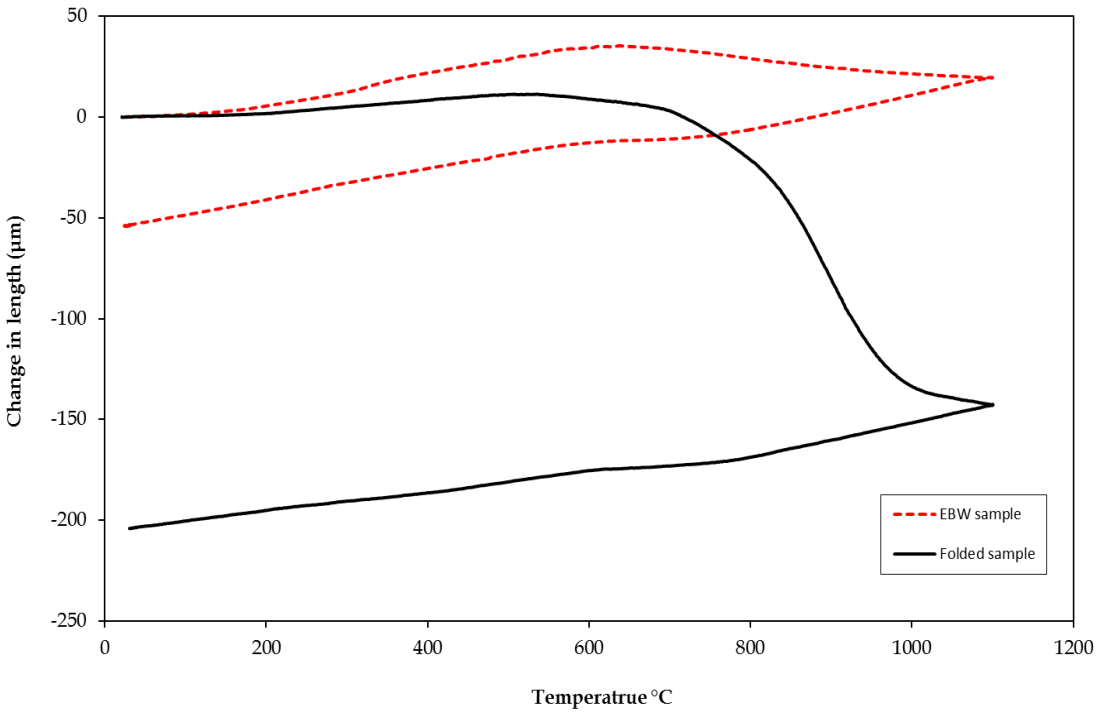

Figure 18: Dissimilarity in thermal curve contraction due to the dimensional difference of the two dilatometry sample. Heating of 1°C/s to 1100°C

The difference in contraction magnitude led to the conclusion that at high temperatures the sample was too soft, therefore, deforming due to the pressure applied by the dilatometry anvils. To increase the high-temperature strength of dilatometry samples, multiple layers of the zirconium-2.5niobium alloy sheet were autogenously welded together using the electron beam welding (EBW) process to increase the thickness, with final sample dimensions of 4 x 5 x 10 mm. Both the folded and EBW dilatometry samples are shown in Figure 19.

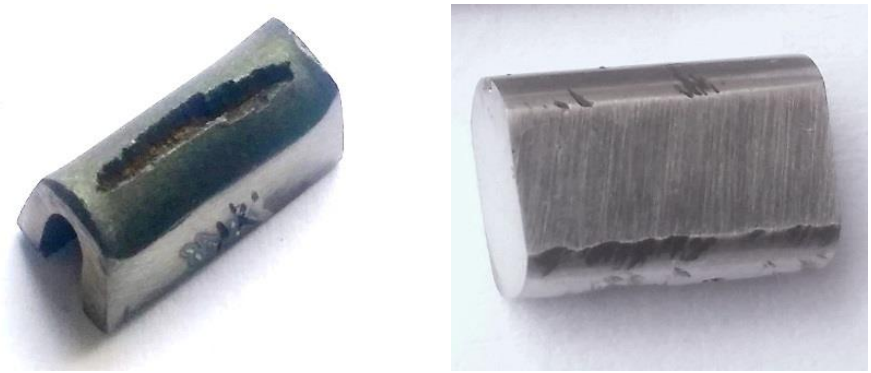

Figure 19: An initial folded dilatometry sample on the left and the improved electron beam welded dilatometry sample on the right. Both samples are of a 10 mm length.

EBW was the preferred process because it is performed in a vacuum chamber, therefore, eliminating the risk of contamination. Dilatometry tests done on these

samples gave satisfactory results. The much-improved dilatometry results from EBW samples are clearly shown above in Figure 18 and Figure 19. All the dilatometry tests were then performed using the EBW samples.

The EBW samples were heated up into the beta ($\beta_{Zr,Nb}$) phase region before cooling to effectively counter the effects of melting during electron beam welding process. A Bähr dilatometer was used to analyze 8 samples. An S-type (Pt/Pt-10%Rh) thermocouple was spot welded on to the samples for temperature monitoring. The samples were heated at a constant rate of 10°C/s to a peak temperature of 1050°C and held for 10 minutes before cooling at different rates from 0.5 - 600°C/s. A complete list of all the cooling rates is given in Table 10. A single phase beta region exists at 1050°C for the zirconium-2.5niobium alloy. Hunt and Niessen (1970) reported that stable conditions are achieved with a short time of just over 60 seconds in the beta phase region. They concluded that neither time at temperature nor the large grain size obtained by a long high temperature anneal have much effect on the subsequent transformation behavior. Therefore 10 minutes at peak temperature was considered sufficient to produce reliable transformation results. Helium gas was introduced into the chamber for better control of the cooling rate during quenching.

The data obtained was used to plot the continuous cooling. Dilatometry samples were examined for metallography and hardness.

Table 10: Dilatometry cooling thermal cycles (Heating rate of 10°C/s to 1050°C and soaked for 10 minutes before cooling)

Sample	Cooling rate (°C/s)
1	0.5
2	1
3	10
4	20
5	50
6	150
7	300
8	600

4.4 Metallography

Sample preparation of zirconium alloy for metallography examination must be carefully controlled because of the ease with which smearing occurs and the risk of forming mechanical twins during cutting and grinding (Vander Voort, 1984). Grinding was done manually using silicon-carbide grinding paper from 180 to 1200 grit size after mounting with Bakelite resin. Removal of fine scratches through mechanical polishing proved very difficult. Chemical polishing was therefore applied during this investigation because of the challenges in using the standard

methods. Chemical polishing is a controlled corrosion process where a thin layer of material is removed in a sample, simultaneously achieving a polished and etched surface (Vander Voort, 1984). This was done by swabbing the sample surface with cotton wool immersed in 10HF–45HNO_3–45H_2O_2 (volume percentage) solution (Vander Voort, 1984). Two sections of the welded samples were examined, the longitudinal planar (top side of the weld) and the transverse planar (cross-section of the weld).

The microstructure was characterized using the following equipment

- Stereoscope, Olympus SZX7
- Optical microscope, Olympus BX51M
- Scanning electron microscope, Zeiss Ultru PLUS FEG SEM, and Jeol JSM IT300LV.

4.5 Mechanical Properties

4.5.1 Hardness Testing

Due to the fact that the zirconium-2.5niobium alloy is a hardenable material, hardness properties provide valuable knowledge in better understanding the welding transformation products. Hardness testing was performed using a Future-Tech FM700 micro-Vickers hardness tester with a load of 500 g/f and dwell time of 10 seconds. The welded samples were tested across the longitudinal planar (top welded side) covering the base metal, heat affected zone and the weld, Figure 20. The hardness indents were 0.5 mm apart. Ten hardness measurements were done randomly on the dilatometry and the base metal samples.

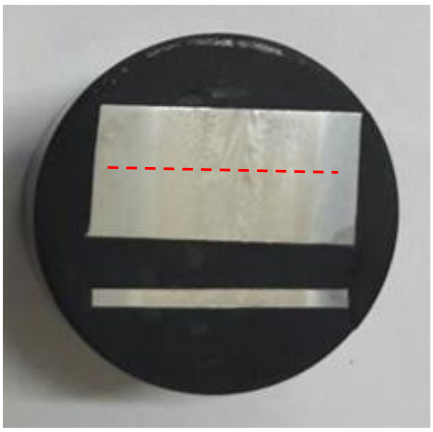

Figure 20: A mounted sample with red dotted line demonstrating where hardness was performed.

4.5.2 Tensile Testing

To evaluate and compare the weld's mechanical properties of the two welding processes, sub-size tensile samples were prepared according to the ASTM E8/E8M

standard, Figure 21. The longitudinal length of the welds was tested. Conventionally, the tensile properties of a welded joint are characterized using a tensile test coupon that is machined transverse to the weld (AWS B4). It will be shown in the results section that the hardness of the weld metal and of the heat affected zone was higher than the hardness of the base metal. A transverse tensile test coupon would, therefore, have failed in the unaffected base metal, and the tensile behavior of the weld metal would not have been characterized. Also, the welded components in nuclear applications experience circumferential stresses, therefore the longitudinal tensile test of the weld is more appropriate. Given the coupon width of 6 mm and the width of the weld bead in the order of 2-4 mm, the tensile test results, therefore, reflect the combined mechanical behavior of the weld metal and the heat affected zone.

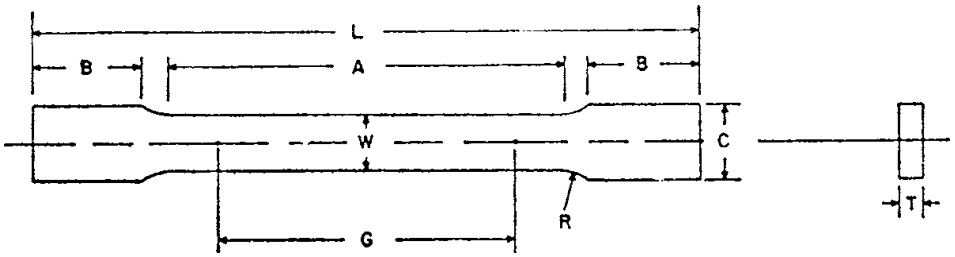

Figure 21: Standard sub-size tensile sample dimensions (mm) according to ASTM E8/E8M standard

Where:

Gage length (G)	:	25
Width (W)	:	6
Radius of fillet (R)	:	6 (min)
Overall length (L)	:	100
Length of grip section (B)	:	30
Width of grip section (C)	:	10

The samples were tested with a MTS Criterion 40 tensile test machine at a constant crosshead speed of 2 mm/minute. This translates to a strain rate of 0.08 mm/mm-min, conforming to the ASTM B811-02 zirconium standard which specifies a strain rate range of 0.076 to 0.18 mm/mm-min. All tests were carried out at room temperature. Five samples were tested in total, including two samples of LBW welds, two of GTAW welds and one of the as-received sheet. The fracture surfaces of the broken tensile samples were analyzed with SEM.

CHAPTER 5

Results

This chapter presents the results and analyses obtained from experiments conducted as described in chapter 4.

5.1 Dilatometry

5.1.1 Determining the phase transformation temperature during heating

To determine the monotectoid and $(\alpha+\beta)$ / $\beta_{(Zr, Nb)}$ transformation temperature, EBW samples were tested at 0.5, 1 and 10°C/s heating rates to 1100°C. The resulting curves are shown in Figure 22.

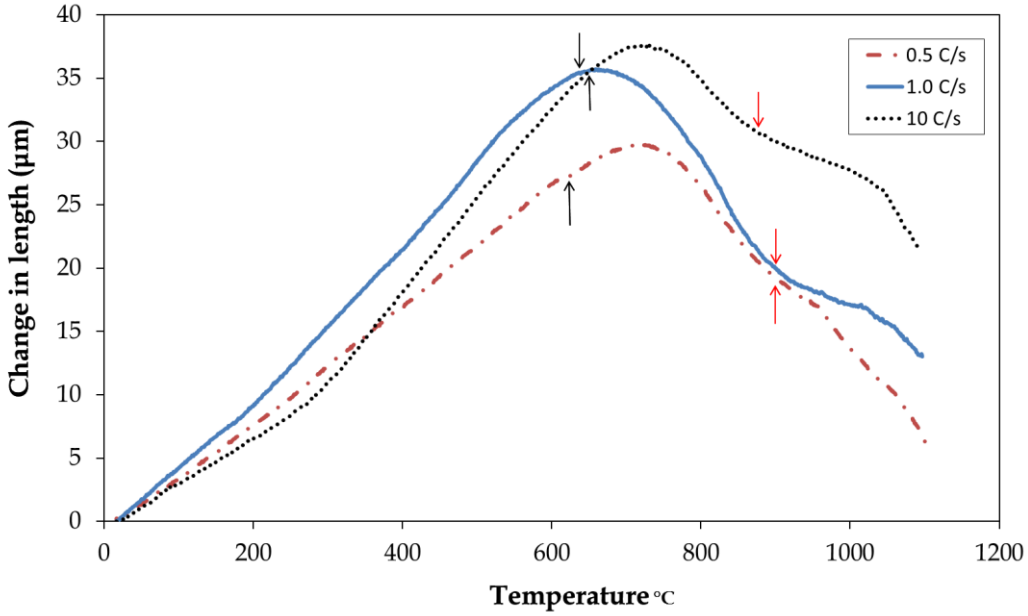

Figure 22: Thermal curves plotted to determine the transformation temperature at varying heating rates applied to 1100°C. The black and red arrows indicate the monotectoid and $(\alpha+\beta_{Zr})$ / $\beta_{(Zr, Nb)}$ transformation temperatures respectively.

The following transformation temperatures were determined and are listed in Table 11.

Table 11: Determined transformation temperatures (°C)

Heating rate (°C/s)	Monotectoid Temp	$(\alpha+\beta_{Zr})$ / $\beta_{(Zr,Nb)}$
0.5	611	880
1	636	881
10	640	868

5.1.2 Determining phase transformation temperatures during cooling

Eight samples were heated at a constant rate of 10°C/s to a peak temperature of 1050°C and held for 10 minutes before cooling at different rates from 0.5 - 600°C/s. The complete thermal cycles are shown in Figure 23.

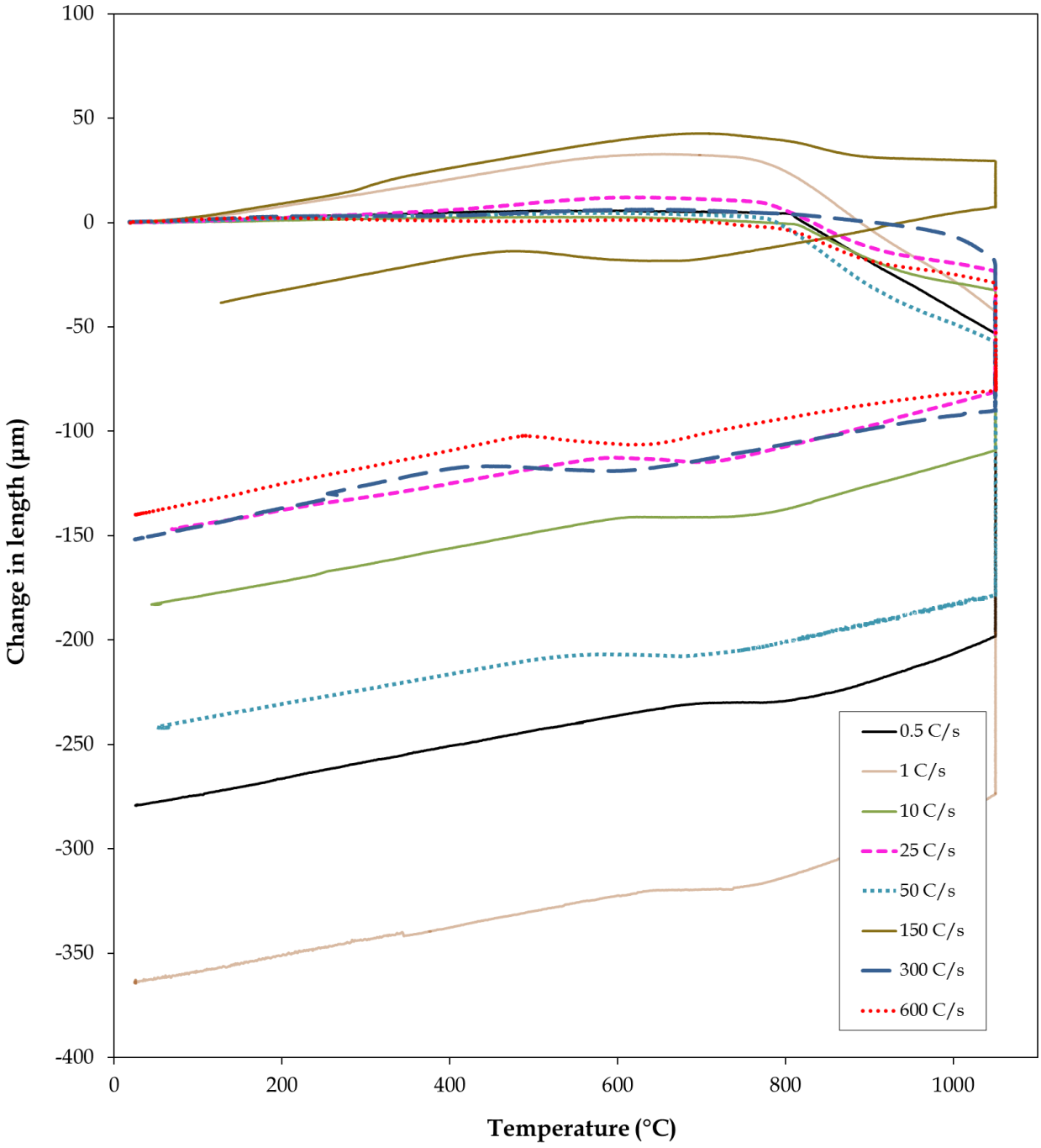

Figure 23: Thermal cycles with the varying cooling rates of 0.5 - 600°C/s.

The transformation temperatures were determined as stipulated by Atkins and is demonstrated in Figure 24 (Atkins, 1980). Continuous cooling transformation (CCT) curves were constructed from dilatometry thermal curves and are shown in Figure 25. The transformation start and finish temperatures indicated by the black solid lines were read from 1 and 99 percent of the inflection points. The transformation temperature and time at different percentages of transformation are highlighted by the dotted lines.

A table containing the actual measured values of transformation start and finish temperatures from the different cooling rates is included in Table 21 in the Appendix. At an 0.5°C/s cooling rate, the $\beta_{(Zr,Nb)}/(\beta_{Zr}+\alpha_{Zr})$ transformation start temperature was found to be 865°C. The observed β to α start temperature progressively decreased with faster cooling rates to ~756°C at 50°C/s. The transformation finish temperature $(\beta_{Zr}+\alpha_{Zr})/(\beta_{Nb}+\alpha_{Zr})$ was observed to be 512°C at a cooling rate of 50°C/s. The M_s and M_f temperatures were found to be 690 and 435°C respectively at a 150°C/s cooling rate. The transformation products were identified through microstructural examination using SEM and confirmed by hardness testing.

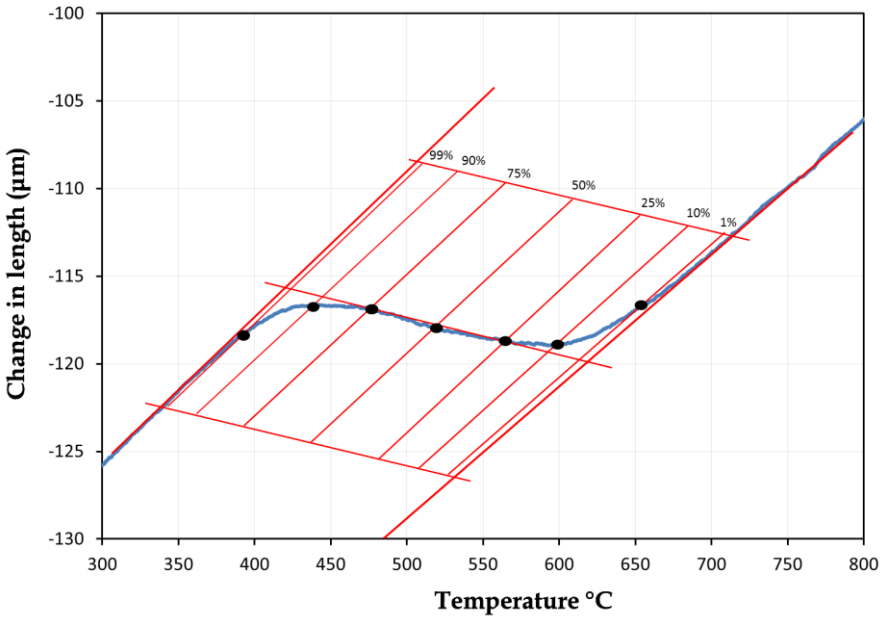

Figure 24: A section of the 300°C/s cooling curve used to demonstration how measurements of beta transformation temperature at different phase volume fractions were determined.

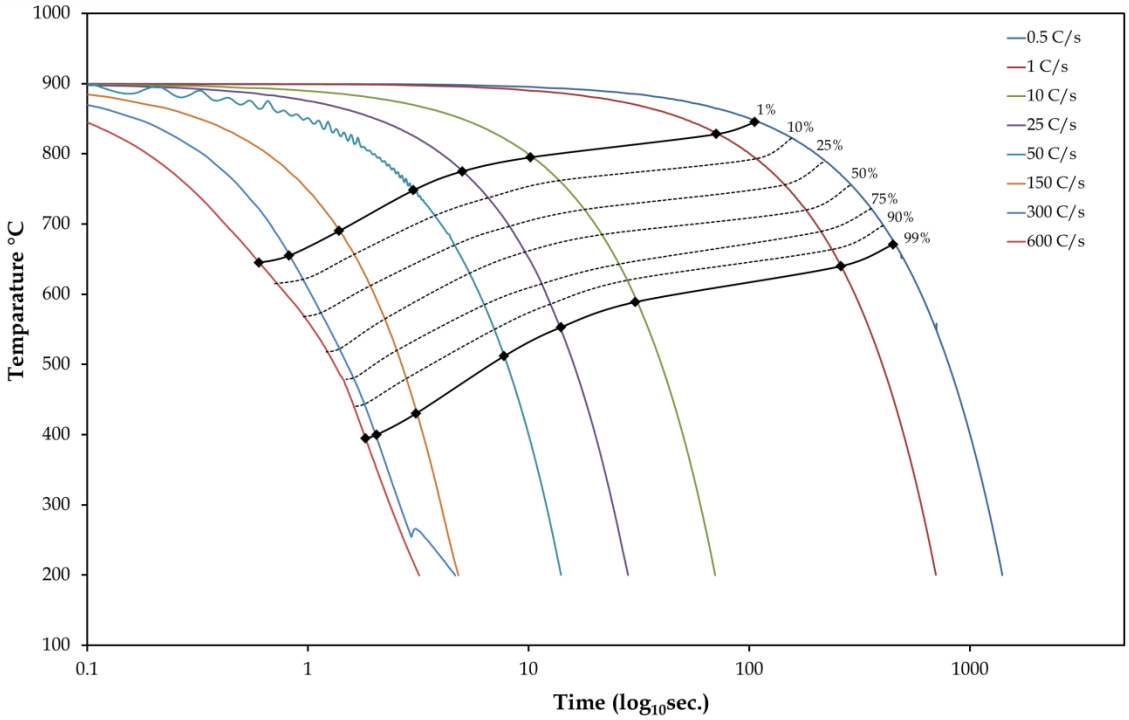

Figure 25: Partial CCT diagram from dilatometry sample's cooling curves. The solid and dotted lines intersecting the cooling curves highlight the transformation temperatures and times at varying volume fractions of the transformed product. The cooling rate was varied from 600 to 0.5°C/s.

5.1.3 Microstructures of dilatometry samples

Microstructural examination of the dilatometry samples was performed using two scanning electron microscopes (SEM) namely the Zeiss Ultra PLUS FEG SEM and Jeol JSM IT300LV. Representative images of the microstructure at slow, intermediate to very fast cooling rates are shown from Figure 26-29. The dilatometry samples cooled between the ranges of 0.5-50°C/s showed a Widmanstätten structure. At 0.5-1°C/s cooling rate the structure exhibited a course hcp alpha phase structure, Figure 26. It consisted of a large volume fraction of basket weave, parallel plate structure and grain boundary allotriomorphs (GBA). The alpha parallel plates maintained strict orientation relationships and habit planes with the parent beta phase.

At higher cooling rates (≥ 150°C/s) a fully martensitic structure was observed, Figure 29. The morphology exhibited acicular (α′) martensite plates with the structure also becoming finer with increasing cooling rate. The parent beta phase is first partitioned by primary acicular plates which span across the grain. Secondary plates then form within the untransformed β phase and the process continues till the transformation is complete. The acicular plates form along different variants of the habit plane, giving the structure the zig-zag appearance.

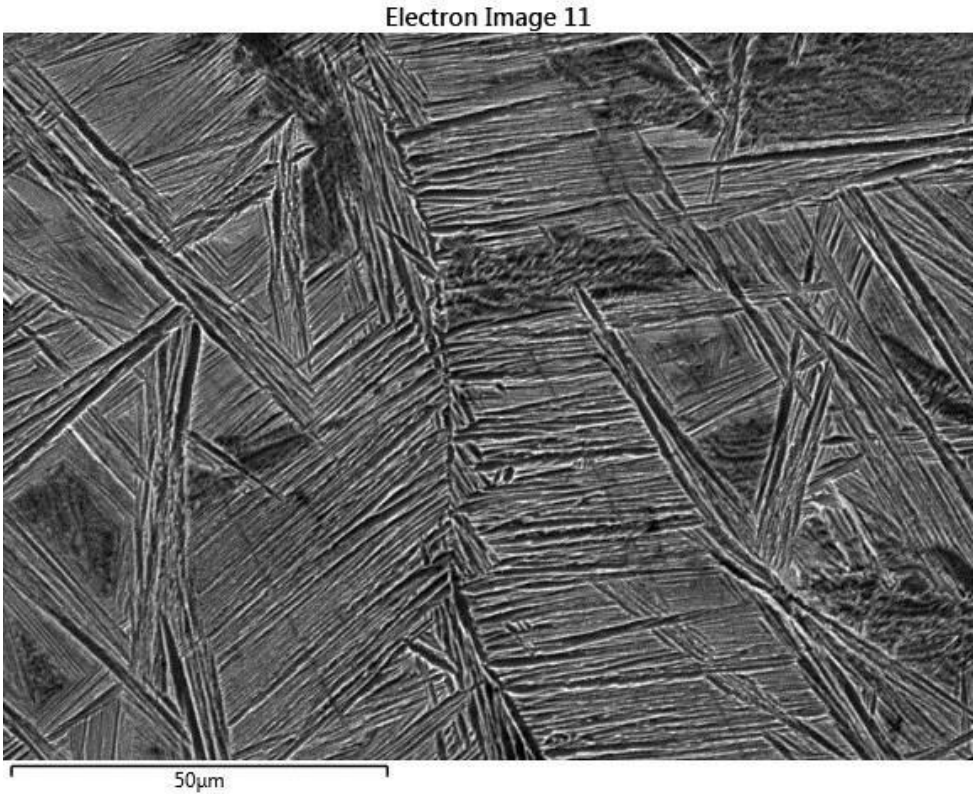

Figure 26: SEM (Jeol JSM) images of 1°C/s dilatometry sample showing the Widmanstätten microstructure. 1000X magnification.

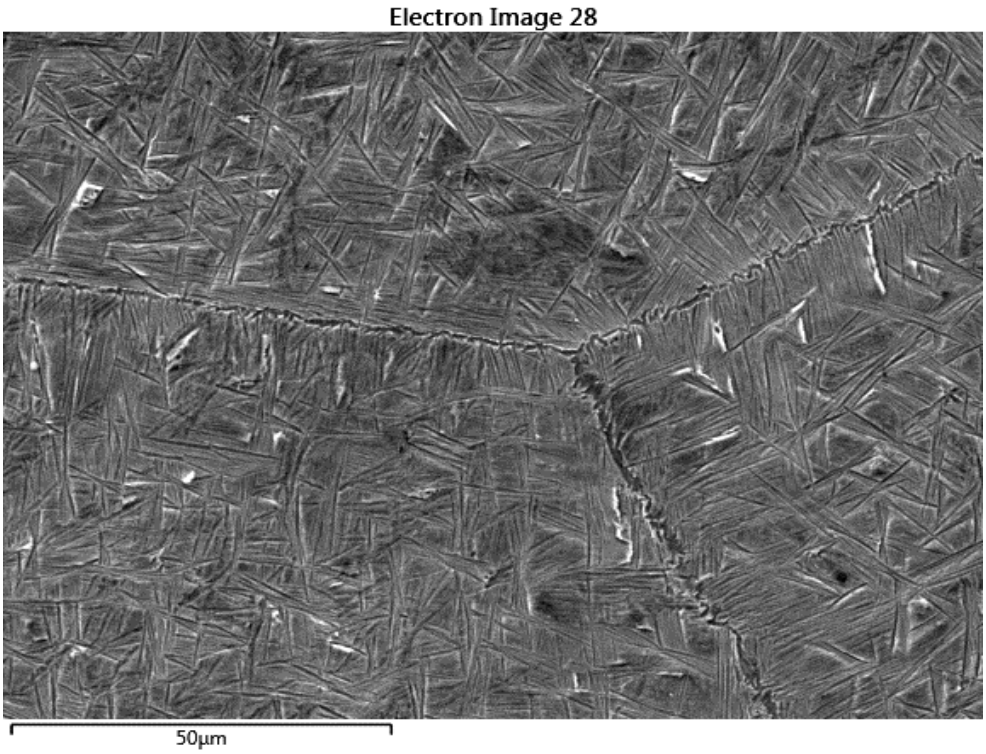

Figure 27: SEM (Jeol JSM) images of 10°C/s dilatometry sample showing the Widmanstätten microstructure with a large volume fraction of basket-weave phase . 1000X magnification

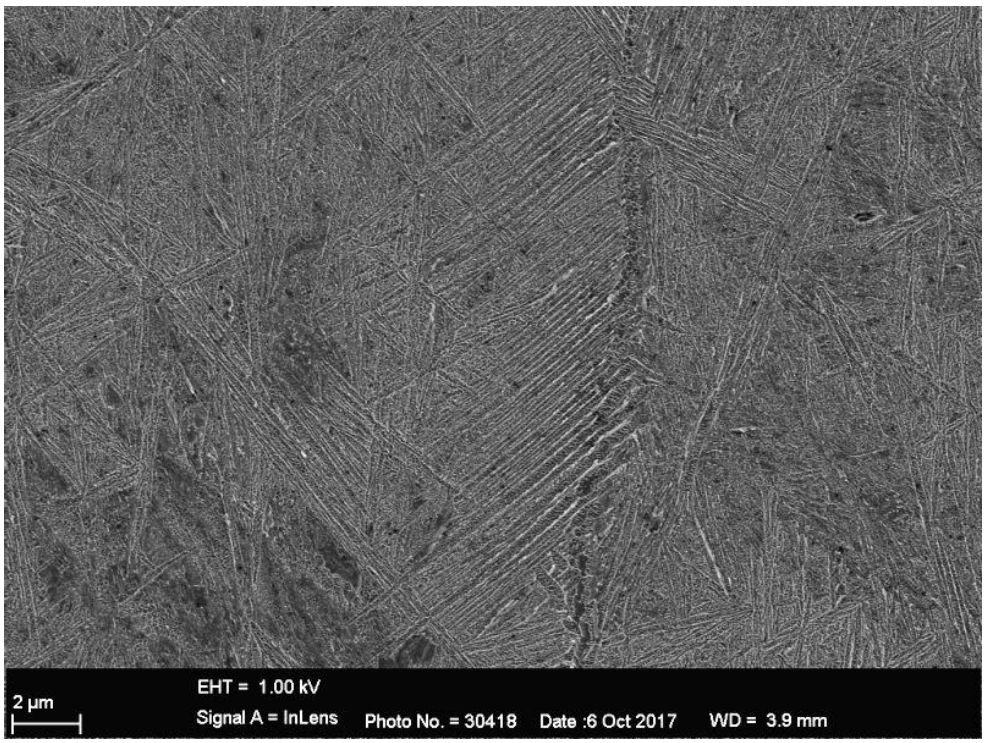

Figure 28: SEM (Zeiss Ultra PLUS FEG) images of 50°C/s dilatometry sample showing the very fine Widmanstätten microstructure. 10000X magnification

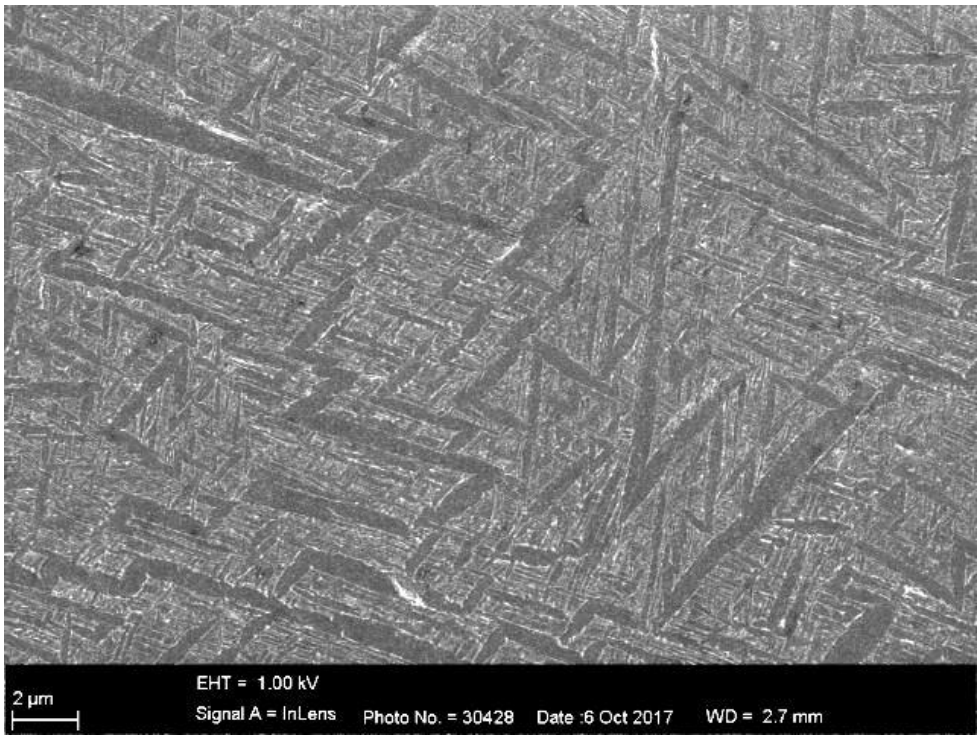

Figure 29: SEM (Zeiss Ultra PLUS FEG) images of 600°C/s dilatometry sample showing the acicular martensite. 10000X magnification.

An optical image shown in Figure 30 of a dilatometry sample cooled at 1°C/s clearly displaying basket weave, parallel plate structure and grain boundary allotriomorphs (GBA). As the cooling rate increased, the volume fraction of basket-weave structure became progressively larger and the alpha plates finer in size.

At an intermediate cooling of the zirconium-2.5niobium alloy, it has been reported in the literature that the first alpha plates to appear during β/α transformation are grain boundary allotriomorphs (GBA) which form along the high angle grain boundaries of the parent β-phase (Hunt, 1971). Nucleation of secondary fine alpha plates on the GBA's which grow on the same habit plane into the beta grain are called the "parallel plate" structure, see Figure 26. This secondary fine alpha plate's structure is feathery in appearance. Within the grain, the basket-weave morphology was dominant and was composed of intragranular alpha plates that randomly precipitate on a number of planes within the same parent β grain. All these transformations occur through nucleation and growth.

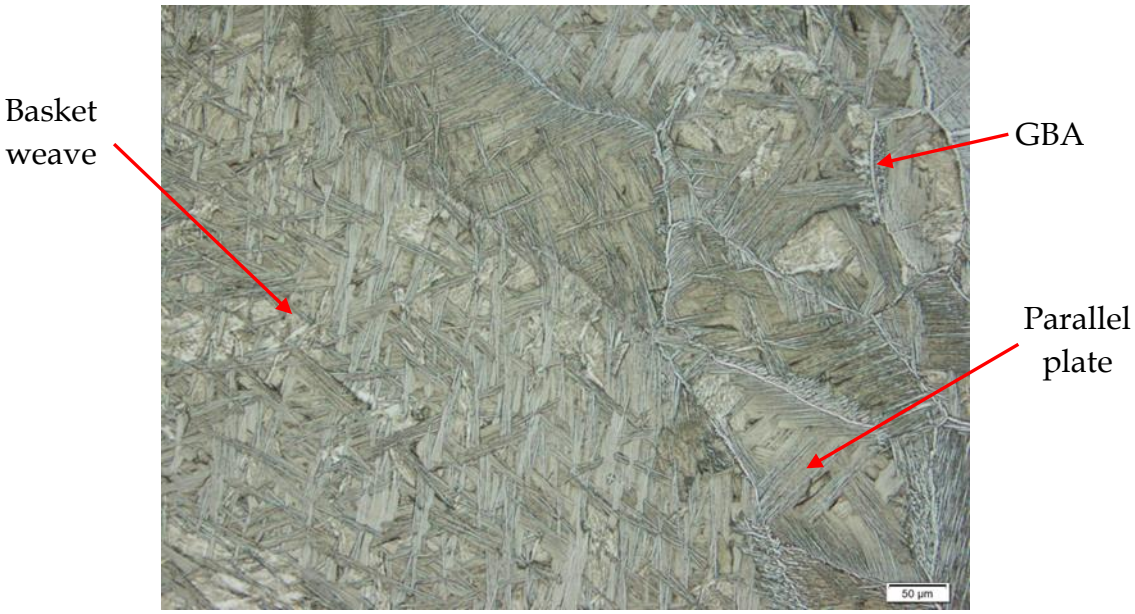

Figure 30: Optical microscopy image of a 1°C/s cooling rate dilatometry sample's microstructure. A mixture of basket weave, parallel plate and grain boundary allotriomorphs (GBA) which form along the high angle grain boundaries of the parent β-phase were found.

5.2 Weld metal geometry

Generally, varying welding parameters can have an influence on mainly three areas of a weld; the weld geometry, weld profile and the morphology. The weld metal geometry was measured from the cross-section of the welded samples using ImageJ software. Figure 31 contains representative micrograph images of both LBW and GTAW cross-sections of welds using a stereoscope. The red shaded area in the image (L5) and (T8) demonstrates how the cross-sectional area was estimated using the ImageJ software. Image (L5) and (L1) are laser beam welds performed at $33.3x10^{-3}$

and 66.6x10^{-3} m/s welding speeds respectively. Image (T8) is a gas tungsten arc weld performed at a 7.54x10^{-3} m/s welding speed.

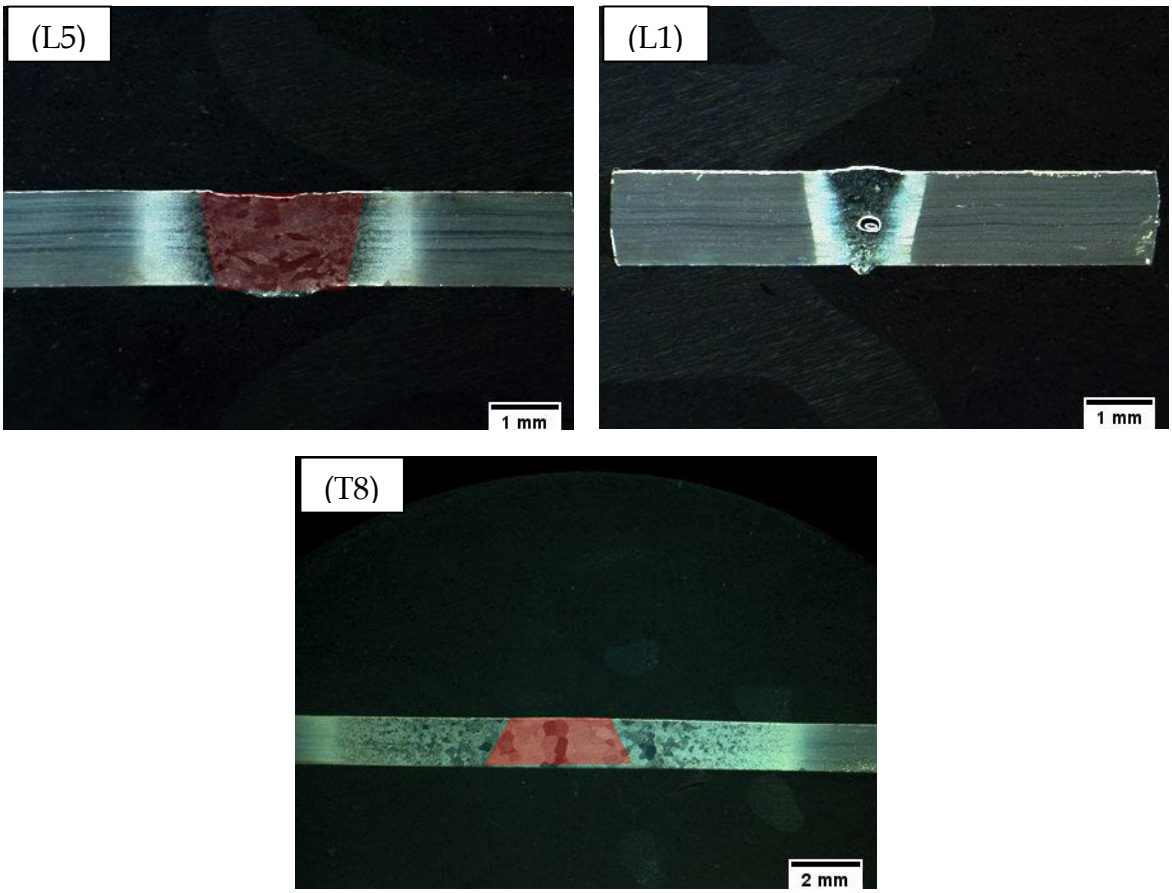

Figure 31: Weld cross sections of LBW (L5, L1) and GTAW (T8).
Image (L5), 33.3x10^{-3} m/s welding speed and 22.8 J/mm heat input,
(L1) 66.6x10^{-3} m/s welding and 8.3 J/mm heat input,
(T8) 7.54x10^{-3} m/s welding speed and 54.3 J/mm heat input.
LBW images were taken at 125X magnification, whilst GTAW image was taken at 85X magnification.

5.2.1 Welds cross-section area and width measurements

Table 12 are the measured values of the welds. The reported weld widths were the average width of the top and the root of the weld metal. The GTAW welds were performed between a heat input ranges of 21.7 to 74.3 J/mm. LBW welds were performed at a lower heat input range of 8.3 to 28.9 J/mm.

Table 12: Welding parameters of LBW stereoscope and SEM images

Welding Process	Weld sample Label	Weld Width (mm)	Weld cross-section area (mm^2)
Laser beam welding	L1	0.8	1.1
	L2	1.4	1.8
	L3	1.3	1.9
	L4	1.8	2.7
	L5	2.2	3.1
	L6	2.1	3.1
	L7	1.7	2.3
	L8	2.6	3.4
	L9	2.8	3.8
Gas tungsten arc welding	T1	4.2	7.0
	T2	4.9	7.1
	T3	6.2	8.9
	T4	2.1	1.1
	T5	4.4	6.1
	T6	7.2	10.5
	T7	3.2	5.1
	T8	5.3	7.7

Figure 32 shows the measured weld metal cross-sectional area in both LBW and GTAW processes as a function of heat input.

The weld cross–sectional area displayed a linear positive response to increasing heat input irrespective of the welding process. A clear observation is the much larger GTAW welds in comparison to the LBW. Factors that can contribute to the differences in weld size are as follows:

1. LBW welding speeds were almost ten times faster than those applied during GTAW, which explains the difference in the heat input ranges. The weld size is proportional to the heat input which is a function of welding speed.
2. The LBW has a higher efficiency (0.55) than the GTAW (0.26) but the high welding speed restricts the exposure time of the base metal to the laser beam for energy transfer.

Extending the trend-lines in Figure 32 to intersect the x-axis indicates that there is a minimum amount of heat input that is required for the GTAW process before melting (weld pool) can occur as compared to LBW.

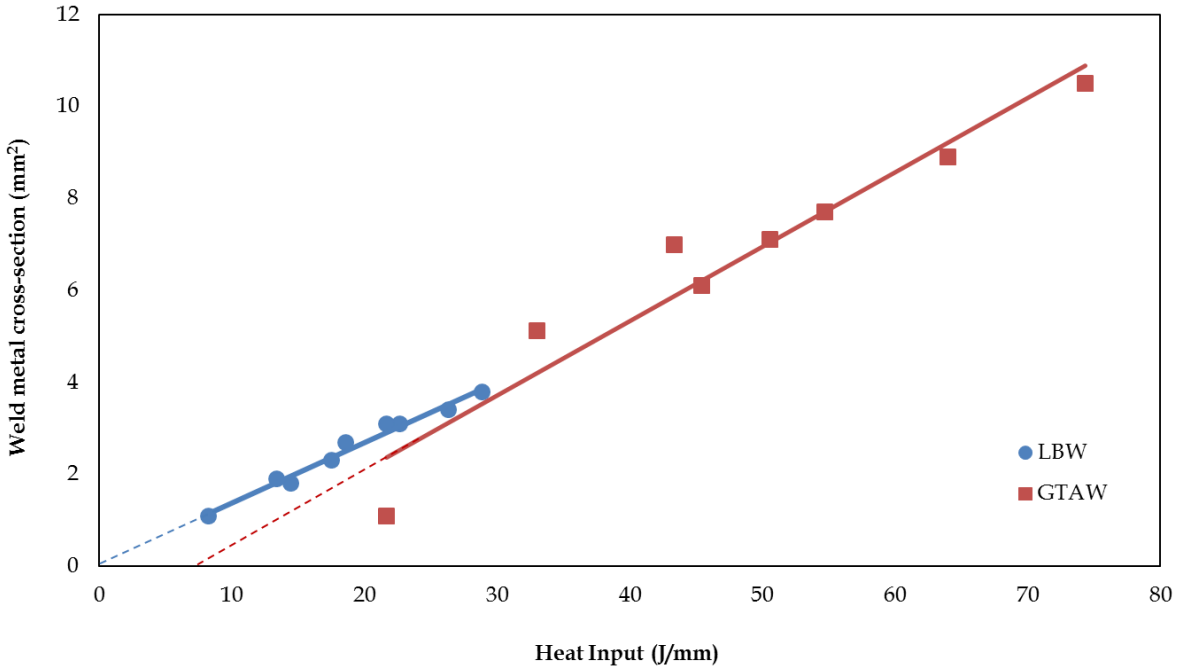

Figure 32: Effect of heat input on the weld metal cross-sectional area. LBW welds were smaller than GTAW welds but both showed a similar correlation to heat input.

The weld metal profile of all LBW welds displayed a parallel-sided fusion line except for the L1 weld which displayed a V-shape, as seen in Figure 31. The L1 weld was performed with a heat input (HI) less than half the average of the HI for laser welds. The parallel-sided fusion line profile is typical of LBW in keyhole mode. GTAW welds remained U-shaped through the whole heat input range.

5.3 Metallography of welded samples

Metallography images of both GTAW and LBW samples presented in this sub-section were evaluated using stereoscopy (Olympus SZX7) and Scanning electron microscopy (Zeiss Ultru-plus FEG SEM). Representative images of welds performed at low and high heat-input of the slowest and the highest welding speeds are included.

5.3.1 Microstructure of gas tungsten arc welds

The changes in microstructure morphology of the welds with varying welding parameters are shown in Figure 33. The stereoscopic images (T1 and T7) in Figure 33 were taken at 100X magnification whilst those of T3 and T8 were taken at a 80X magnification. The difference in magnification was necessitated by the need to show the whole weld profile in one complete image.

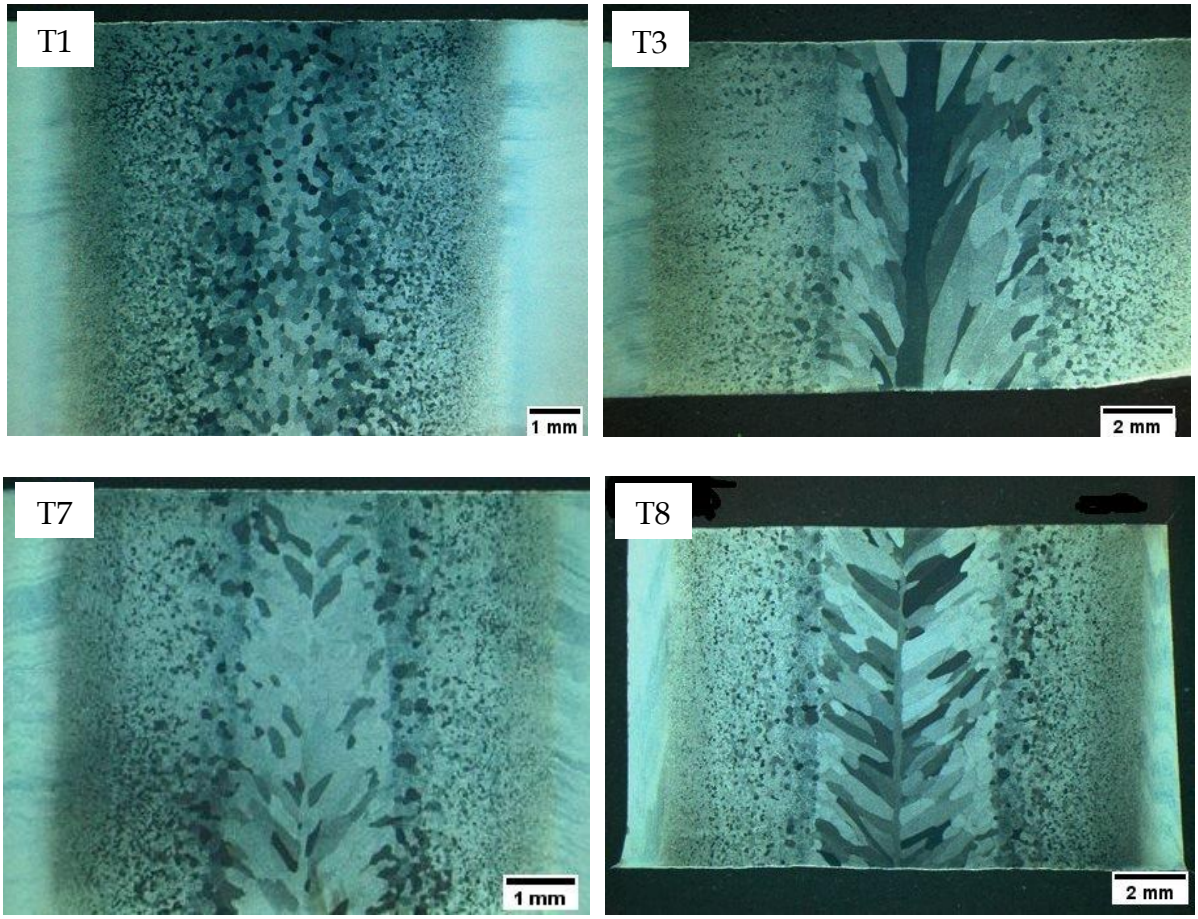

Figure 33: GTAW stereoscopic images.The change in microstructure morphology from equiaxed to columnar grains with varying welding parameters. Welding speed and heat Input: (T1) 3.43x10^{-3} m/s ; 43.4 J/mm, (T3) 3.43x10^{-3} m/s ; 64.0 J/mm, (T7) 7.54x10^{-3} m/s ; 33.0 J/mm, (T8) 7.54x10^{-3} m/s ; 54.7 J/mm

At low heat inputs and welding speeds, the microstructure of both the HAZ and weld metal are characterized by equiaxed grains as shown in image (T1). As the heat input increases, the weld metal structure initially consists of large equiaxed grains and then transitions to columnar grains towards the center.

SEM images shown in Figure 34 are representative of the GTAW weld's microstructural constituents.

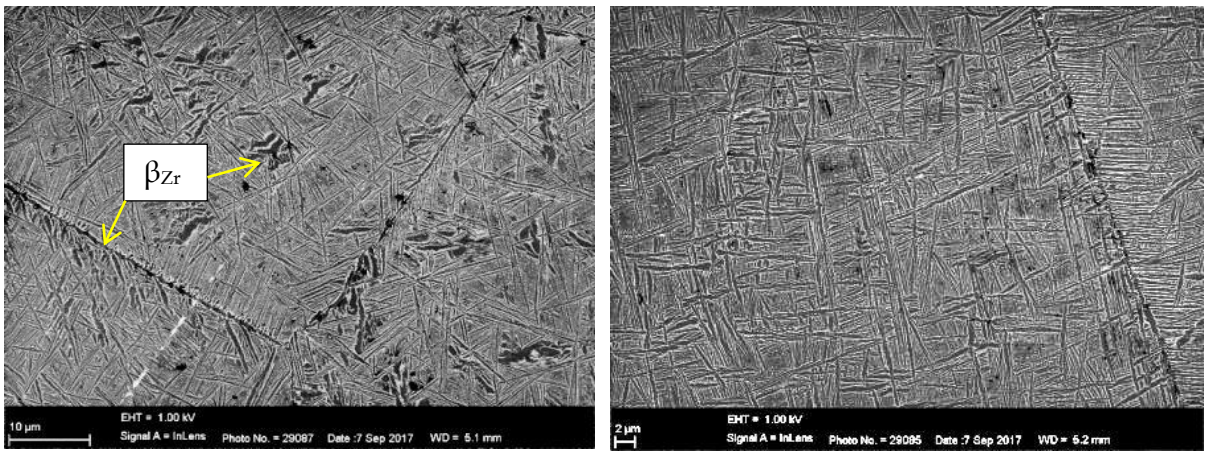

Figure 34: GTAW SEM images showing HAZ and weld metal sample welded at $7.54x10^{-3}$ m/s speed and 54.7 J/mm heat input.
Yellow arrows pointing at the retained beta phase. 5000X magnification

The heat affected zone consisted mainly of the basketweave structure with a small amount of alpha parallel plates nucleating on the grain boundaries. The HAZ exhibited a finer structure with a decrease in heat input. Retained beta (β_{Zr}) phase was observed on the grain interior and grain boundary. If the critical cooling rate to form martensite is not achieved, the metastable beta (β_{Zr}) phase will be retained at room temperature.
The weld metal showed a more uniform basketweave structure. The grain boundaries contained retained β_{Zr} phase with fine parallel plates nucleating from it. No retained β_{Zr} phase was observed on the interior of the weld metal grains.

5.3.2 Microstructure of laser beam welds

A total of nine laser beam welds (LBW) were performed with varying welding parameters. Visual analyses of images obtained through stereoscopic means show equiaxed grains in the heat affected zone (HAZ) with increasing grain size until the fusion line is reached. The HAZ is clearly distinguishable from the weld metal at slower welding speeds as seen in Figure 35. The weld metal consists of large columnar grains which transitioned to finer smaller equiaxed grains with increasing welding speed.

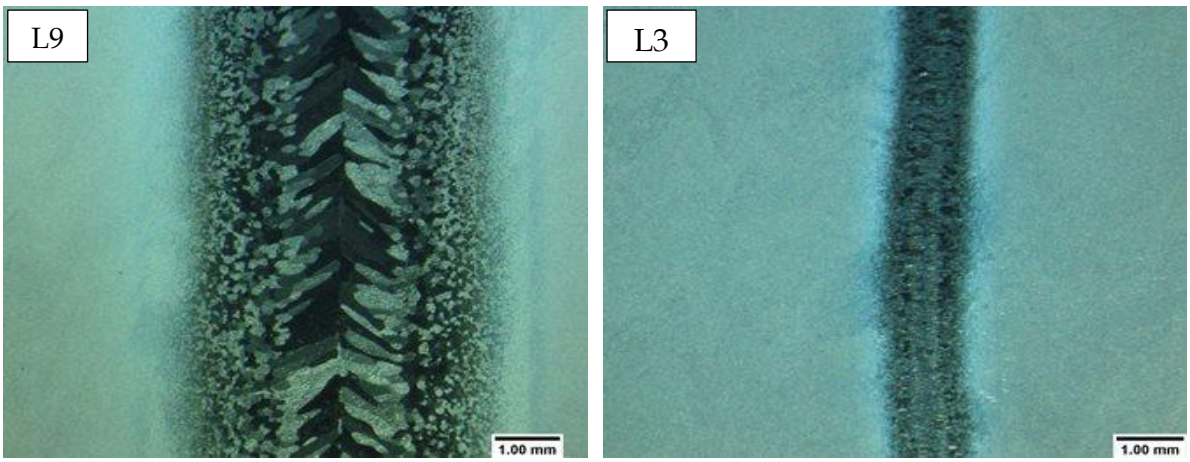

Figure 35: LBW stereoscopic images. L9 shows equiaxed grains in the HAZ and mainly columnar grains in the weld metal. L3 exhibits equiaxed grain in both HAZ and weld. Welding speed and heat Input: (L9) 16.7x10^{-3} m/s; 28.9 J/mm, (L3) 66.7x10^{-3} m/s ; 13.4 J/mm,. 100X magnification

All of the laser beam welds showed similar microstructural constituents and Figure 36 shows images of representative microstructures taken at 10000X magnification.

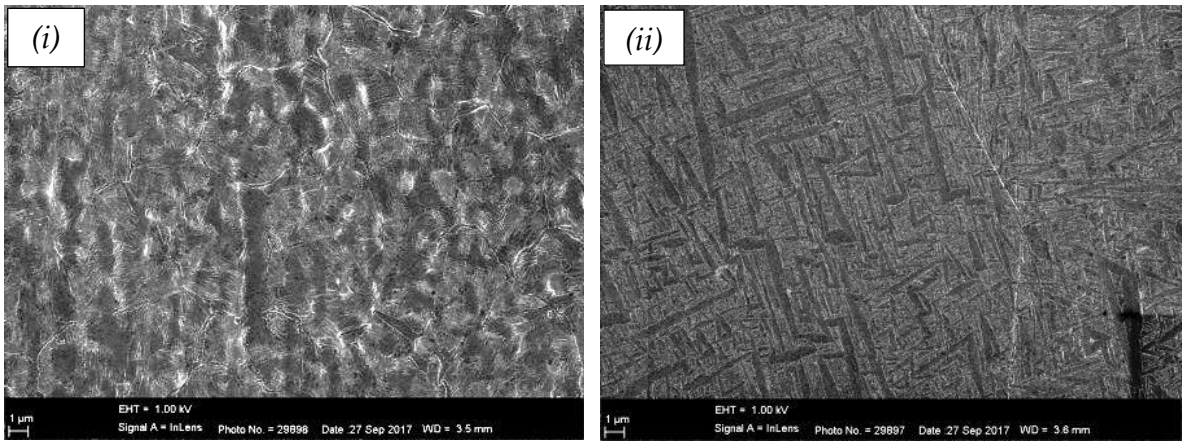

Figure 36: Laser beam weld's SEM images showing (i) the HAZ with a complex structure of Widmastätten, retained beta and martensite and (ii) weld metal consisting of a fully martensitic structure. L9 sample welded at 16.7x10^{-3} m/s speed and 28.9 J/mm heat input. 10000X magnification

The heat affected zone of the laser welds contained a more complex microstructure. The hybrid microstructure consisted of martensite, basketweave structure and retained beta phase. The amount of martensite decreased as you moved away from the fusion line. This observation is supported by the fact that some regions in the HAZ were partially transformed.

The weld metal consisted of a fully martensitic microstructure. The acicular plates were arranged very similarly to those in dilatometry samples, forming along different variants of the habit plane. The microstructural morphology and constituents were consistent with the dilatometry samples for all the welds as per the corresponding cooling rates.

5.4 Hardness Results

All hardness tests were performed using 500g/f load on the micro-Vickers machine.

5.4.1 Dilatometry Hardness Results

To determine the effect of the cooling rate on the hardness, ten random measurements were done on each of the EBW dilatometry samples. The results are presented in Table 13. Results of the base metal sample which are included in Table 13 averaged 210 $Hv_{0.5}$ with a confidence interval of 7.

Table 13: Dilatometry and base metal sample's micro-Vickers hardness results (load 500 g/f)

Cooling rate (°C/s)	Hardness ($HV_{0.5}$)			Std. Deviation	95% CI
	Min.	Max.	Ave.		
0.5	187	229	206	14	10
1	185	221	207	10	7
10	220	243	230	9	6
25	229	260	249	10	7
50	254	274	262	7	5
150	267	290	276	8	6
300	264	291	278	9	6
600	258	282	278	8	6
Base metal sample	196	224	210		

Figure 37 and Figure 38 schematically show the effect of cooling rate on the zirconium-2.5niobium's hardness. Initially, a rapid increase in hardness from ~205 to 260 $HV_{0.5}$ (average) was observed between the cooling rates of 0.5-50°C/s. The hardness improvement corresponded to the increased volume fraction of basketweave structure and refinement of alpha plates. The hardness then plateaus with the values ranging ~270-280 $HV_{0.5}$ between the cooling rates of 150-600°C/s. At these cooling rates, the microstructure was fully martensitic.

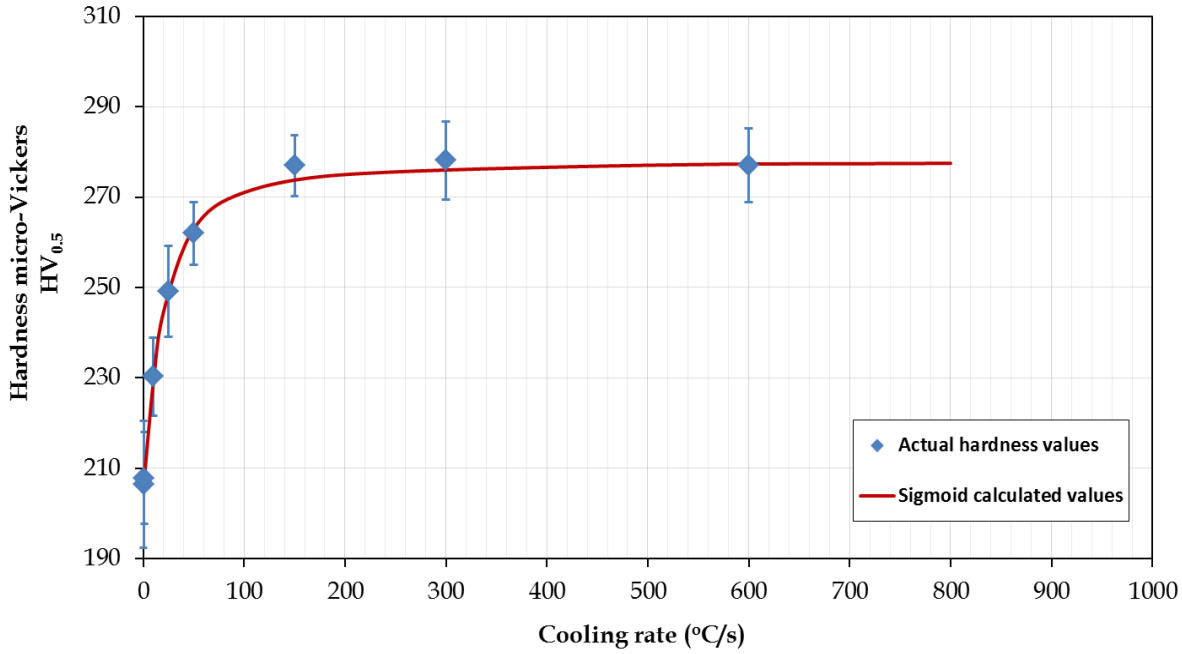

Figure 37: Dilatometry samples showing the effect of cooling rate on the hardness, expressed as the Micro-Vickers hardness, determined using with 500g/f load.

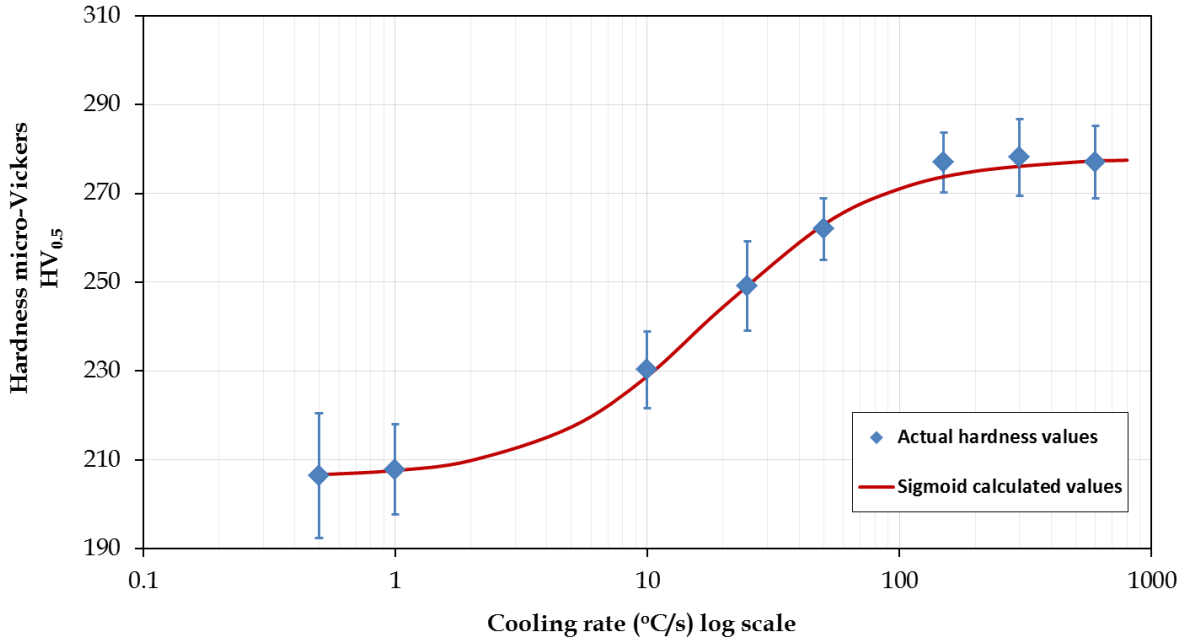

Figure 38: Dilatometry samples showing the effect of cooling rate on the hardness plotted on a log scale.

5.4.2 Hardness of welded joints

The influence of cooling rate on the microstructure and hardness of the welds in zirconium-2.5niobium has been clearly demonstrated on dilatometry results. In addition to better understand the welding transformation products through their hardness properties, it was of interest to determine whether the same response of hardness to cooling rate as seen in the dilatometry samples will be observed during welding. The cooling rate after welding is mainly influenced by the heat input and consequently, this affects the resulting microstructure.

Hardness results of the HAZ and weld metal from both welding processes are presented in Figure 39 as a function of heat input. Table 14 contains the average hardness values of HAZ and weld metal. The weld metal of LBW samples which consisted of a fully martensitic structure, showed no change in hardness with increasing heat input. These observations are consistent with microstructure and hardness values of dilatometry samples cooled at 150°C/s and above. The LBW heat affected zone's hardness indicated a slight softening with increasing heat input. Similarly, the GTAW welds and heat affected zone observed the same trend. LBW welds are slightly harder than those performed with the GTAW process even at similar heat inputs. The higher hardness in LBW welds is attributed to the very high welding speed and small spot size of the laser beam which results in the smaller weld pool. Consequently, the heat is dissipation faster and therefore a higher cooling rate is found.

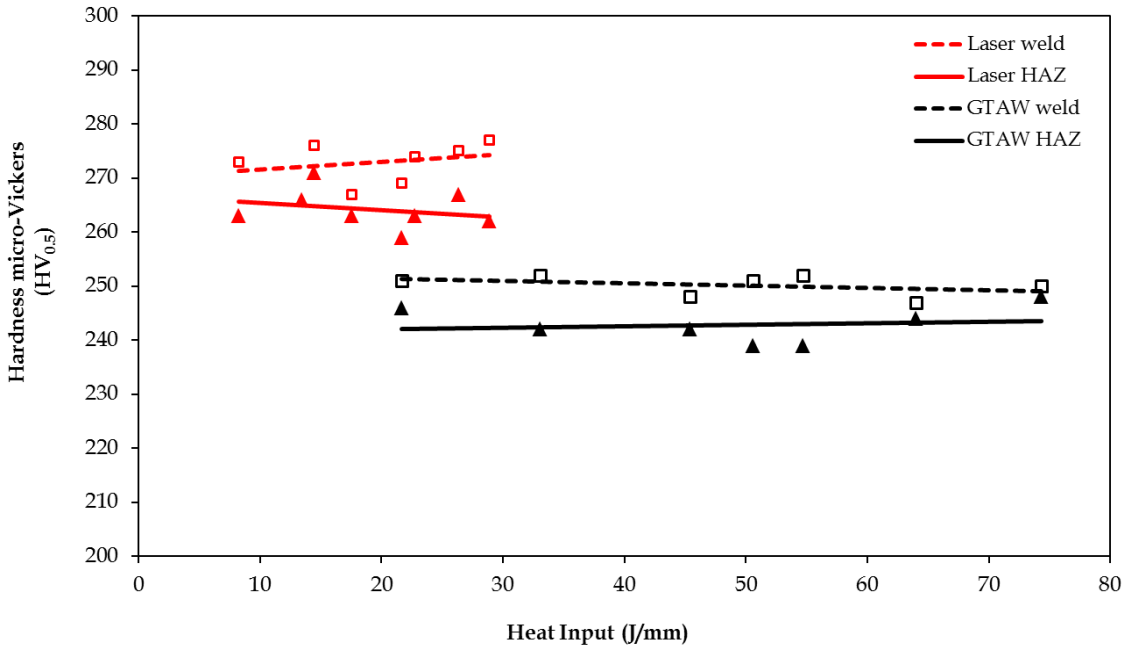

Figure 39: Effect of heat input on the heat affected zone and weld metal hardness values for both LBW and GTAW.

Table 14: Average hardness values of HAZ and weld metal ($HV_{0.5}$)

Welding Process	Weld Sample Label	HAZ	Weld Metal
Laser beam welding	L1	263	273
	L2	271	276
	L3	266	258
	L4	273	265
	L5	263	274
	L6	259	269
	L7	263	267
	L8	267	275
	L9	262	277
Gas tungsten arc welding	T1	261	268
	T2	239	251
	T3	244	247
	T4	246	251
	T5	242	248
	T6	248	250
	T7	242	252
	T8	239	252

5.5 Tensile Testing

Five samples were tested, including two samples of LBW welds, two of GTAW welds and one of the as-received sheet. Both LBW and GTAW welds were performed at a similar heat input. Table 15 contains the average values of the tensile results, as read from the stress-strain curves presented in Figure 40.

Table 15: Average tensile test results of Zr-2.5Nb.
LBW, GTAW and base metal sub-size samples were tested at room temperature.

	Tensile Strength (MPa)		Yield Strength 0.2% strain offset (MPa)		Total Elongation (%)		% width Reduction
Laser	895	902	824	818	7.6	9.8	11
GTAW	780	762	660	693	13.7	15.1	23
No weld (as received)	680		656		19		28

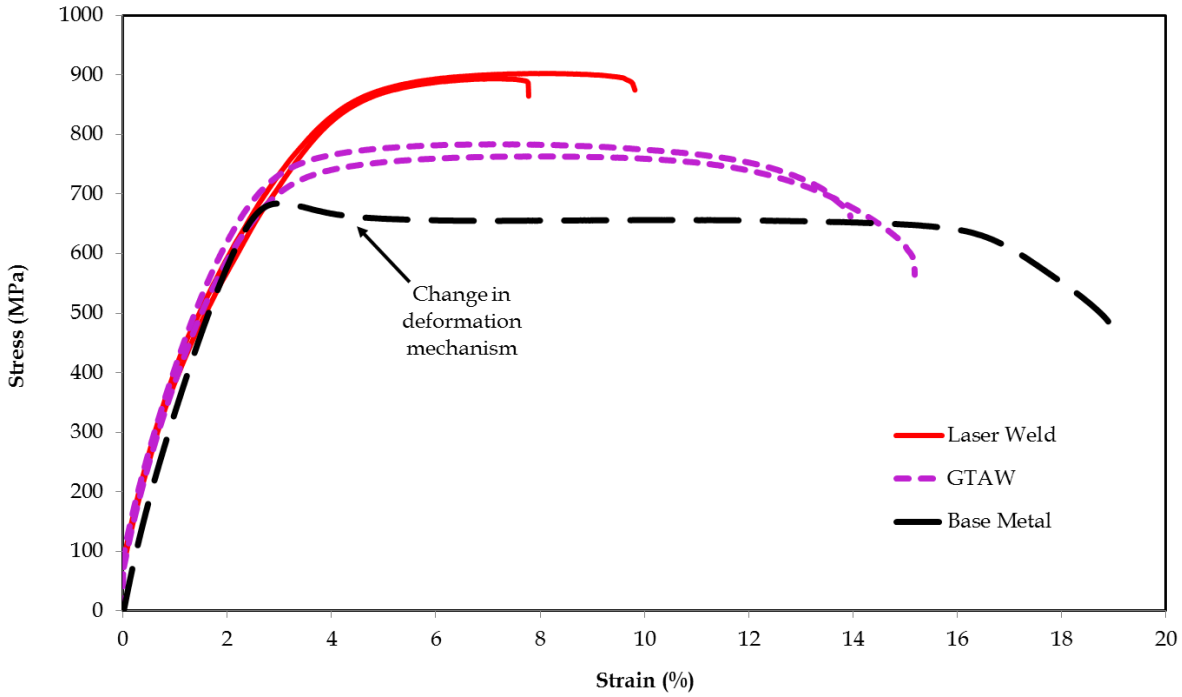

Figure 40: Stress-Strain curves from tests at room temperature with a cross-head speed of 2 mm/min

The tensile test curves observed in Figure 40 are typical of zirconium deformation at room temperature, where initially plastic yielding is smooth and the flow curve gradually plateaus leading to a point in which the rate of dynamic recovery is equal to the hardening rate. As explained in Chapter 2, deformation in hcp zirconium alloys is accommodated by the activation of either the slip or twinning systems. At room temperature, zirconium initially deforms dominantly through slip until a transition (critical) point is reached where the onset of uniform twinning deformation occurs. The transition point can be clearly seen in the "base metal" curve. After the onset of plastic deformation, some strain softening occurred (at an engineering strain of about 4 percent), followed by a constant flow stress (up to a strain of about 15percent).

Figure 41 presents the stereoscopic images of the LBW, GTAW and un-welded broken samples. The width of the reduced tensile sample section was machined to 6 mm. The reduced section of the LBW sample consisted of the weld metal, heat affected zone (HAZ) and the base metal. The GTAW reduced section is without the base metal because of a larger HAZ. The base metal on the LBW samples might have had an effect on the overall tensile properties, but the test was performed for comparative purposes only.

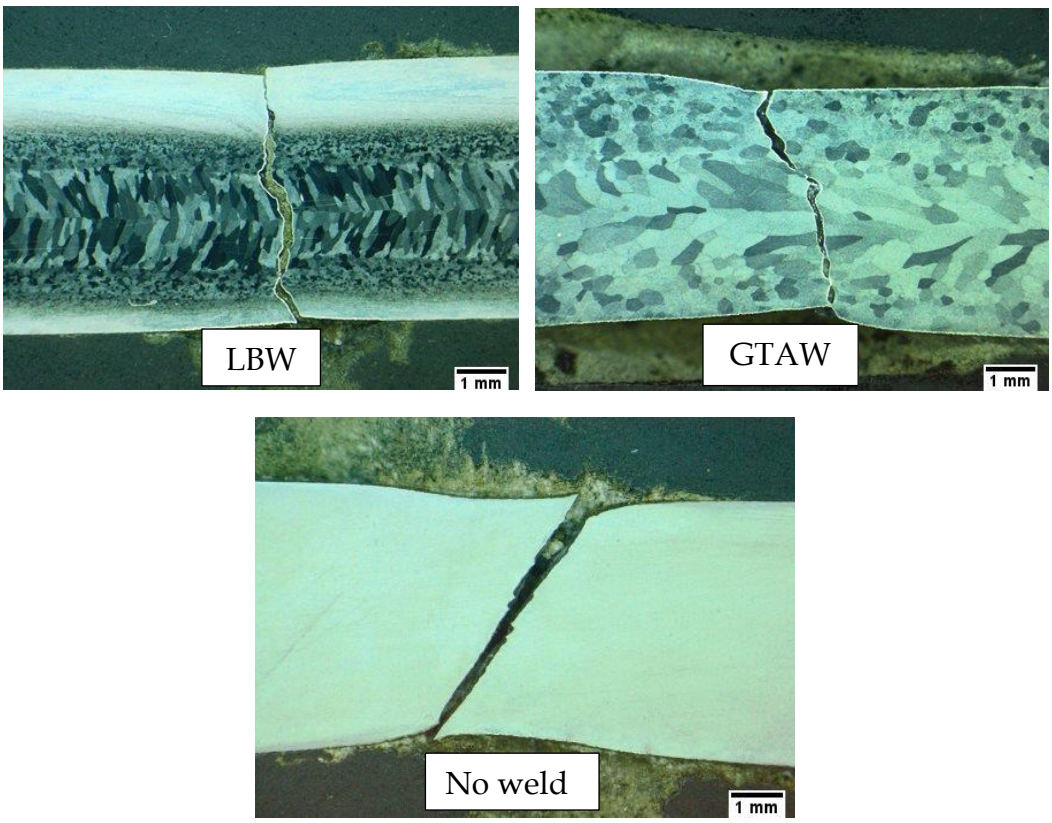

Figure 41: Stereoscopic images of broken tensile samples. Welds were performed at 45 J/mm heat input. Magnification 125X.

Because of the role of pressure tubes as the secondary containment of hot pressurized coolant in the nuclear reactor, it was critical to study the fracture surface to help understand the fracture mode during failure. The fracture surfaces of the broken tensile samples were analyzed with SEM and presented in Figure 42.

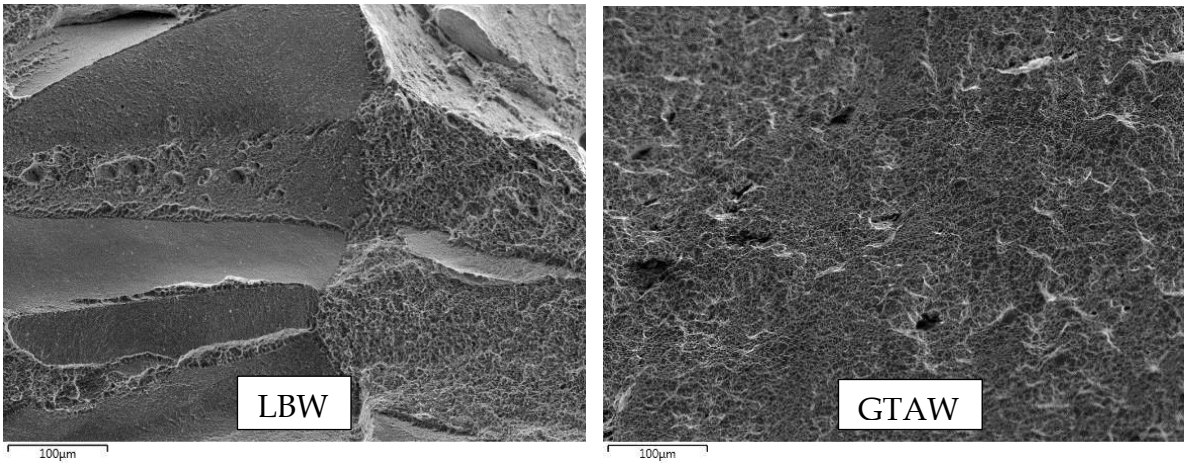

Figure 42: SEM (Jeol JSM) images of the broken tensile fracture surface: The LBW sample exhibits a mixture of brittle and ductile fracture whilst the GTAW sample exhibits a full ductile fracture

The base metal fracture was at an oblique angle which suggests a shear failure and showed the highest width reduction of 28 percent. The fractured surface exhibited very uniform fine dimples with no evidence of shear lips.

Visually the LBW showed a square fracture with some shear on the edges and the least width reduction of 11 percent. This fracture appearance is attributed to the martensitic welds with unaffected base metal on the outside edges. The greater contribution to width reduction was likely the softer base metal on the edges. A mixture of both transgranular and intergranular in the LBW fracture was evident. Along the grain boundary (intergranular), the fracture was very smooth which indicates a cleavage fracture but the transgranular surface was rough and dimpled, indicating a ductile fracture.

The GTAW broken samples exhibited a greater width reduction than the LBW sample which measured 23 percent. The GTAW fracture was also at an oblique angle but slightly wider than that of the base metal. This fracture was an indication that the GTAW welds were more ductile than that of the LBW but of lesser extent than that of base metal, which agrees with the total elongation results in the stress-strain curve. The GTAW fracture appeared transgranular with a uniform dimpled surface.

The characteristic shape of the stress-strain curves for both welding processes was very similar.

5.6 Summary of Results

Transformation temperatures:

- The monotectoid temperature was found to range from 611 to 640°C with increasing heating rate of 0.5-10°C/s.
- The ratio $(\alpha+\beta)\ /\beta_{(Zr,Nb)}$ was more uniform at average temperature of 876°C

The observed beta start and finish transformation temperatures were progressively lowered with increasing cooling rates, ranging between 865-756°C at the start and 680-512°C at the finish.

Microstructure:

At slow cooling rates, the zirconium-2.5niobium alloy showed a Widmanstätten microstructure. It consisted mainly of a basket weave structure with a small volume fraction of parallel plate structure and grain boundary allotriomorphs (GBA). Cooling rates of 150°C/s and above exhibited an acicular martensite.

The microstructures of GTAW welds exhibited a basket weave structure in both the HAZ and weld metal, with retained beta phase observed in the HAZ of some welds. The LBW microstructures consisted of a mixture of martensite, retained beta and Widmanstätten structure in the HAZ with a fully martensitic weld metal.

Hardness:

The Widmanstätten microstructure showed an increase in hardness with increasing cooling rate. The hardness ranged between ~205-260 $HV_{0.5}$ for a cooling rate of up to 50°C/s. At cooling rates above 150°C/s where the microstructure is fully martensitic, the hardness averaged 270-280 $HV_{0.5}$.

Tensile:

Both LBW and GTAW welds were performed at a similar heat input. The LBW weld had a higher ultimate tensile strength (UTS) of 820 MPa when compared to the GTAW's UTS of 675 MPa, on average. The higher UTS was due to the higher cooling rate in LBW welds and a much finer martensitic structure. Both the fracture surface and elongation indicate a more ductile GTAW welds

CHAPTER 6

Discussion

6.1 Practical welding

Good quality autogenous welds free of any discontinuities were achieved with both gas tungsten arc and laser beam welding processes. The most challenging and critical step in the welding process was ensuring good shielding to avoid contamination. Visually all the welds were free of the detrimental contamination. Zirconium is a reactive metal and has high solubility for elements like oxygen and nitrogen, especially at elevated temperatures. The weld metal had a slightly lower hardness than the dilatometry tested samples, at the same cooling rate. Therefore, any contamination that might have occurred was insignificant, and did not cause an increase in hardness and embrittlement. The zirconium-2.5niobium alloy displayed good weldability as stated in the literature.

The resulting phase transformation products after welding are greatly influenced by the prior thermo-mechanical processing on the base metal. As the material used in this research project was supplied in the cold worked and stress relieved condition and welded as is, this had implications on the resulting structure, more specifically in the heat affected zone. Prior to the thermal treatment, the dilatometry samples were electron beam welded. They were then heated to a peak temperature of 1050°C in the single-phase beta region and held for 10 minutes. This soaking time was sufficient to achieve stable homogeneous conditions. The differences between dilatometry and welded samples are therefore to be taken into consideration when interpreting and comparing results.

6.2 The Zirconium-2.5niobium transformation temperature during thermal treatment

Under equilibrium conditions, the transformation temperature and phase products of any alloy can simply be determined from the available phase diagrams. But non-equilibrium conditions almost always prevail in practical applications and processing. Generally, factors which can influence the transformation kinetics of the material are chemical composition and thermal treatment. The zirconium plate used for this study was alloyed with niobium which is a beta stabilizer, and also contained a fair amount of oxygen which is a strong alpha stabilizer. The niobium and oxygen, therefore, had a strong influence on the transformation temperature. For better control and understanding of the resulting microstructure and properties, it was necessary to study and determine the transformation temperatures of this alloy.

As reported in Table 11 from Chapter 5, the observed monotectoid transformation temperature α/β_{Zr} increased from 611 to 640°C with increasing heating rate. The transformation temperature shifted higher with an increase in heating rate, as observed in Figure 43 which has been previously reported by Forgeron (2000) on a zirconium-1niobium alloy dilatometry results. This transformation temperature change could be attributed to the sluggish thermal diffusion of niobium in zirconium which is from the dissolution of β_{Nb} (niobium rich bcc phase) during heating. The hexagonal crystal structure of the alpha phase has a very low solubility of niobium, accommodating only a maximum of 0.6 atomic percent niobium at the monotectoid temperature. The bcc beta phase (β_{Zr}) has a much higher solubility of niobium with a maximum of 18.5 atomic percent at the monotectoid temperature. Another contributing factor to the delay in transformation is that hcp alpha to bcc beta phase transformation is reconstructive and hence diffusion controlled. This transformation mechanism implies that near neighbor bonds are broken at the transformation front and the product structure is reconstructed by replacing the incoming atoms. The incubation time or delay of the α/β_{Zr} transformation with increasing heating rate could be higher because of the slow niobium diffusion and β_{Nb} dissolution (Beneš 2011).

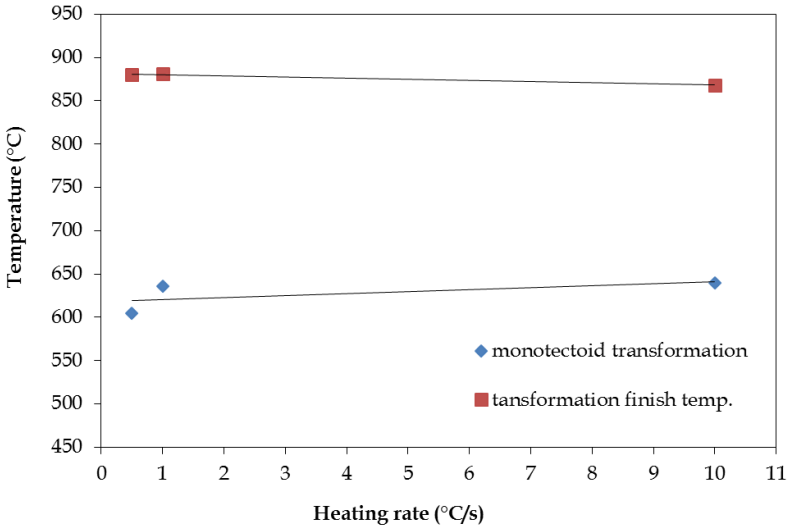

Figure 43: The influence of heating rate on the transformation temperature. The α/β_{Zr} monotectoid transformation temperature has shifted higher with an increase in heating rate. No significant influence on the $(\alpha+\beta_{Zr})/\beta_{Zr,Nb}$ transformation temperature was found.

Dilatometry functions by detecting the dilation of the sample, so it is possible to have a delay in detection of the beta phase until a sufficient volume fraction is transformed. This detection delay grows with increasing heating rate, translating to detection at higher temperatures.

The average observed upper transformation temperature ($\alpha+\beta_{Zr}/\beta_{Zr,\ Nb}$) was 876°C which deviates slightly from the equilibrium transformation temperature of 870°C, as reported by Banerjee & Mukhopadhyay in 2010. The increasing heating rate did not seem to have a significant influence on the ($\alpha+\beta_{Zr}/\beta_{Zr,Nb}$) temperature. The

diffusion rate increases at higher temperatures, which could explain the diminishing influence of heating rate on the transformation temperature.

On cooling the zirconium-2.5niobium alloy from the high-temperature single beta phase, different transformation products can be expected. It can either transform to the equilibrium phases (α and β_{Nb}) or go through a martensitic reaction depending on the cooling rate. At intermediate cooling rates, it is also possible to have retained metastable beta phase (β_{Zr}) at room temperature. During the dilatometry experiment, the observed β-α start transformation temperature was progressively lowered with increasing cooling rates between 0.5 to 50°C/s. The monotectoid temperature displayed a similar trend. As mentioned earlier, the β/α transformation is reconstructive and occurs through nucleation and growth. The process of nucleation and growth is time dependent, and how fast the solutes (niobium) can be rejected by diffusion from the β/α interface during the growth of the alpha phase. Therefore, the observed influence of cooling rate on the transformation temperature was to be expected.

On cooling rates of 150°C/s and above, a martensitic reaction which is a displacive transformation, was observed. This reaction is athemal, which means the martensite start and finish temperatures (M_s and M_f) should be constant for a given alloy. The observed dilatometry results show a depression of transformation temperature with an increasing cooling rate which is not in keeping with martensite transformation theory. Stewart, Hatt, and Roberts (1965) reported a similar observation for an iodide zirconium-3 atomic percent niobium alloy, a depression of the M_s temperature from 750 to 695°C on increasing the cooling rate from 1000 to 3000°C/s. Recently Saibaba (2012) on his microstructural studies on zirconium-2.7niobium presented a CCT diagram (Figure 44) showing a depression in the M_s temperature. Saibaba observed martensite from a 50°C/s cooling rate.

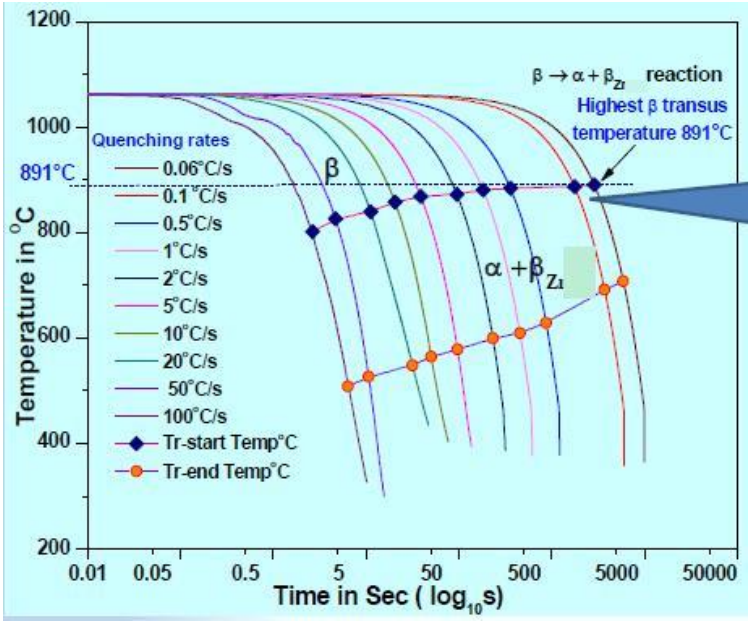

Figure 44: Cooling curves of Zr-2.7Nb showing a depression of martensite start temperature between 50 and 100°C/s (Saibaba, 2012)

6.3 Weld geometry and morphology

The grain structure or morphology of the welded samples was sensitive to the heat input. Both of the laser and GTAW processes display similar weld microstructural constituents and characteristics. The base metal's microstructure was a fine cold worked structure of alpha (α_{Zr}) phase with a very small volume fraction of niobium-rich beta (β_{Nb}) phase. At a low heat input, the microstructure of both the HAZ and the weld metal was characterized by equiaxed grains. As the heat input increased, the weld metal structure initially consisted of large equiaxed grains and then transitioned to columnar grains towards the center line. The equiaxed microstructure in the HAZ showed an increase in grain size as one moves towards the fusion line, due to grain growth. The main difference between the welding processes is the much larger grain size of the GTAW welds and it's HAZ as compared to those of LBW.

Nucleation in fusion welds is dominated by epitaxial growth from the high temperature HAZ. Due to epitaxial solidification and growth, the columnar grains solidify taking the orientation of the heat flow. Non-epitaxial nucleation and growth may occur most likely along the weld centreline where the temperature gradient is shallow. Figure 45 shows the effect of welding speed (which changes the dynamics of nucleation and growth) on the weld metal grain structure.

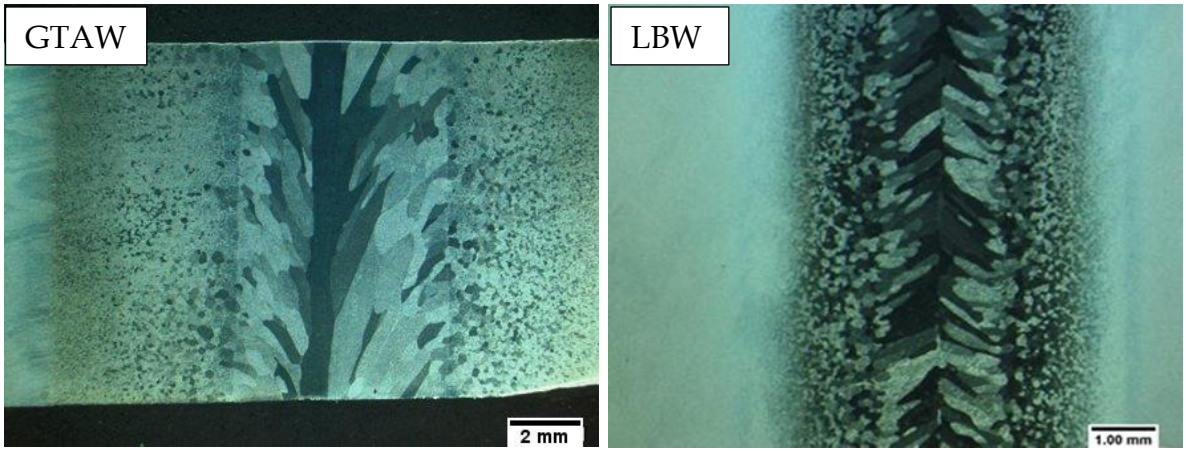

Figure 45: The effect of welding speed on the weld metal grain structure. Low welding speed in the GTAW welds resulted in grain orientation differences when compared to the high welding speed in LBW.

In LBW where the welding speeds are high, grains can grow continuously from the fusion boundary to the centreline until they impinge on those from the other side of the weld. The nature of this centreline makes it susceptible to weld solidification cracking (Lippold, 2014), but no cracks were observed in any of the welds performed. At lower welding speeds, a grain in the center line can grow parallel to the welding direction (Figure 45) which reduces the risk of centerline cracking.

6.4 Phases observed in the zirconium-2.5niobium samples

6.4.1 Base metal

The base material was supplied in the cold worked and annealed condition. The last hot working step during fabrication is performed in the two phase (α+β) region. This step is important to ensure that the desired volume fraction ratio of the two phases and crystallographic texture is achieved after the final anneal. Figure 46 shows the microstructure of the base metal in the as received condition. The structure consists of recrystallized equiaxed grains of alpha and beta phase.

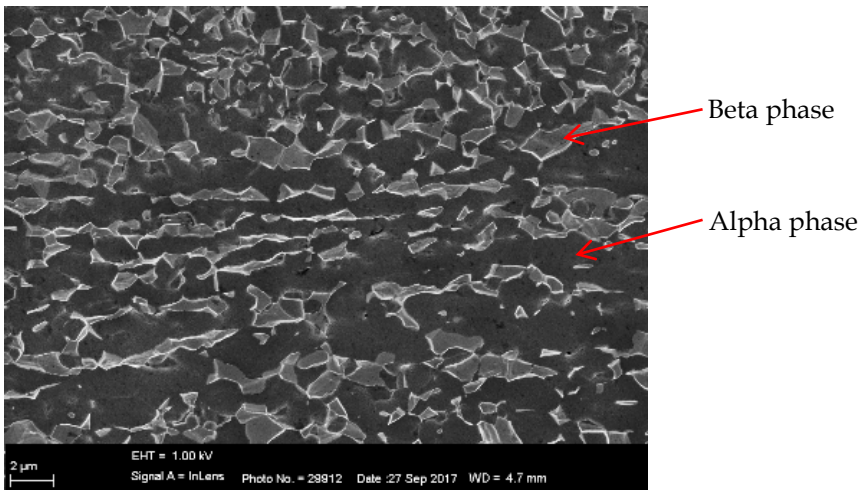

Figure 46: SEM image of the base metal microstructure. The structure constists of recrystallised equiaxed grains of alpha and beta phase. 10000X magnification.

6.4.2 Widmanstätten microstructure

Figure 47 (a) and (b) show a representative microstructure of basket-weave morphology as observed in both welded and dilatometry samples.

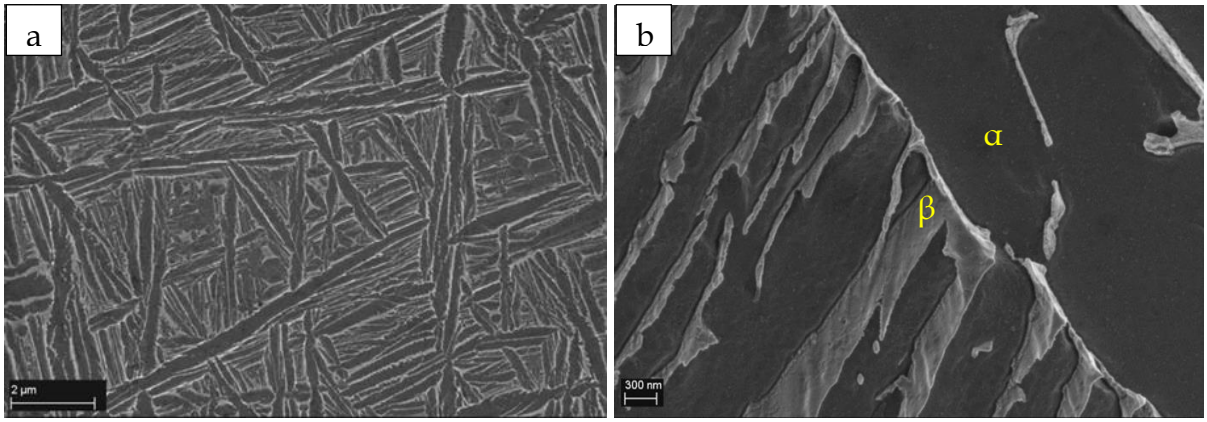

Figure 47: Micrographs of a dilatometry sample (25°C/s) showing the basket-weave structure at a high magnification. Beta phase is observed between the alpha plates. Image (a) and (b) were taken at 20000X and 50000X magnification respectively

6.4.3 Martensite

Fully martensitic microstructures were observed in both laser welds and dilatometry samples cooled at ≥ 150°C/s. Figure 48 shows a representative microstructure of acicular (α′) martensite plates at a high magnification.

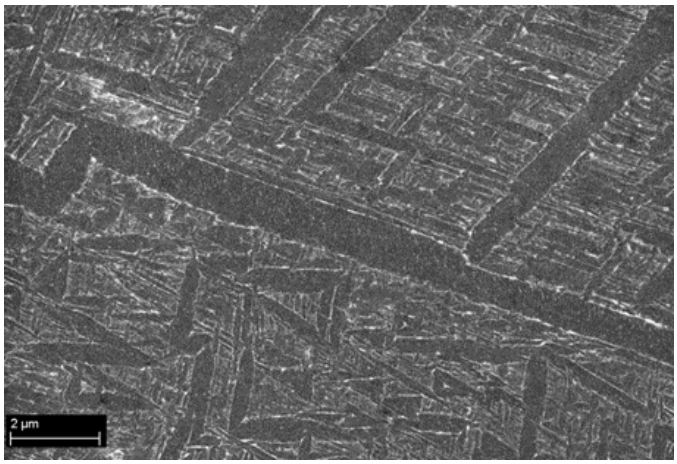

Figure 48: Micrograph of a dilatometry sample cooled at 600°C/s showing acicular martensite plates. 20000X magnification

6.5 Application of the Rosenthal equation to characterize the gas tungsten arc and laser beam welds

To achieve a good comparison of the welded sample's properties to those of dilatometry, it was necessary to characterize the thermal profile of the welds. As mentioned earlier in Chapter 3, the Rosenthal heat flow equation of a moving heat source was used to quantify the influence of the heat input on the weld thermal cycle at a given distance from weld center. The heat flow which can either be two or three dimensional, is a function of plate thickness. Figure 49 demonstrates the two-dimensional heat flow when full penetration is achieved. During the current study, the welding parameters were designed to achieve full penetration; therefore the Rosenthal equation for the thin plate was applied.

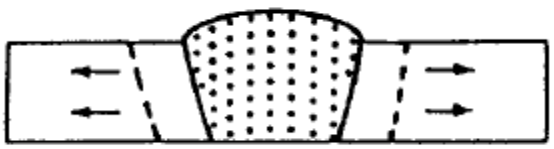

Figure 49: Two-dimensional heat flow when full penetration is achieved

Table 16 is a list of the Zr705 alloy's (zirconium-2.5niobium) material properties that were applied in the Rosenthal equation's calculations. It has been determined through experimental work that the cooling time between 800-500°C is constant

within the heat affected zone if the peak temperature (T_p) is above 900°C (Easterling, 2013). The transformation temperature for the zirconium-2.5niobium at varying cooling rates is between 856–520°C, as determined from the dilatometry results. Therefore, the critical transformation temperature range that was used for calculating the cooling time was revised to 900-500°C (1173-723K).

Table 16: Material properties of Zr-2.5Nb Alloy at room temperature (ASM Handbook vol. 2)

Melting temperature (K)	2113
Plate thickness (m)	$1.5x10^{-3}$
Thermal diffusivity	$9.32x10^{-6}$
Thermal conductivity at 300-500 K ($Wm^{-1}K^{-1}$ or $Jm^{-1}s^{-1}K^{-1}$)	17.1
Volume thermal capacity ($Jm^{-3}K^{-1}$)	$1.835x10^{6}$

(No thermal property data of Zr-2.5Nb was found for elevated temperatures)

6.5.1 The average arc efficiency from the measured weld width

The results of the calculated heat input and the average arc efficiency are shown in Table 17 and Table 18 for both the LBW and GTAW welding processes respectively.

Table 17: Determined arc efficiency from comparing laser beam welding heat inputs (Joules/millimeter)

Weld samples label	Heat Input (welding parameters)	Heat Input (weld width)	Arc efficiency (η)
L1	15.0	8.3	0.58
L2	22.5	14.5	0.67
L3	45.0	13.4	0.24
L4	30.0	18.6	0.62
L5	45.0	22.7	0.50
L6	90.0	21.7	0.30
L7	36.0	17.6	0.52
L8	48.0	26.3	0.55
L9	60.0	28.9	0.48
	Average		**0.55+/-0.1**
	Lowest value		**0.24**
	Highest value		**0.67**
	Standard deviation		**0.135**

Table 18: Determined arc efficiency from comparing gas tungsten arc welding heat inputs (Joules/millimeter)

Weld samples label	Heat Input (welding parameters)	Heat Input (weld width)	Arc efficiency (η)
T1	150.2	43.4	0.29
T2	212.0	50.6	0.24
T3	255.3	64.0	0.25
T4	146.4	21.7	0.15
T5	199.0	45.4	0.23
T6	238.6	74.3	0.31
T7	146.8	33.0	0.23
T8	198.3	54.7	0.28
	Average		**0.26+/-0.04**
	Lowest value		**0.15**
	Highest value		**0.31**
	Standard deviation		**0.050**

The L3 and L6 laser welds in Table 17 were performed at 3000W which resulted in a very poor arc efficiency of 0.24 and 0.30 respectively, when compared with other welds. These two welds were excluded in calculating the average LBW arc efficiency. Full weld penetration was not achieved in the T4 weld of GTAW because the applied welding current was too low. A two-dimensional heat flow was therefore not completely achieved, resulting in a low T4 arc efficiency of 0.15. It was hence also excluded from the GTAW average arc efficiency.

Average arc efficiencies (η) are as follows,

LBW: 0.55

GTAW: 0.26

6.5.2 Analysing the influence of welding parameters on thermal cycle

The main objective of this sub-section is to determine the influence of welding parameters on thermal cycles in the heat affected zone. This knowledge will assist in understanding and predicting the microstructural transformation mechanisms during welding. Equation [9] was applied to calculate the thermal cycle temperatures experienced by a certain fixed point in the fusion line or heat affected zone.

$$T_p - T_o = \frac{\frac{q}{v}}{d\sqrt{4\pi\lambda\rho ct}} e^{-\frac{r^2}{4at}} \qquad [9]$$

Representative thermal curves of GTAW and LBW welds are presented in Figure 50 as a function of temperature and time. Low (T7, L1) and High (T3, L4) heat input welds were selected to highlight the influence of heat input on cooling rate. In all the

welds the cooling rate was initially rapid and then gradually slowed with time. The T7 weld (low HI, high welding speed) required a time of 4 seconds for the temperature to cool from 900-500°C. The T3 weld with high HI and slow welding speed required much longer cooling time of 15 seconds for the same temperature range. Laser welds followed the same trend in relation to the heat input influence on cooling times.

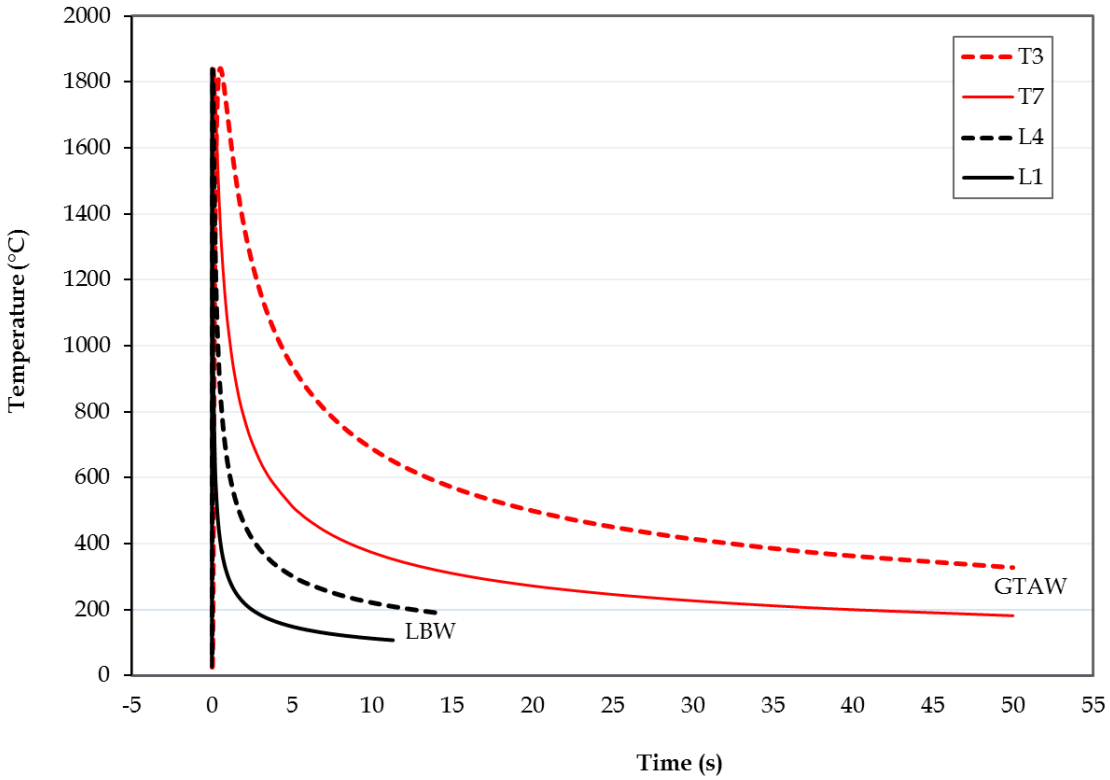

Figure 50: Thermal curves as calculated using the Rosenthal thin-plate solution on the fusion line of both LBW and GTAW. The dotted curves represent welds of higher heat input (HI) in their respective welding processes.
***T3**: 64.0 (J/mm) HI and 3.43x10^{-3} (m/s) welding speed,*
***T7**: 33.0 (J/mm) HI and 7.54x10^{-3} (m/s) welding speed,*
***L4:** 18.6 (J/mm) HI and 33.3x10^{-3} (m/s) welding speed,*
***L1**: 82.6 (J/mm) HI and 66.7x10^{-3} (m/s) welding speed.*

The differences in the temperature profile between LBW and GTAW are clearly evident in Figure 50. Laser welds showed significantly higher cooling rates than the GTAW welds.

It was also necessary to demonstrate the change in thermal profile in the heat affected zone, as the measured point moved away from the fusion line. A GTAW weld was selected because of the larger HAZ than in LBW. Three radial points were chosen from the T8 weld with distances of 0.5, 2 and 5mm from the fusion line. Figure 51 shows the cross-sectional structure of T8 weld, indicating where these points lie in the microstructure. The thermal profiles are shown in Figure 52.

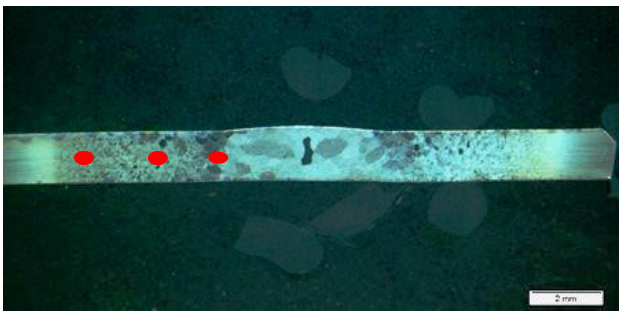

Figure 51: T8 Weld cross section performed at a 7.54x10^{-3} (m/s) welding speed and 54.7 J/mm heat input, showing the three radial points with distances of 0.5, 2 and 5mm from the fusion line. Stereoscopic image at 85X magnification

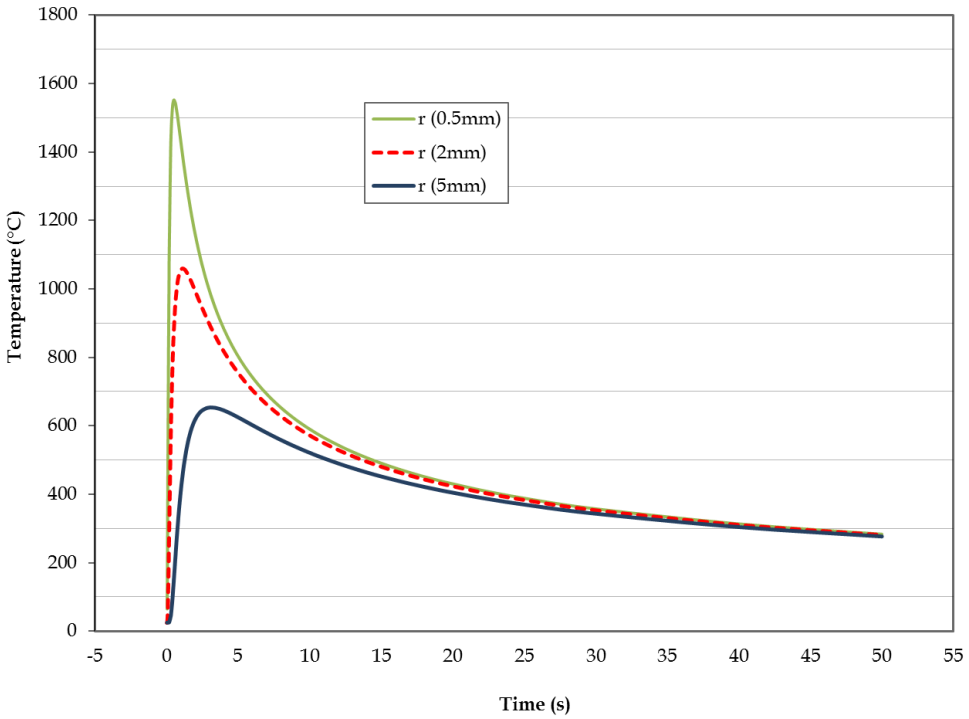

Figure 52: T8 Thermal profiles on the varying distance from the fusion line. (54.7(J/mm) HI, 7.54x10^{-3} (m/s) welding speed)

The peak temperature reduces and is delayed as the distance from the fusion line or heat source increases as clearly shown in Table 19.

Table 19: T8 Peak temperature and time at the HAZ.

Distance from fusion line (mm)	Peak temperature (°C)	Time to the peak temperature (s).
0.5	1552	0.53
2	1060	1.17
5	654	3.10

6.5.3 Calculating the approximate cooling time ($\Delta t_{900\text{-}500}$)

The cooling rate through the transformation temperature range (900-500°C) is critical because it determines the resulting metallurgical transformation products and their properties. The cooling time ($\Delta t_{900\text{-}500}$) will be calculated by substituting the required values in equation [10] and [11].

$$\Delta t_{9-5} = \frac{\left(\frac{q}{v}\right)^2}{4\pi\lambda\rho c\Theta^2 d^2} \qquad [10]$$

$$\frac{1}{(\Theta_2)^2} = \frac{1}{(773-T_o)^2} - \frac{1}{(1173-T_o)^2} \qquad [11]$$

Table 20 gives the calculated cooling times for LBW and GTAW. The T4 weld is highlighted in yellow because full penetration was not achieved and therefore the estimate for the cooling time was probably incorrect. The cooling rate in the fusion line of the laser welds ranged between 136-1664°C/s. A martensitic reaction (β-α') is to be expected above a cooling rate of 50°C/s (Saibaba, 2012). For GTAW welds the cooling range was between 21-60°C/s except for T7 which had a cooling rate of 104°C/s. T7 had the lowest heat input of 33.0 J/mm. The (β-α) phase transformation within these ranges is expected to result in a Widmanstätten structure, manifesting mainly as fine basket-weave morphology.

Table 20: The cooling time ($\Delta t_{900\text{-}500}$) at the fusion line of all welds. The T4 weld is highlighted because full penetration was not achieved.

Welding Process	Weld Sample Label	Heat Input (J/mm)	$\Delta t_{900\text{-}500}$ Cooling time (s)	Cooling Rate (°C/s)
Laser beam welding	L1	8.3	0.24	1664
	L2	14.5	0.74	543
	L3	13.4	0.63	630
	L4	18.6	1.22	329
	L5	22.7	1.82	220
	L6	21.7	1.66	241
	L7	17.6	1.09	368
	L8	26.3	2.44	164
	L9	28.9	2.95	136
Gas tungsten arc welding	T1	43.3	6.63	60
	T2	50.6	9.02	44
	T3	64.0	14.44	28
	T4	21.7	1.66	241
	T5	45.4	7.27	55
	T6	74.3	19.47	21
	T7	33.0	3.85	104
	T8	54.7	10.55	38

6.5.4 Effect of cooling rate ($\Delta t_{900\text{-}500}$) in welded samples

The resulting microstructure as observed in the previous sub-section of dilatometry analysis, is influenced by the cooling rate which is a function of the heat input. The influence of heat input on cooling rate for both welding processes was analyzed and presented in Figure 53. The cooling time ($\Delta t_{900\text{-}500}$) was calculated using the Rosenthal equation from the fusion line of all the welds. As the LBW cooling rates ranged between 136-1664˚C/s, it was expected for all the welds to be martensitic as per the dilatometry microstructure examination. The GTAW weld's cooling rate at the fusion line ranged between 21-104˚C/s. These cooling rates would result in a Widmanstätten structure.

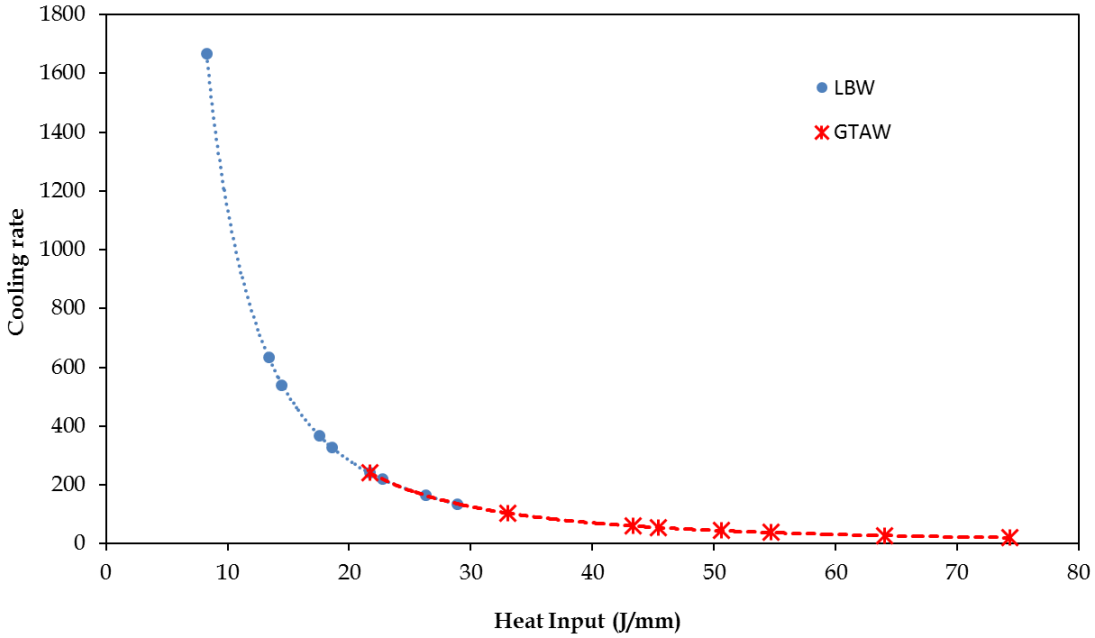

Figure 53: Influence of heat input on a calculated average cooling rate between 900-500°C during laser beam and gas tungsten arc welding. The cooling time ($\Delta t_{900\text{-}500}$) was calculated at the fusion line on all welds.

A GTAW (T5) weld was chosen to calculate the change in peak temperature across the heat affected zone which measured approximately 5 mm in width. Figure 54 shows the decrease of peak temperature from the fusion line. This observed change in peak temperature in the heat affected zone has implications on the transformation kinetics and final phase products. This is therefore important to consider when analyzing the HAZ.

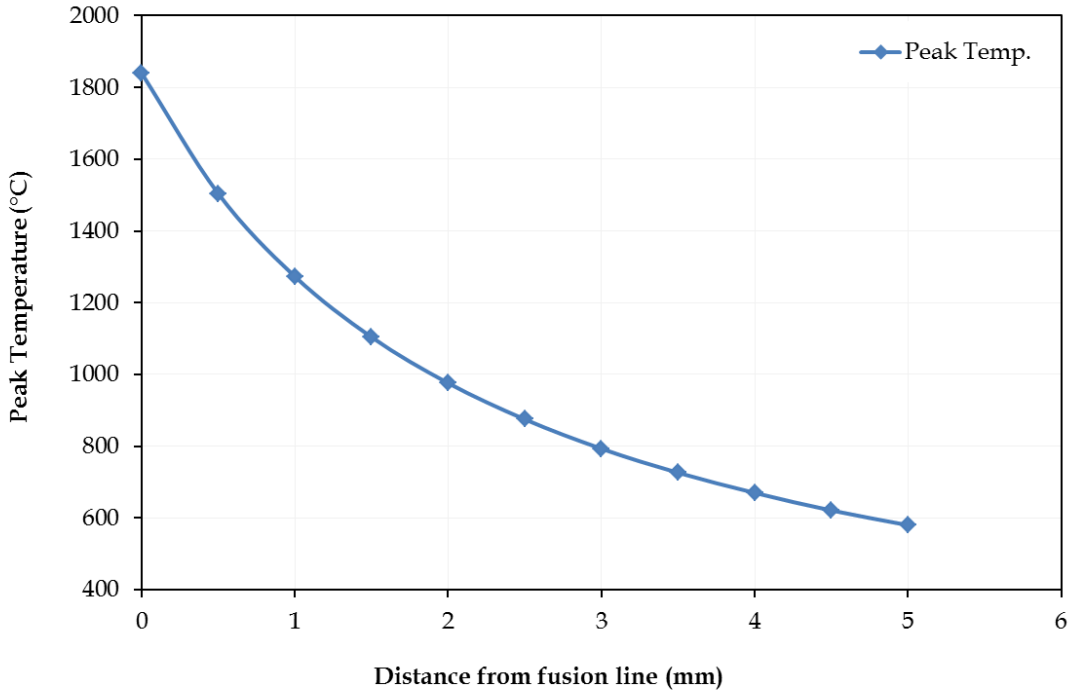

Figure 54: T5 GTAW heat affected zone (HAZ) showing the change in peak temperature with increasing distance from the fusion line. The welding speed and heat Input: 5.02x10^{-3} m/s ; 45.4 J/mm

6.5.5 Sub-regions in the heat affected zone

Because of the different peak temperatures and cooling rates experienced in the heat affected zone, it can be divided into a number of sub-regions. The T5 GTAW weld is again used to illustrate this in Figure 55 where various sub-regions of the heat affected zone corresponding to the zirconium-2.5niobium equilibrium phase diagram, are shown. Tempering of the base metal during the thermal cycle can occur between 450-600°C. In the 450-600°C temperature range, a number of changes can occur including recovery, recrystallization, and decomposition of retained beta to the niobium rich beta (β_{Nb}) phase (Griffiths, 2008). The very short duration of the welding thermal cycles means the HAZ region exposed to the 450-600°C cycle will not have any significant change in the structure or mechanical properties. Generally, aging at 450-550°C for more than 10 hours is required before any β_{Nb} precipitates are observed (Griffiths, 2008) and (Sabol, 1970). Above 620°C (monotectoid temperature), a partial α-β transformation took place. A complex final microstructure of martensite and Widmanstätten in this region can be observed, depending on the cooling rate (Williams, 1966). An increase in strength can be observed in the HAZ regions that experienced thermal cycles above the monotectoid temperature, but this is dependent on the heat input which influences the cooling rate. Homogenisation and grain growth occurs at temperatures in the single beta phase region. It was expected for the varying microstructures in the HAZ sub-regions to possess different mechanical properties.

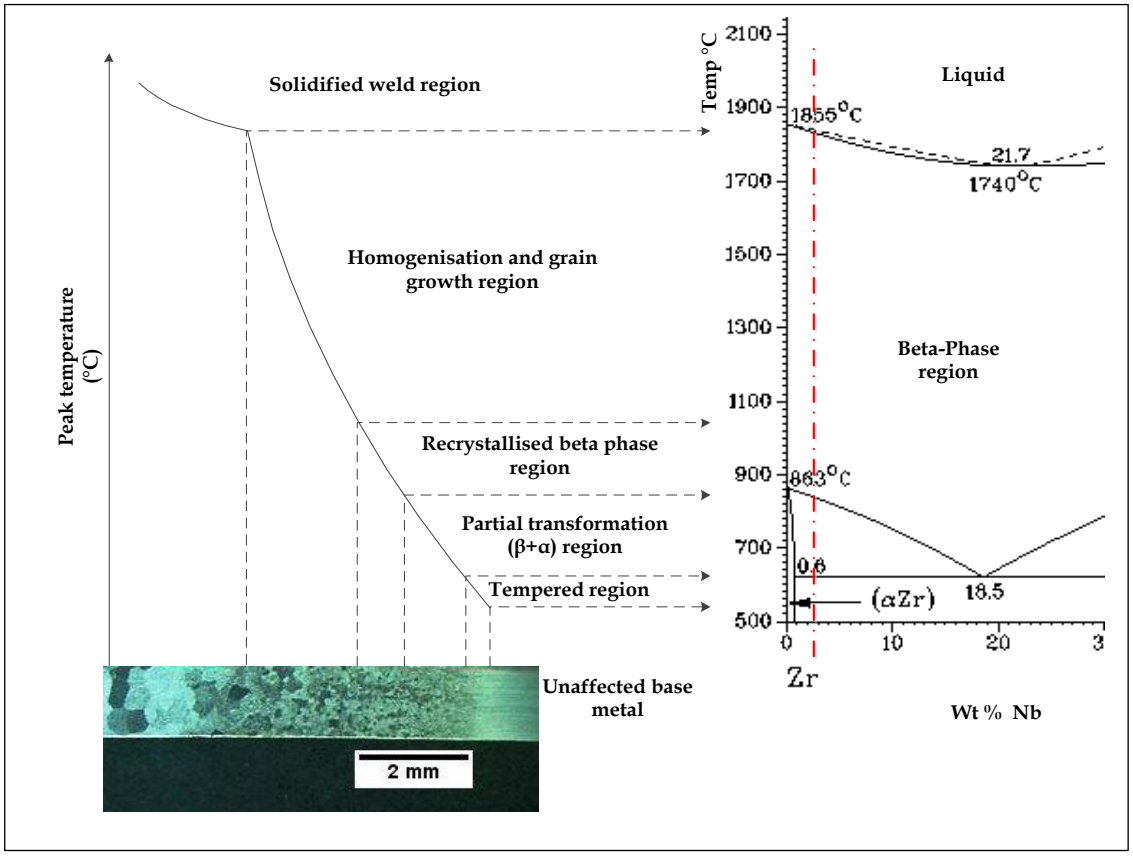

Figure 55: GTAW stereoscopic images of a weld showing the various sub-regions of the heat affected zone corresponding to the Zr-2.5Nb equilibrium phase diagram. Depending on the cooling rate, the bcc-beta (β_{Zr}) phase will transform to hcp-alpha (a) and niobium rich beta (β_{Nb}) or hcp-martensite (a'). Welding speed and heat Input: (T5) 5.02x10^{-3} m/s ; 45.4 J/mm

6.6 Mechanical Properties

6.6.1 Hardness Properties

The hardness results against the cooling rate of welded samples (LBW and GTAW) showed similar trends to the dilatometry results (Figure 56). The hardness of the base metal averaged 210 $HV_{0.5}$ with a Widmanstätten cold worked microstructure. The hardness of LBW samples ranged between 260-275 $HV_{0.5}$ for both the HAZ and the weld metal. The martensitic structure in both the HAZ and weld metal was mainly responsible for the higher hardness. The GTAW welds were slightly lower in hardness than LBW welds. The GTAW weld's hardness increased gradually from 240-265 $HV_{0.5}$ between the HAZ and weld metal. There was a minor discrepancy between the hardness of the weld metal and the hardness of the dilatometry tested samples. The weld metal usually had a slightly lower hardness than the dilatometry tested samples, at the same cooling rate. The reason for this minor discrepancy was not clear, but thought to be related to the difference in peak temperature between weld metal and dilatometry tested samples.

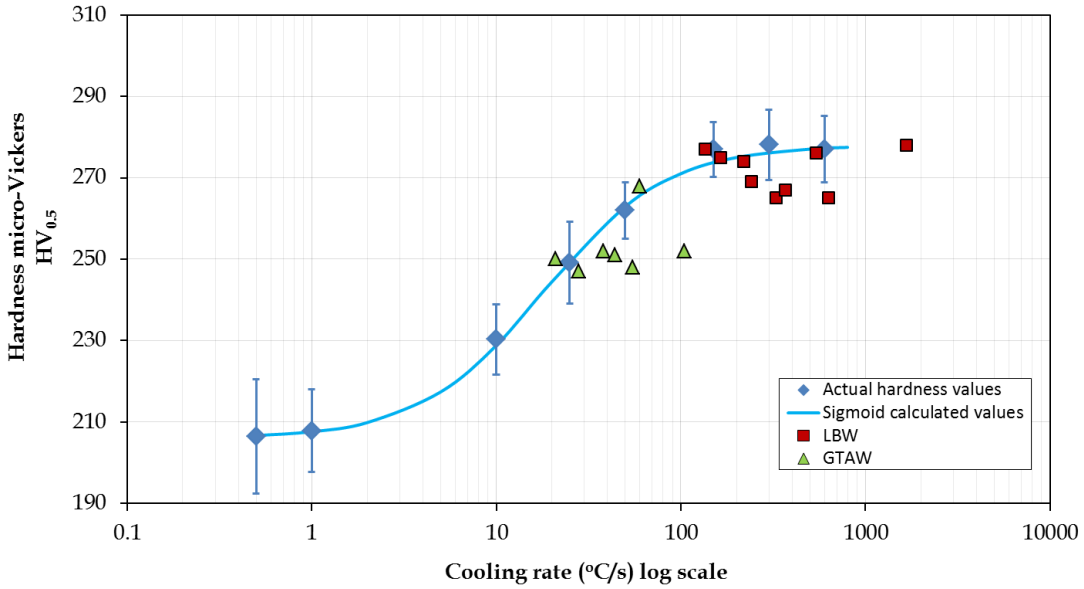

Figure 56: The average hardness values of the weld metal in both LBW and GTAW, showing good agreement with dilatometry tested results in relation to the cooling rate.

6.6.2 Tensile Properties

The laser beam welds showed a higher tensile strength than the GTAW weld metal and the base metal. This can be attributed to the higher cooling rate in LBW and therefore a martensitic structure. The substructure within acicular martensite on the zirconium-2.5niobium alloy generally consists of a high dislocation density and twinning which are detrimental to the ductility but should improve the strength (Banerjee, 2010). The width of the LBW tensile samples contained approximately 35 percent (Figure 57) unaffected base metal due to the narrow laser welds and this had a bearing on the ultimate tensile strength and in improving total elongation. The weld metal and HAZ of GTAW welds formed within the whole reduced section of the tensile sample. The microstructure consisted of mainly basketweave structure and thus exhibits a lower strength than LBW welds but improved ductility.

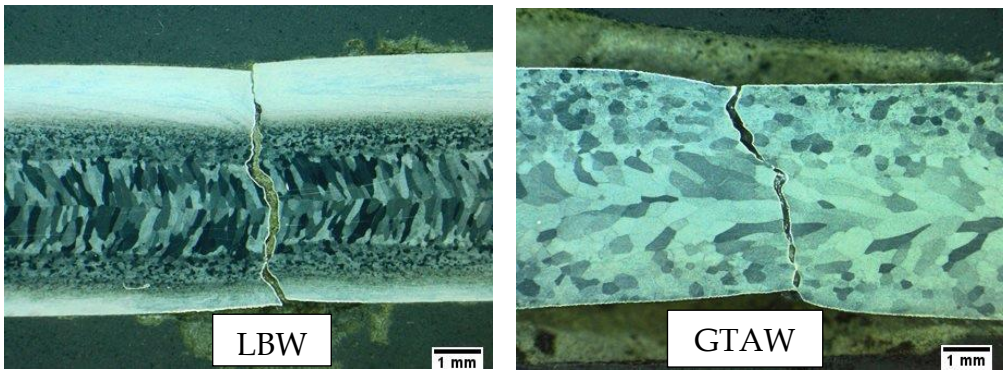

Figure 57: Stereoscopic images of the broken tensile samples. Welds were performed at 45.0 J/mm heat input. Magnification 125X.

Both welding processes resulted in improved strength but reduced ductility when compared to the base metal. The finer grain size of LBW welds seems to have benefited the strength in comparison to the GTAW courser grains. These tensile results corroborate the prior observation that strength improves with cooling rate.

Figure 58 displays the relationship between the Vickers hardness value of the weld metal and maximum strength of the zirconium-2.5niobium. The correlation between hardness and strength was observed to be nonlinear but determined to be approximately:

$$UTS = 3.15Hv$$

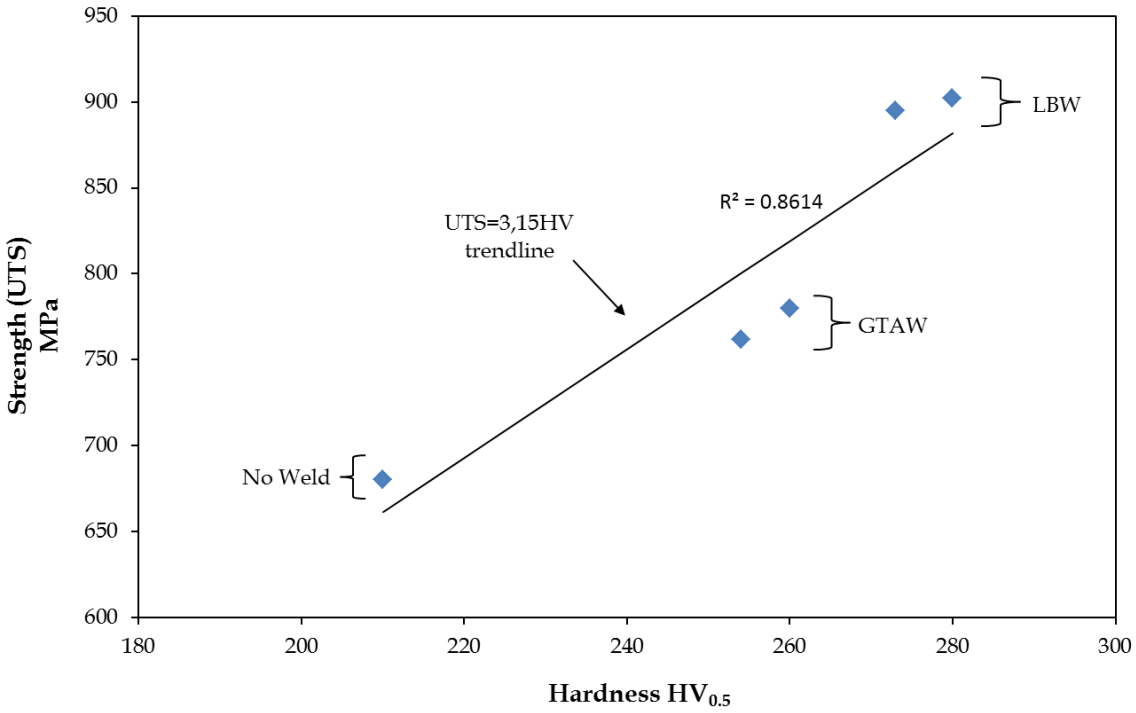

Figure 58: Correlation between hardness and ultimate tensile strength from the Zr-2.5Nb sub-size tensile samples.

CHAPTER 7

Conclusions and Recommendations

7.1 Conclusions

Conclusions drawn based on the results obtained during this study, are as follows:

1. Both laser and GTAW processes displayed similar grain structures. At a low heat input, the HAZ and weld metal of both processes were characterized by equiaxed grains. Increasing the heat input resulted in columnar grains, solidifying by epitaxial growth.
2. The size of the weld's cross–sectional area displayed a positive linear response to increasing heat input.
3. The microstructural transformation products as a function of heat input or cooling rate between the welds and dilatometry samples showed good consistency. The GTAW microstructures exhibited a basket weave structure in both of the HAZ and weld metal, with retained beta phase observed in the HAZ of some welds. The LBW microstructures consisted of a mixture of martensite, retained beta and Widmanstätten structure in the HAZ and a fully martensitic weld metal.
4. The cooling rate had no influence on the hardness of martensite which was 275 $HV_{0.5}$ on average. The muted hardness response of martensite is true within the parameters applied in the current study where the maximum calculated cooling rate in a laser weld was 1664°C/s. The hardness of the Widmanstätten microstructure, by contrast, had a positive linear relationship to an increasing cooling rate.
5. Laser beam welds have a higher hardness and tensile strength than gas tungsten arc welds even at similar heat inputs. The higher strength of LBW welds compromises their ductility as observed in the total percentage strain from tensile test results and cleavage fracture surfaces.

7.2 Recommendations

Transmission electron microscopy (TEM) analysis is recommended for future work to assist in understating the morphological development during the beta to alpha transformation at varying cooling rates. TEM studies will also reveal the structures that form between the α/β interface and the substructures (dislocations and twins) within the martensite plates.

Zirconium alloys find application in the nuclear industry because of excellent neutron economy and good corrosion properties. It would be of great interest to investigate the effect of welding on the corrosion behaviour of the zirconium-2.5niobium alloy.

REFERENCES

Abriata, J.P., and Bolcich, J.C., 1982. The Nb−Zr (niobium−zirconium) system. *Journal of Phase Equilibria*, *3*(1), pp.34-44.

Adamson, R., Garzarolli, F., Cox, B., Strasser, A. and Rudling, P., 2007. Corrosion mechanisms in zirconium alloys. *ZIRAT12 Special Topic Report Corrosion Mechanisms in Zirconium Alloys*

Aldridge, S.A. and Cheadle, B.A., 1972. Age hardening of Zr-2.5 wt% Nb slowly cooled from the (α+ β) phase field. *Journal of Nuclear Materials*, *42*(1), pp.32-42.

American Society of Mechanical Engineers (ASME), 2010. *Boiler & Pressure Vessel Code VIII: Rules for Construction of Pressure Vessels*, BPVC-VIII-1-2010, New York: ASME

American Society for Testing and Materials, International (ASTM), (B811-02), 2002., *Wrought Zirconium Alloy Seamless Tubes for Nuclear Reactor Fuel Cladding,* West Conshohocken, PA.

American Welding Society (AWS G2.5/G2.5M), 2012. *Guide for the Fusion Welding of Zirconium and Zirconium Alloys,* An American National Standard, Miami, FL.

Atkins, M., 1980. Atlas of continuous cooling transformation diagrams for engineering steels. *American Society for Metals International (ASM),* Materials Park, OH, p.260.

Banerjee, S., Buschow, K.H.J., Robert, W.C., Merton, C.F., Bernard, I., Edward, J.K., Subhash, M. and Patrick, V., 2001. Nuclear applications: zirconium alloys. *Encyclopaedia of Materials: Science and Technology (Second Edition),* Elsevier, Oxford, pp.6287-6299.

Banerjee, S., Dey, G.K., Srivastava, D. and Ranganathan, S., 1997. Plate-shaped transformation products in zirconium-based alloys. *Metallurgical and Materials Transactions A*, *28*(11), pp.2201-2216.

Banerjee, S. and Krishnan, R., 1971. Martensitic transformation in zirconium-niobium alloys. *Acta metallurgica*, *19*(12), pp.1317-1326

Banerjee, S. and Mukhopadhyay, P., 2010. *Phase transformations: examples from titanium and zirconium alloys* (Vol. 12). Pergamon material series, Elsevier, Oxford UK.

Banerjee, S., Vijayakar, S.J. and Krishnan, R., 1976. Precipitation in zirconium-niobium martensites. *Journal of Nuclear Materials*, *62*(2-3), pp.229-239.

Beneš, O., Van Uffelen, P., Van de Laar, J., Győri, C., Konings, R.J.M. and Hózer, Z., 2011. Kinetic studies of the α–β phase transition in the Zr1% Nb cladding for nuclear reactors. *Journal of Nuclear Materials*, *414*(2), pp.88-91.

Bordoni, R. and Olmedo, A.M., 2011. Oxide thickness measurements and characterisation of two Zr-2.5Nb pressure tubes of Embalse nuclear power plant. *Acta Microscopica*, Vol *20*(1) pp.10-20.

Chai, L., Wu, H., Wang, S., Chen, K., Wang, T. and Xia, J., 2017. Characterization of microstructure and hardness of a Zr-2.5 Nb alloy surface-treated by pulsed laser. *Materials Chemistry and Physics*, Elsevier BV, Amsterdam, Netherlands 198,pp.303-309.

Cheadle, B.A., 1975. The physical metallurgy of zirconium alloys (No. CRNL--1208). *Atomic Energy of Canada Limited*, Chalk River, ON., Canada.

Choubey, R. and Jackman, J.A., 1996. Micro-segregation of oxygen in Zr-2.5 Nb alloy materials. *Metallurgical and Materials Transactions A*, *27*(2), pp.431-440.

Cochrane, C.J., 2013. *Effect of Process Parameters on Deformation of Zr-2.5 wt% Nb Alloy* (Doctoral dissertation, Queen's University (Canada))

Coleman, C.E., Doubt, G.L., Fong, R.W., Root, J.H., Bowden, J.W., Sagat, S. and Webster, R.T., 1994. Mitigation of harmful effects of welds in zirconium alloy components. In *Zirconium in the Nuclear Industry: Tenth International Symposium*. ASTM International.

DuPont, J.N. and Marder, A.R., 1995. Thermal efficiency of arc welding processes. *Welding Journal-Including Welding Research Supplement*, *74*(12), p.406s.

Easterling, K., 2013. *Introduction to the physical metallurgy of welding*. Elsevier.

Elliot, A.J., Muir, I.J. and Shaddick, A., 2005. In-reactor corrosion and deuterium uptake studies of Zr-2.5Nb pressure tube materials. *Behaviour of high corrosion resistance Zr-based alloys*, p.32.

Evans, W., LeSurf, J.E. and Thomas, W.R., 1967. Heat-treated Zr-2.5% Nb pressure tubes for water-cooled power reactors, presented at *CNA annual conference*, Atomic Energy of Canada, Report AECL-2890.

Fong, R.W.L., Miller, R., Saari, H.J. and Vogel, S.C., 2012. Crystallographic texture and volume fraction of α and β phases in Zr-2.5 Nb pressure tube material during heating and cooling. *Metallurgical and Materials Transactions A*, *43*(3), pp.806-821.

Forgeron, T., Brachet, J.C., Barcelo, F., Castaing, A., Hivroz, J., Mardon, J.P. and Bernaudat, C., 2000, January. Experiment and modeling of advanced fuel rod cladding behavior under LOCA conditions: Alpha-beta phase transformation kinetics and EDGAR methodology. In *Zirconium in the nuclear industry: twelfth international symposium*. ASTM International.

Funderburk, R.S., 1999. A look at heat input. *Welding Innovation*, *16*(1), pp.8-11.

Garcí, C., Caballero, F.G., Capdevila, C. and Alvarez, L.F., 2002. Application of dilatometric analysis to the study of solid–solid phase transformations in steels. *Materials Characterization*, *48*(1), pp.101-111.

Griffiths, M., Winegar, J.E. and Buyers, A., 2008. The transformation behavior of the β-phase in Zr–2.5 Nb pressure tubes. *Journal of Nuclear Materials*, *383*(1-2), pp.28-33.

Hälsig, A., Pehle, S., Kusch, M. and Mayr, P., 2017. Reducing potential errors in the calculation of cooling rates for typical arc welding processes. *Welding in the World*, *61*(4), pp.745-754.

Higgins, G.T., and Banks, E.E., 1966. The martensite start temperature in dilute zirconium-niobium alloys. *British Journal of Applied Physics*, *17*(2), p.283.

Hiwarkar, V.D., Sahoo, S.K., Samajdar, I., Narasimhan, K., Krishna, K.M., Dey, G.K., Srivastava, D., Tewari, R. and Banerjee, S., 2009. Annealing of cold worked two-phase Zr-2.5Nb associated microstructural developments. *Journal of Nuclear Materials*, *384*(1), pp.30-37.

Hunt, C.E.L., and Niessen, P., 1970. The effect of oxygen on the equilibrium β/α+ β transformation temperature of zirconium-niobium alloys. *Journal of Nuclear Materials*, *35*(1), pp.134-136.

Hunt, C.E.L., and Niessen, P., 1971. The continuous cooling transformation behavior of zirconium-niobium-oxygen alloys. *Journal of Nuclear Materials*, *38*(1), pp.17-25.

Jepson, K.S., Brown, A.R.G. and Gray, J.A., 1970. Effect of cooling rate on the beta transformation in titanium-niobium and titanium-aluminum alloys. *Royal Aircraft Establishment*, Farnborough, Eng.

Kaufman, L., 1959. The lattice stability of metals—I. Titanium and zirconium. *Acta Metallurgica*, *7*(8), pp.575-587.

Krishnan, R. and Asundi, M.K., 1981. Zirconium alloys in nuclear technology. *Proceedings of the Indian Academy of Sciences Section C: Engineering Sciences*, *4*(1), pp.41-56.

Krueger, B.R., 2015. Reactive refractory and precious metals and alloys. *Welding Handbook.* American Welding Society. Chapter 7, 449-482

Kumar, M.K., Vanitha, C., Samajdar, I., Dey, G.K., Tewari, R., Srivastava, D. and Banerjee, S., 2004. Textural and microstructural developments during fabrication of Zr–2.5 Nb pressure tubes. *Journal of nuclear materials*, *335*(1), pp.48-58.

Lambert, J.B. and Rausch, J.J., 1992. Non-Ferrous Alloys and Special-Purpose Materials, Materials Handbook, Vol. 2. *ASM INTERNATIONAL, Materials Park, OH*, pp.557-82.

Langford, W.J., and Mooder, L.E.J., 1978. Fracture behavior of zirconium alloy pressure tubes for Canadian nuclear power reactors. *International Journal of Pressure Vessels and Piping*, *6*(4), pp.275-310.

Lippold, J.C., 2014. *Welding metallurgy and weldability*. John Wiley & Sons, Hoboken, New Jersey

Lustman, B. and Kerze, F. eds., 1955. *The metallurgy of zirconium* (Vol. 4). McGraw-Hill Book Company, Pennsylvania Plaza, New York City.

Mazumder, J., 1993. Laser beam welding. *American Society for Metals International (ASM) Handbook*, Materials Park, OH. Vol 6, pp.262-269.

Messler, R.W., 1999. Principles of Welding: *Processes, Physics, Chemistry, and Metallurgy*. Wiley VCH, Weinheim, Germany.

Moorthy, K.B., 1969. Current trends in the use of Zirconium Alloys. *Bhabha Atomic research centre*, Bombay, pp.181-187

Musaeva, Z.A., and Peletskii, V.E., 2005. An investigation of the thermal conductivity of Zr–2.5%Nb reactor alloy. *High Temperature*, *43*(5), pp.694-699.

Nikulina, A.V., 2010. Metal Science Aspects of Zirconium-Base Reactor Material Production in the Soviet Union, *Zirconium Production and Technology: The Kroll Medal Papers 1975–2010*, R. Adamson, Ed., ASTM International, West Conshohocken, PA, pp.179-194.

Northwood, D.O., 1985. The development and applications of zirconium alloys. *Materials & design*, *6*(2), pp.58-70.

Perovic, V. and Weatherly, G.C., 1989. The β to α transformation in a Zr-2.5 wt% Nb alloy. *Acta Metallurgica*, *37*(3), pp.813-821.

Robertson, J.A.L., 1979. Nuclear energy in Canada: the CANDU system. *Atomic Energy of Canada Limited.* Chalk River, ON., Canada.

Robson, J.D., 2008. Modelling precipitation in zirconium niobium alloys. *Journal of Nuclear Materials*, *377*(3), pp.415-422.

Rudling, P., Strasser, A., Garzarolli, F. and van Swam, L., 2007. Welding of zirconium alloys, *special topic report (IZNA7): Welding of Zirconium Alloys*. Advanced Nuclear Technology (ANT) International, Skultuna, Sweden

Sabol, G.P., 1970. Precipitation behavior in Zr/2.5 wt% Nb alloys. *Journal of Nuclear Materials*, *34*(2), pp.142-150.

Saibaba, N., Jha, S., Tonpe, S., Vaibhaw, K., Deshmukh, V., Rao, S.R., Krishna, K.M., Neogy, S., Srivastava, D., Dey, G. and Kulkarni, R., 2012, April. Microstructural studies of heat treated Zr-2.5Nb alloy for pressure tube applications. In *Zirconium in the Nuclear Industry: 16th International Symposium*. ASTM International.

Slattery, G.F., 1965. Some dilatometric observations on the α-β transformation in zirconium-212 wt.% niobium alloy. *Journal of the Less Common Metals*, *8*(3), pp.195-208

Sokolov, M. and Salminen, A., 2014. Improving laser beam welding efficiency. *Engineering*, *6*(09), p.559.

Song, S.G., and Gray, G.T., 1995. Influence of temperature and strain rate on slip and twinning behavior of Zr. *Metallurgical and Materials Transactions A*, *26*(10), pp.2665-2675.

Srivastava, D., Mukhopadhyay, P., Banerjee, S. and Ranganathan, S., 2000. Morphology and substructure of lath martensites in dilute Zr-Nb alloys. *Materials Science and Engineering: A*, *288*(1), pp.101-110.

Standard, A.S.T.M., 2009. B551: Standard specification for zirconium and zirconium alloy sheet. *Strip and Plate, Annual Book of ASTM Standards, ASTM International, West Conshohocken, PA*.

Stenbacka, N., Choquet, I. and Hurtig, K., 2012. Review of arc efficiency values for gas tungsten arc welding. In *IIW Commission IV-XII-SG212, Intermediate Meeting, BAM, Berlin, Germany, 18-20 April 2012* (pp. 1-21).

Tenckhoff, E., 2005. Review of deformation mechanisms, texture, and mechanical anisotropy in zirconium and zirconium base alloys. *Journal of ASTM International*, *2*(4), pp.1-26.

Vander Voort, G.F., 1984. *Metallography, principles and practice*. American Society for Metals International (ASM), Materials Park, OH.

Weman, K., 2011. *Welding processes handbook*. Woodhead Publishing Ltd, Cambridge, England.

Williams, C.D. and Gilbert, R.W., 1966. Tempered structures of a Zr-2.5 wt% Nb alloy. *Journal of Nuclear Materials*, *18*(2), pp.161-166.

Yoo, M.H., Morris, J.R., Ho, K.M. and Agnew, S.R., 2002. Nonbasal deformation modes of HCP metals and alloys: Role of dislocation source and mobility. *Metallurgical and Materials Transactions A*, *33*(3), pp.813-822.

Yuan, G., Zhang, L., Yue, Q., Gu, H., Li, G. and Shen, J., 2015. Microstructural characteristics of β precipitates in Zr–1Nb alloy. *Materials Chemistry and Physics*, *165*, pp.87-90.

APPENDIX

Table 21: Transformation temperatures of Zr-2.5Nb as derived from dilatometry cooling curves

Cooling rate (°C/s)	Transformation temperature (°C)	
	Start $\beta/(\beta_{Zr}+\alpha_{Zr})$	**Finish** $(\beta_{Zr}+\alpha_{Zr})/(\beta_{Nb}+\alpha_{Zr})$
0.5	865	680
1	772	640
10	795	600
25	775	565
50	756	512
	$\mathbf{M_s}$	$\mathbf{M_f}$
150	690	435
300	660	410
600	645	395

Table 22: Calculating the correlation between UTS and hardness

	Hardness	**UTS**	**UTS/$HV_{0.5}$**
Base	210	680	3.24
GTAW	254	762	3.00
GTAW	260	780	3.00
LBW	273	895	3.29
LBW	280	902	3.22
		Average	3.15 +/- 0.15